https://ntrs.nasa.gov/search.jsp?R=19660020451 2020-03-16T20:56:48+00:00Z

GPO PRICE $ ______

CFSTI PRICE(S) $ ______

Hard copy (HC) 5.00

Microfiche (MF) 1.00

ff 653 July 65

FACILITY FORM 602

N66 29741	
(ACCESSION NUMBER)	(THRU)
163	1
(PAGES)	(CODE)
CR-76014	25
(NASA CR OR TMX OR AD NUMBER)	(CATEGORY)

PRINCETON UNIVERSITY

DEPARTMENT OF

AEROSPACE AND MECHANICAL SCIENCES

NATIONAL AERONAUTICS
AND
SPACE ADMINISTRATION

Research Grant NsG-306-63

DYNAMICS OF A PINCH DISCHARGE DRIVEN BY A HIGH CURRENT PULSE-FORMING NETWORK

Report No. 778*

Prepared by Neville A. Black
Neville A. Black

Approved by Robert G. Jahn
Robert G. Jahn
Associate Professor
and Research Leader

*This report is a reproduction in entirety of the Ph.D. dissertation of Mr. Neville A. Black. It is submitted to the sponsor and to the distribution list in this form both as a presentation of the technical material, and as an indication of the academic program supported by this Grant.

Reproduction, translation, publication, use and disposal in whole or in part by or for the United States Government is permitted.

May 1966

Guggenheim Laboratories for the Aerospace Propulsion Sciences
Department of Aerospace and Mechanical Sciences
PRINCETON UNIVERSITY
Princeton, New Jersey

ABSTRACT

29741

A large-radius, linear pinch discharge is driven by a high current pulse-forming network, consisting of a simple ladder configuration with capacitance added at various points along the distributed inductance afforded by two parallel-plate conductors. A variety of current waveforms are obtainable, typified by a 4.5 μsec., 200,000 amp. constant-amplitude pulse, rising in 0.6 μsec. for 10 KV charging voltage. The dynamical behavior of discharges driven by these waveforms is well represented by a snowplow model. The dynamical efficiency of the discharge as a gas accelerator is found to be favored by conditions that provide for maximum mass accumulation early in the acceleration process. Under certain conditions a precursor current pulse is observed to separate from the main current sheet, and to propagate ahead with twice snowplow velocity.

Author

CONTENTS

Page

ABSTRACT i
CONTENTS ii
LIST OF ILLUSTRATIONS iv

Chapter
I. PROPULSION SYSTEMS 1

1.1 Space Propulsion 1
1.2 Electric Propulsion Systems 3
1.3 Electrostatic and Electromagnetic Thrustors 5
1.4 Plasma Propulsion 6

II. CURRENT SHEETS 10

2.1 Fusion Research 10
2.2 The Pinch Effect 12
2.3 Pulsed Plasma Accelerators 14
2.4 The Pulsed High-Current Discharge 18

III. THE PRODUCTION OF LARGE PULSE CURRENTS 22

3.1 Conventional Capacitor Banks 22
3.2 Sustained Currents 25
3.3 The Ladder Network 27
3.4 Other Techniques 31

IV. EXPERIMENTAL APPARATUS 33

4.1 Discharge Chamber and Switch 33
4.2 Operating Sequence 33
4.3 The Pulse-Forming Network 35
4.4 Electrical Characteristics 37
4.5 Instrumentation 42
4.6 Network Response 47

V. EXPERIMENTAL OBSERVATIONS 51

5.1 Qualitative Discharge Behavior 51
5.2 Current Densities 57
5.3 Current Sheet Bifurcation 70
5.4 Discharge Dynamics 70

CONTENTS

Page

Chapter
VI. THE SNOWPLOW MODEL 73

6.1 The Model 73
6.2 The Linear Pinch Snowplow Equation 74
6.3 Comparison of Observed and Calculated Trajectories 79
6.4 Trajectory Bifurcation 85
6.5 Dynamical Efficiency of the Snowplow Model 87
6.6 A Gasdynamic Argument 92

VII. REVIEW AND RECOMMENDATIONS 98

Appendix
A. TRANSMISSION LINES AND PULSE-FORMING NETWORKS. 101

A.1 The Ideal Uniform Transmission Line 101
A.2 The Equi-Section Network 105
A.3 The Distributed Line with Parasitic Inductance 112
A.4 A Variational Approach 117

B. SNOWPLOW MATHEMATICS 122

B.1 Dimensional Analysis 122
B.2 Similarity Relations of the Snowplow Equation 125
B.3 Analytic Solutions of the Snowplow Equation 129

C. ELECTRODYNAMICS OF PULSED DISCHARGES 133

C.1 Electric Fields and Terminal Voltage 133
C.2 Damping by Time-Varying Inductance 138
C.3 Validity of the Inductance Concept 140

ACKNOWLEDGEMENTS. 141

REFERENCES. 142

LIST OF ILLUSTRATIONS

Figure Page

2-1 Pulsed Plasma Accelerators 15

4-1 Experimental Apparatus (Schematic) 34

4-2 Top View of Pulse Forming Network (Schematic). . 36

4-3 Capacitor Units. 38

4-4 Pulse Forming Network Cross Section (Schematic). 39

4-5 View of Pulse Forming Network. 40

4-6 Block Diagram Streak Photograph Operation. . . . 45

4-7 Network Behavior in Uniform Line Configuration . 49

5-1 Comparison of Streak Photographs for Two Current Waveforms. 52

5-2 Comparison of Magnetic Probe Responses for Two Current Waveforms. 54

5-3 Effect of Various Driving Currents on 100 μ Argon Discharge 56

5-4 Sine and Pulse Driving Currents. 58

5-5 (a) Current Density: 0.6 Microseconds 60
(b) Current Density: 1.1 Microseconds 61
(c) Current Density: 1.7 Microseconds 62
(d) Current Density: 2.2 Microseconds 63
(e) Current Density: 2.8 Microseconds 64
(f) Current Density: 3.3 Microseconds 65
(g) Current Density: 3.6 Microseconds 66
(h) Current Density: 4.4 Microseconds 67
(i) Current Density: 5.0 Microseconds 68
(j) Current Density: 5.6 Microseconds 69

5-6 Pinch Discharge Current I and Probe Response $\partial B/\partial t$, at R = 1.5" 71

6-1 Pinch Discharge. 75

6-2 Snowplow Model and Current-Sheet Trajectories. . 80

6-3 Snowplow Model and Current-Sheet Trajectories. . 81

6-4 Snowplow Model and Current-Sheet Trajectories. . 83

LIST OF ILLUSTRATIONS-cont'd

Figure		Page
6-5	Snowplow Model and Current-Sheet Trajectories. .	84
6-6	Trajectories of $\partial B/\partial t$ Maxima, Luminous Front and Snowplow Model in 8" Pinch Discharge at 100 μ Argon.	86
6-7	Piston Driven Shock Wave	93
A-1	Response of Equi-Section Networks.	106
A-2	Effect of Parasitic Inductance, 10-Section Network	108
A-3	Effect of Number of Sections, Constant Resonant Frequency Capacitors	111
A-4	Short Circuit Current for Distributed Line With Parasitic Inductance.	116
B-1	Non-Dimensional Snowplow Trajectories.	127
C-1	Configuration for Discussion of Electric Fields.	134

CHAPTER I

PROPULSION SYSTEMS

1.1 SPACE PROPULSION

The principle of conservation of momentum governs the performance of reaction propulsion systems. Thus if a single-stage rocket having constant exhaust velocity v_e changes its velocity by an amount Δv, then, neglecting gravitational fields, its final and initial masses, m_f and m_i respectively, are related by

$$\frac{m_f}{m_i} = \mathrm{EXP}[-\Delta v/v_e] \qquad (1\text{-}1)$$

A major aim of rocket propulsion research has been to raise v_e so that for a given single stage mass ratio the velocity increment Δv may be increased. Chemical rockets presently attain exhaust velocities of about 3000 meters per second. So-called "exotic" propellants might eventually double this figure under very optimistic assumptions. Beyond this point, a new means of accelerating the exhaust stream must be developed.

The term "advanced propulsion" is commonly applied to any thrust producing system which does not primarily depend on the energy of chemical reaction of its exhaust material.

Corliss(1) has given a comprehensive survey of many advanced propulsion concepts. At present and foreseeable levels of technological development two broad classes of thrustors show promise for high exhaust velocity space propulsion: the direct nuclear and the electric systems.

In a direct nuclear system, the energy released in a nuclear reaction is transferred thermally to the propellants. At progressively higher temperatures the fissioning material will be in the solid, liquid, or gaseous state leading to the designations of solid core, liquid core, and gaseous core nuclear rockets.

The solid-core nuclear rocket, after a decade of intensive development, is now an engineering reality.(2) While the working temperatures are actually lower than those of chemical rockets, exhaust velocities of 8000 meters per second are achieved by virtue of the low molecular weight of the hydrogen propellant. Velocities of up to 30,000 meters per second have been visualized for liquid and gaseous core rockets, but at present they can only be considered concepts for which some research has been done on the enormously complicated fluid mechanics and heat transfer problems involved in transferring energy to the propellant while limiting the amount of fissile material lost to the exhaust stream.

In an electric propulsion system, electric power is used to impart energy to the propellant by some mechanism or combination of mechanisms. Batteries might provide power for flight testing; solar cell power could be used to meet the propulsion requirements of some altitude-control, station-keeping, and unmanned-probe tasks. But for space missions in which electric propulsion would be used as a primary thrust system on large vehicles, the electric power requirements are such that they must be provided by some generator whose ultimate source is nuclear energy. The adjective "nuclear-electric" is applied to such a propulsion system.

1.2 ELECTRIC PROPULSION SYSTEMS

Jahn(3) has provided a recent comprehensive review of the physics and engineering of many proposed electric thrustor concepts. It is clear that as a class such thrustors offer exhaust velocities from 10,000 meters per second upwards, albeit with varying efficiencies of conversion of electric power to exhaust-stream power. Electric thrustors are commonly classified in one of three categories: electrothermal, electromagnetic, and electrostatic.

In his book, Jahn defines these categories as follows:

1. <u>Electrothermal Propulsion</u>--wherein the propellant gas is heated electrically, then expanded through a nozzle.
2. <u>Electrostatic Propulsion</u>--wherein the propellant is accelerated by direct application of electric body forces to ionized gas particles.
3. <u>Electromagnetic Propulsion</u>--wherein the propellant is accelerated by somewhat complex interactions of external and internal electric and magnetic fields.

In general, electrostatic devices offer the highest exhaust velocities, followed by electromagnetic and electrothermal schemes. One should not conclude, however, from Eq. (1-1) and our discussion to this point, that the sole criterion of a propulsion system is the exhaust velocity. An electric propulsion system requires a power supply whose mass can be expected to increase as an approximately linear function of power. At a given thrust level the exhaust power, and hence the power plant mass, is a linearly increasing function of exhaust velocity. Thus while propellant mass is reduced by higher exhaust velocity, the power plant mass is increased. Clearly, for a given mission, there is an optimum exhaust velocity to minimize the sum of the masses. For a discussion of this point, and of the characteristics of electro-thermal thrustors, we refer again to the books by Corliss(1) and Jahn.(3) We do not intend here to enter into the thicket of comparative mission analyses, in which small assumptions grow rapidly into large conclusions. A recent map of this thicket, somewhat pessimistic for electric propulsion is presented in a RAND report(4) by Pinkel, et al.

The application of electric thrustors as prime propulsion units for space missions thus depends on the development of sufficiently-low mass power plants. Because power-conditioning equipment, such as D.C. to A.C. inverters, low to high voltage transformers, etc., that might be required to match the electrical characteristics of generator and thrustor would constitute a significant fraction of the power plant mass, as well as reducing reliability, it seems likely that the choice of electric thrustor system will ultimately be determined by the best available generator.

The dominant parameter for performance evaluation is the ratio of total mass of the power plant and thrustor system to the directed kinetic energy component of exhaust beam power. Forty pounds per kilowatt looks useful; less than ten pounds per kilowatt is alluring.

1.3 ELECTROSTATIC AND ELECTROMAGNETIC THRUSTORS

At present writing, the electrostatic thrustor, or ion engine, has the distinction of having been flight tested in space and achieving its predicted performance. But the ion engine affords a thrust per unit area inherently lower than that of electromagnetic thrustors. The stress associated with electrostatic fields is $\epsilon_0 E^2/2$, while for magnetic fields it is $B^2/2\mu_0$. We have for a rather extreme electric field of 10^7 volts/meter:

$$\frac{\epsilon_0 E^2}{2} = \frac{8.85 \times 10^{-12} \times (10^7)^2}{2} \sim 5 \times 10^2 \text{ NEWTONS}/\text{M}^2 \tag{1-2}$$

While for a comparatively modest magnetic field of 1 weber/m^2 (= 10,000 gauss):

$$\frac{B^2}{2\mu_0} = \frac{1}{2 \times 4\pi \times 10^{-7}} \sim 5 \times 10^5 \text{ NEWTONS}/\text{M}^2 \tag{1-3}$$

A practical ion engine must have very closely spaced electrodes in order that maximum electric field strength, and thus maximum thrust density, be achieved.(5) Combining this requirement with that of large area, to compensate for the low value of maximum thrust density, produces an inherently vulnerable, cumbersome thrustor.

An even more serious deficiency of the ion engine is its range of exhaust velocities: the maximum is limited only by relativistic considerations, but achieving less than 50,000 meters per second at maximum thrust density is difficult.

Electromagnetic thrustors offer, in comparison with electrostatic devices, the possibility of a high-thrust density, rugged device covering the velocity range from some 10,000 meters per second upwards. This possibility has caused research on electromagnetic thrustors to be actively pursued in a number of laboratories, despite the inherent complexity of the physical phenomena involved. In these devices currents flow in a conducting, macroscopically neutral gaseous medium, thus they are referred to as plasma engines.

1.4 PLASMA PROPULSION

Most plasma engines pass current through the gas by means of electrodes. "Electrodeless" accelerators are coupled by time varying fields, and achieving sufficiently "tight" coupling has been the major problem of these devices.(1,3,6,7) It is conventional to categorize electrode-using systems by the terms steady and pulsed; in a steady device the local time derivatives of field and flow properties are all zero.

The simplest manifestation of a steady plasma accelerator using electrodes is a duct having mutually perpendicular electric and magnetic fields perpendicular to the axis of the duct. The electric field drives a current through the plasma and the interaction of this current with the applied magnetic field drives the plasma along the duct. Velocities of 20,000-30,000 meters per second have been achieved in this fashion. The duct walls, however, are severely tried. Magnetic fields of some kilogauss strength are required. In laboratory devices these are generally provided by massive, power-consuming electro-magnets which tend to dwarf the accelerator itself. Super-conducting electro-magnets may find application here, although the refrigeration requirement carries its own set of engineering problems. These steady $\bar{j} \times \bar{B}$ thrustors do involve technology in common with magnetohydrodynamic power generation and, consequently, benefit directly from the extensive research now going on in this area.

The currents flowing in $\bar{j} \times \bar{B}$ thrustors also produce their own magnetic fields. The forces produced by the interaction of the current and its self magnetic field vary as the square of the current. Thus, at sufficiently high currents, useful levels of force can be attained without employing separate magnetic field sources. Currents ranging from a few thousand amperes to hundreds of kiloamperes, and associated power levels of tens of kilowatts to hundreds of megawatts may be required. Laboratory experimentation is greatly facilitated by the use of capacitive energy storage systems, which can readily provide the requisite power levels on a time scale of some microseconds to a millisecond.

We must distinguish here between the concepts of "pulsed" and "pulsed quasi-steady" plasma accelerators. A steady device was defined as one in which the local time derivatives of field and flow properties are effectively zero. If, in view of the considerations of the above paragraph, we energize such a device by a capacitor bank for some microseconds, we call it "pulsed- (in deference to the rapid discharge of energy) quasi-steady (because the fundamental mechanisms do not depend on the transient nature of the operation)."

Recent work(8) has indicated that the supposedly electrothermal arc-jet thrustors, when driven into a high-power high-current mode of operation in which self-magnetic fields are presumably important, deliver high exhaust velocities at high efficiency. The technique of pulsed quasi-steady operation has recently been applied to the study of the high-current arc jet.(9) It facilitates high-power operation, and the transient instrumentation tools, such as the magnetic probe for determining current density distributions and the inductive total-current monitoring loop (Rogowski coil), of pulsed experimentation can be used to determine the final properties in a pulsed quasi-steady apparatus by monitoring the transient approach to final values.

In this work we deal with pulsed plasma acceleration which is fundamentally dependent on transient phenomena: the rate of current rise is so fast that the associated magnetic field is largely excluded from the conducting plasma, and the driving force is produced by the interaction of the magnetic field and the relatively thin current sheet. Pulsed plasma thrustors have characteristic velocities of 10,000 - 80,000 meters per second, the appropriate range for interplanetary missions. The present state of development is indicated in the writings of Jahn,(3) Lovberg,(7) and Sutton and Sherman(10) and the references to the literature provided by these authors. The ultimate utility of any electric propulsion system depends on achieving an adequate value for the conversion efficiency of electric power input to directed exhaust energy. From this standpoint, pulsed plasma thrustors are less developed than the ion engines, because of the inherent complexity of the physical phenomena involved in their operation. But there seems to be no fundamental obstacle to the attainment of adequate efficiency, and research on these devices is spurred by their promise of high thrust density.

CHAPTER II

CURRENT SHEETS

2.1 FUSION RESEARCH

A major scientific effort to achieve a sustained controlled thermonuclear fusion reaction has been under way for several years. Accomplishment of this feat would provide the world with power for millennia.

At sufficiently high temperatures, nuclei of deuterium and tritium[+] will collide with such violence that the mutual repulsion of their positive charge is overcome to the point that the short-range nuclear forces come into play and a fusion reaction of the two nuclei, with release of large amounts of energy, may occur. The problems are as obvious as the concept is simple: the gas must be confined in a bounded volume so that reactions can occur, while heated to temperatures orders of magnitude greater than any material wall can sustain. However, the gas will be effectively fully ionized, and conducting, at much lower temperatures. Electric and magnetic fields may then be used for the dual purposes of confining the gas away from material walls and heating it further. Vigorous efforts were made along these lines, during

---

[+] Reactions will occur with ordinary hydrogen, or other light elements.(12) However, the deuterium-tritium reaction is achievable at the lowest "sufficiently high temperature."

the development of thermonuclear weapons, under conditions of great secrecy. The secrecy curtain was lifted in stages beginning in 1955, culminating in a rather complete de-classification in time for the 1958 Second United Nations Conference on the Peaceful Uses of Atomic Energy. The scientists involved were not greatly amazed to find that almost identical approaches had been followed in the U.S.A., the U.K., and the U.S.S.R., with quite similar experimental and theoretical results.

This "breakout" into the open literature caused a rebirth of scientific interest in gas discharges, under the name of plasma physics, which emphasized the importance of the electrical effects of the highly ionized medium. Bishop has provided a very readable, though simplified, account of the U.S. efforts in controlled fusion through 1959.(11) The books by Glasstone and Lovberg,(12) and Rose and Clark,(13) are comprehensive introductory surveys of plasma physics with a controlled fusion focus, emphasizing respectively the experimental and analytical aspects.

While the physicists attacked the physics of plasmas with the weapons of kinetic theory and statistical mechanics, emphasizing the concept of interactions between charged particles, the fluid dynamicists plunged into the fray with Maxwell's equations wedded to those of continuum fluid mechanics. Despite the now-extensive body of theory on what has come to be called magnetogasdynamics, the techniques and concepts of experimental pulsed plasma propulsion research have been principally acquired from the fusion laboratories; magnetogasdynamics has been more fruitfully applied to the steady and quasi-steady devices.

2.2 THE PINCH EFFECT

Early work on the fusion problem was concentrated on a high-current (10^4 - 10^6 amperes) cylindrical gas discharge. Conceptually, an extremely hot, steady cylindrical gas column could be formed. The continuum-level manifestation of charged particle motion in the presence of magnetic fields, for this situation, is that the interaction force of the current and its self-magnetic field acts radially inward to balance the thermal pressure of the hot conducting gas, containing the discharge away from the walls of the discharge chamber.(14) However, it was shown that losses from electron bremsstrahlung radiation become so great that there is a limiting current, inadequate to achieve fusion conditions, no matter how large the applied electric field (and hence no matter how great the input power) (Ref. 12, Chap. 7). The supposed system is also unstable to geometrical perturbations.

High-voltage capacitor banks were used to provide, on a pulsed basis, the requisite high currents for these experiments. It was realized that the transient processes in the development of the constricted--or "pinched"--discharge were important and not accounted for by the above steady-state model. An important advance in understanding pinch discharges was made in 1954 at

Los Alamos by Rosenbluth,(15) and independently and somewhat earlier in the U.S.S.R. by Leontovich and Osovets,(16) who proposed an elegant dynamic model for the transient phase of pinch development. "The impact of the (Rosenbluth) M-theory on the pinch program was both immediate and far-reaching" (Ref. 11, p. 31). It offered an explanation for the phenomenon observed in the fast-rising high-current pinch experiments.

When the cold neutral gas breaks down under the effects of the applied electric field, it becomes electrically conducting. The current is then confined to a relatively thin layer by virtue of the skin effect. Under the action of its self magnetic field, this current sheet is driven inward. Rosenbluth's model provides a mathematical description of the dynamics of this process; we explore the consequences in some detail in Chapter VI and Appendix B.

Although the emphasis of controlled fusion research has shifted towards (hopefully) stable quasi-steady schemes in which plasma is confined for times much longer than those associated with the dynamic pinch, the dynamic pinch approach is still being vigorously pursued, in the U.S. principally at the Los Alamos Scientific Laboratory. For various reasons the θ-pinch version is now preferred. Here a fast-rising current in a single-turn coil wrapped around the discharge tube induces an oppositely-flowing azimuthal current in the plasma. A compressive force results from the interaction of this current and its associated axial magnetic field.

We cannot go further into the problems of fusion here; we have ventured thus far to show that, in the late 1950's, dynamic phenomena were known to occur in fast, transient high-current gas discharges.

While the aim of these experiments was to create and hold a volume of gas at enormous temperatures, the characteristic velocities of the dynamic phenomena were some centimeters per microseconds--the regime of interest for space propulsion.

2.3 PULSED PLASMA ACCELERATORS

Rosenbluth proposed that a moving current sheet, together with its magnetic field, would act as a "magnetic piston," accelerating the gas into which it moved. Marshall then pioneered the development of the coaxial plasma gun,(17) in which a current sheet driven by a capacitor bank ejects a blob of fast moving plasma. The concept is illustrated in Fig. (2-1(a)). With the hope that "power grows out of the barrel of a gun," most fusion research laboratories have experimented with using coaxial guns to inject energetic plasma into a some sort of magnetic bottle, in which the plasma energy becomes thermalized. But the device has also been seized upon as a potential pulsed plasma thrustor. As a propulsion device, the coaxial plasma gun has been the subject of much effort by the groups associated with Gloersen, at General Electric, and Lovberg, Gooding and Larson, at General Dynamics.

An alternative concept, also stimulated by the early fusion research, is the "pinch" engine (Fig. 2-1(b)) devised

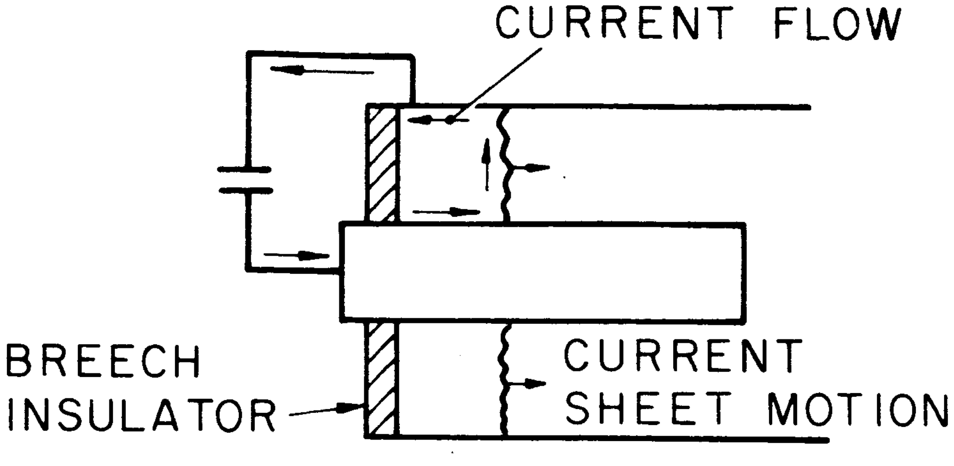

(a)

COAXIAL GUN

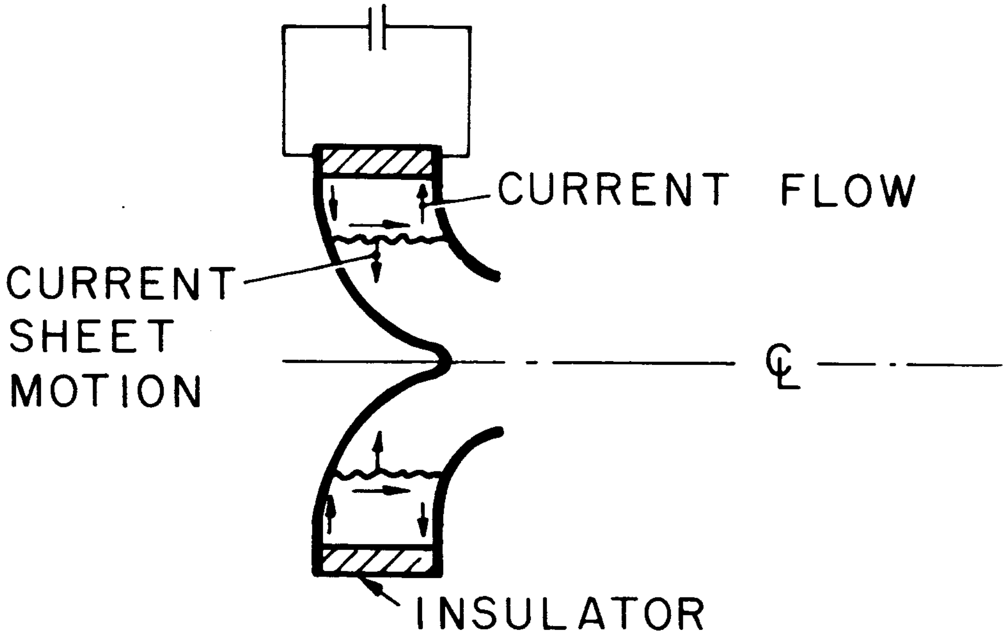

(b)

PINCH ENGINE

AD25-R4118-66

PULSED PLASMA ACCELERATORS

FIGURE 2-1

by Kunen and colleagues at Republic Aviation.(18) Here the current sheet moves initially in the radial direction, acquiring axial motion from the curved electrodes.

The coaxial gun and the pinch engine have much in common; Lovberg(7) has shown how a series of geometrical manipulations changes one device into the other, and encompasses many intermediate geometries which have been studied as possible thrustors. Cylindrical geometry, as opposed to the T-tube, or button gun, or rail gun,(1,3) has come to be favored since, in Lovberg's words, it "forms an edgeless current sheet, and hence, ...can sweep up all propellant...."

Each cycle of a pulsed plasma accelerator can be divided into a series of events: charging of energy storage units, injection of propellant gas, initiation of discharge, formation of current sheet, driving of current sheet into the gas with gas acceleration and increase of inductance, ejection of plasma from the device.

One of the major problems in thrustor development work has been to separate the processes of propellant injection from discharge initiation. If gas is admitted between electrodes with voltage already applied, breakdown occurs on the low-pressure branch of the Paschen curve,+ and the discharge may be launched before adequate mass has been admitted. Much effort has accordingly been devoted to fast-acting gas valves and the geometrical arrangement of gas-injection ports. Experimental

---

+The Paschen curve, for a given geometry, is a plot of breakdown voltage against pressure. Usually, the curve is U-shaped, having a minimum at a critical value of pressure, with breakdown voltage increasing on either side of the critical value.

work is complicated in this gas-triggered mode of operation by the resulting nonuniform density in the device. However, as we shall see, over-all efficiency may be favored by a nonuniform density distribution.

The problems of gas-triggered operation can be relieved by the addition of a high-power switch to the system. Then a desired gas distribution can be established before the voltage is applied to initiate breakdown. This switch-triggered mode of operation is most convenient for research purposes, although severe development problems are raised for a switch suitable for space propulsion requirements that would not involve excessive losses.

We pass over the initiation phase, which represents an extreme case of the "impulse breakdown" problem in which the current rises from zero to several thousand amperes, merely pointing out it is hard to conceive of a more complex and rapid series of gas discharge phenomena. A possible starting point is considering the process as a rapid transition from a glow to arc discharge.(19)

The performance, as a thrust-producing device, of a pulsed plasma accelerator can only be evaluated by exhausting into a high-vacuum environment. While investigations have been made of the exhaust properties--e.g., using microwaves, Langmuir probes, calorimeters, ballistic pendula, ion energy analyzers--relatively little attention has been paid to the details of the actual ejection process where the plasma detaches itself from the accelerator. Jahn(20) has pointed out that this process may be of great importance for the over-all efficiency, and systematic study is now going on. However, before the plasma is ejected, it must be accelerated by the current sheet.

2.4 THE PULSED HIGH-CURRENT DISCHARGE

An effective pulsed plasma thrustor must generate an intense, stable current sheet that efficiently sweeps and accelerates the propellant gas. In 1962, a systematic study of pulsed plasma accelerator phenomena was begun at Princeton. This work has been reported in several publications.(21,22,23) The initial phase of this study was done in closed cylindrical discharge chambers, much like the linear pinch fusion geometry, excepting that the length of the chamber is less than the radius. This geometry was adopted for the advantages it offered for experimental work: ready access of instrumentation through end and sides, essentially one-dimensional (radial) nature in contrast to the inherent two-dimensional (radial and axial) character of the coaxial gun, and most importantly, stability and shot-to-shot reproducibility which make systematic investigation feasible. These advantages had been well demonstrated by the group at Republic Aviation in the operation of a cylindrical pinch "test rig" in conjunction with their plasma pinch engine development work, and the design of our first apparatus relied considerably on their experience. Subsequent devices were constructed in response to insights obtained from earlier models.

Most pulsed plasma experiments, in both fusion and propulsion oriented work, have been performed using energy stored in parallel-connected banks of capacitors. The electrical characteristics of the usual pulsed plasma device, together with the requisite connection to the capacitors, are such that the current waveform, as a function of time, is approximately an exponentially damped sine wave. In fusion work, with a requirement for transfer of large amounts of energy to the discharge, even at extremely high voltages large total capacitance is involved. Consequently, the period of the oscillating circuit is greater than the pinch time, and the pinch typically occurs while the current is rising during the first quarter-cycle of the sinusoidal waveform. Relatively small capacitor banks are generally used in propulsion research, since the total stored energy requirements are more modest than for fusion experiments, with associated advantages in terms of economics and ease of small-scale laboratory operation. A further incentive for small capacitor banks is the general minimum-mass requirement for spacecraft systems. In order to get large currents with small capacitance, much effort must be given to inductance minimization. The resulting system also yields a damped sinusoidal current, whose period is shorter than that of the usual fusion apparatus because of the lower capacitance and inductance. In fact it was often suggested in the early phase of pulsed thrustor research that this process be carried to the limit of a circuit period much less than the transit time of the current sheet, with the hope that in this fashion the capacitor bank would "ring out," delivering a large fraction of its total stored energy to the discharge.

The phenomenon of "secondary breakdown" thwarts the "ringing out" concept, and introduces complications into the conduct of experiments. The primary breakdown begins the initiation phase of the discharge, in which the first current sheet is formed and begins to move during the rising first quarter-cycle of the oscillatory current. Because of the predominantly inductive nature of the discharge, a reverse voltage appears across the chamber in the second quarter-cycle as the current amplitude begins to decrease. This voltage causes a secondary breakdown, with the formation of a second current sheet of opposite sign, commencing at the chamber wall. The first current sheet is then effectively decoupled from the capacitor bank and further changes in the total circuit current are manifested in the second current sheet. References 21, 22, and 23 discuss the behavior of the sinusoid-driven pinch in more detail.

The driving current is the single most important factor governing the behavior of a pulsed plasma discharge. For that reason alone it would be desirable to have this factor under the control of the experimenter, rather than to accept passively only the conditions produced by a damped sinusoid. In addition, the complex phenomena of the multiple current sheets produced by an oscillating discharge current complicate the interpretation of diagnostic measurements, and the premature de-coupling of the primary current sheet from the power source reduces the over-all efficiency of the acceleration process.

The above considerations motivated the development of a pulse-generating system that would deliver a fast-rising large-amplitude current to our pinch apparatus. A current effectively constant for several microseconds was the initial design aim. This would remove the time dependence from the dominant experimental variable, simplifying analysis of experimental data. It was hoped that the sustained current would drive an intense localized current sheet through the complete volume of gas. A further requirement was that the pulse generator could be set up to deliver constant current at various amplitudes, sinusoidal waveforms to compare the two modes of operation, and other non-sinusoidal waveforms to explore more fully the effects of varying the driving current waveform.

Chapter III is devoted to the general and analytic aspects of high-current pulse generation. The practical realization of the desired pulse-generating capability, together with other details of the experimental apparatus, is covered in Chapter IV.

CHAPTER III

THE PRODUCTION OF LARGE PULSE CURRENTS

3.1 CONVENTIONAL CAPACITOR BANKS

Most pulsed plasma experimentation, in both fusion- and propulsion-oriented work, has been done using energy stored in capacitors. This electrostatic field-energy is released by closing some form of fast-acting high voltage high-current switch, or the discharge may be self-switching, i.e. by injecting gas or causing some local discharge by means of auxiliary electrodes. The discharge is predominantly inductive, so to a first approximation we have the equivalent circuit indicated in the sketch:

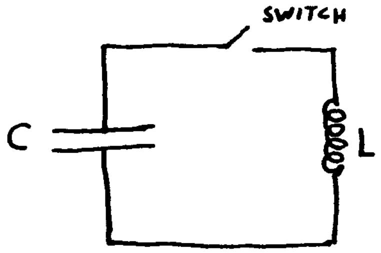

The current I is then given by:

$$I = V_0 \left(\frac{C}{L}\right)^{1/2} \sin \frac{t}{(LC)^{1/2}} \tag{3-1}$$

where V_0 is the initial voltage on the capacitor. Thus, large currents are seen to be associated with high voltage, high capacitance, and low inductance. In practice, a number of identical capacitors are assembled in parallel.

The effective capacitance, C, of n parallel-connected capacitors of magnitude C', is nC'. No actual component has the properties of the "ideal" elements of circuit theory, e.g. at high frequencies the capacitance between turns of a coil becomes important. Such departures from idealized behavior are grappled with by concocting an equivalent circuit which will better represent the behavior of the component. In energy-storage capacitors in the regime of interest, the capacitor should be regarded as having an inductance in series with it. For parallel-connected banks, if each of the n capacitors of value C' has such an inductance L', the equivalent result is a capacitor of value $C=nC'$ in series with an inductance $L_c = L'/n$. In applying Eq. (3-1) we must add to the discharge inductance L_P the effective inductance of the switch, L_S, and the connections of the capacitor bank to the load, L_T. Thus, we have

$$L = L_c + L_S + L_T + L_P \tag{3-2}$$

And for $t \ll (LC)^{1/2}$, Eq. (3-1) reduces to

$$I = \frac{V_0 t}{L} \tag{3-3}$$

In pulsed plasma work one desires to achieve a high rate of current rise, so that magnetic field and plasma, as a consequence of the skin effect, are separated by a relatively thin current layer; rapid rise-rates are facilitated by high voltage and low inductance as Eq. (3-3) shows.

With careful attention to inductance minimization, the current rise-rates and amplitudes necessary for propulsion experiments can be achieved with banks having only a few kilojoules stored energy. The problem of protection against faults, where the total stored energy is sufficient to cause a violent explosion in the event of the failure of capacitor, which is of major importance in the megajoule banks that have been used in the fusion program, is thereby averted; but even relatively small banks, when charged, will deliver an instantly fatal shock. A typical small pinch apparatus(21) has a 15 microfarad bank of 10,000 volt capacitors which deliver a waveform of 200,000 amps at 250 kilocycles. The concept was advanced, during early development work on a pulsed plasma thrustor, of having a bank of such low capacitance and inductance that it would "ring down," delivering several cycles of the damped sinusoidal waveform, during the motion of the current sheet in the accelerator. We now know that secondary discharges frustrate attempts to achieve this mode of operation. But electrical limitations also arise. A real capacitor, as we have discussed, has an inductance associated with it and thus a self-resonant frequency $f = 1/2\pi(L_c C)^{1/2}$. Paralleling a number of such capacitors decreases the effective inductance and increases the effective capacitance, but the product L_cC is invariant, neglecting the additional inductance of the connections. Thus, no bank of capacitors can achieve an oscillating discharge of frequency higher than the self-resonant frequency of the individual capacitor units.

We have been considering the discharge to be an inductance. The next approximation to its circuit element behavior is that of a time-varying inductance (the change in inductance resulting from the change in position of the current sheet). The ramifications of this representation, and other electrodynamic aspects of a transient discharge, are discussed in Appendix C.

3.2 SUSTAINED CURRENTS

In Chapter II we discussed the motivation for studying a pulsed plasma discharge with a current waveform substantially differing from the damped sinusoid characteristic of conventional capacitor banks. A constant-current waveform was our initial objective. Specifically, the current waveform should have the following characteristics:

1) fast rise
2) magnitude greater than 100,000 amps
3) approximately constant - i.e. "flat topped"
4) a few microseconds duration.

If one charges a length of ideal transmission line, e.g. lossless uniform coaxial cable, and then discharges it through a resistance, a constant-amplitude current flows in the resistance for twice the time required for an electromagnetic signal to propagate the length of the transmission line.[+] This well-known characteristic behavior of transmission lines is a convenient physical and mathematical starting point for our discussion of pulse-generating techniques.

We show in Appendix A that, for time less than the two-way transit time of the line, a uniform transmission line charged to voltage V_0 can be represented by the following equivalent circuit:

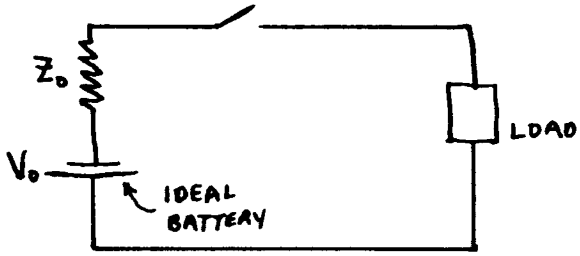

where Z_0 is the characteristic impedance of the line.

If the load is an inductance L and the switch is closed at $t = 0$, then the circuit current I is given by

$$I = \frac{V_0}{Z_0}\left(1 - e^{-Z_0 t/L}\right) \tag{3-4}$$

To achieve an asymptotic amplitude I_0, we must have $Z_0 = V_0/I_0$. If we take V_0 to be 10,000 volts and demand I_0 = 200,000 amperes, then Z_0 must be 50 milliohms. Paralleling 1,000 pieces of ordinary coaxial cable would yield

---

[+] Lewis and Wells afford a comprehensive discussion of transmission lines in "Millimicrosecond Pulse Techniques."(24)

a 50 milliohm system. However, the signal velocity in such cable is about half the speed of light, i.e. about 15 cm. per nano-second. Thus, a two-way time of 6 microseconds would require

$$3 \times 10^{-6} \text{ sec} \times 15 \times 10^{9} \frac{\text{cm.}}{\text{sec.}} = 450 \text{ meter lengths of cable}$$

So we would need a total of 450 kilometers of cable to generate our pulse from an actual distributed parameter transmission line. Even though special low-impedance cable might reduce this requirement by a factor of ten, and coaxial cable has been employed on such a gargantuan scale for the special pulse-generating requirements of the Astron thermonuclear research program,(25) the use of cable is not physically or economically feasible for most laboratories. We therefore turn to the question of how transmission-line performance may be obtained from a lumped-element circuit.

3.3 THE LADDER NETWORK

The partial differential equations for a transmission line can be obtained by considering the differential limit of an L-C ladder[+] network

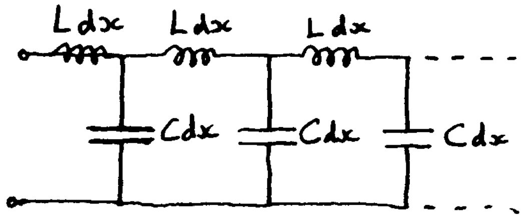

[+] So-called because of the structural appearance of its schematic diagram.

where L and C are respectively the inductance and capacitance per unit length. An obvious lumped approximation is then:

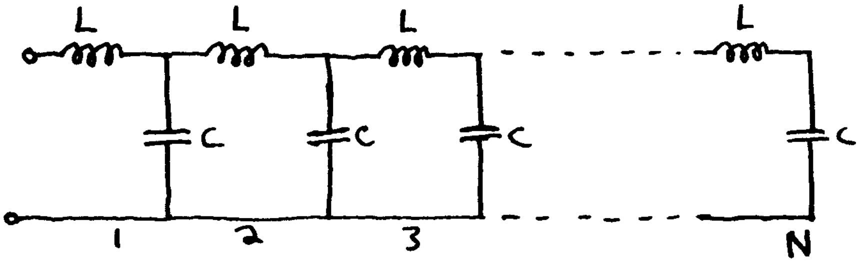

Such a ladder network equipped with output terminals at the end (section N) would be regarded as an N-th order L-section low-pass filter network in the conventional sinusoidal steady-state domain of electrical engineering. Its two-terminal transient response, however, approximates that of a transmission line having characteristic impedance $Z_0 = (L/C)^{1/2}$ and one way transit time $\tau = N(LC)^{1/2}$, but when the network is discharged into a resistive load, the response differs from that of the uniform distributed line in that the current waveform has non-zero rise time, overshoot and ripple. Furthermore, as we noted in Section (3-1), we must consider the effective series inductance of the capacitors, which modifies the equi-section ladder network circuit as indicated:

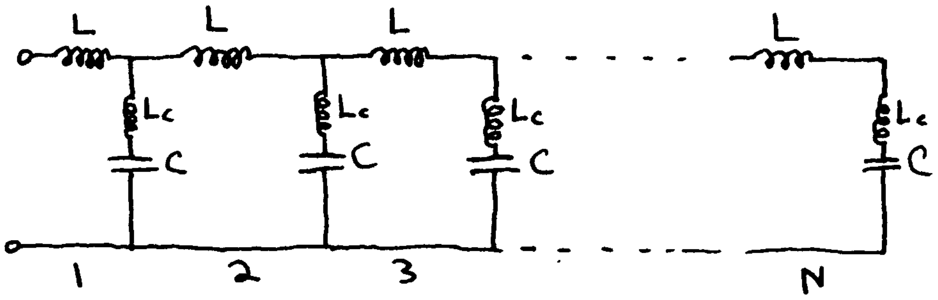

where L_c denotes the "parasitic," i.e. unwanted, self-inductance of the capacitor and its connection to the network. Consideration of the effects of this parasitic inductance, and the number of sections, N, on the current waveform, is deferred until Appendix A; we must first establish that the lumped network transmission line approximation is more readily realizable than one and one-half megafeet of coaxial cable.

It is convenient to adopt the following units:

inductance :	nanohenries
capacitance:	microfarads
time :	microseconds
resistance :	milliohms

Now a lossless uniform transmission line--and to a first approximation its lumped ladder network equivalent--can be specified by

L_T - total inductance

C_T - total capacitance

Then in our units these quantities depend on the line one-way time τ, and the characteristic impedance Z_0, through the relations

$$L_T = \tau Z_0 \tag{3-5}$$

$$C_T = \frac{1000\tau}{Z_0} \tag{3-6}$$

So for a 50 milliohm 3 microsecond line:

$$L_T = 150 \text{ nanohenries}$$

$$C_T = 60 \text{ microfarads}$$

It thus proves to be feasible to construct a lumped-circuit transmission line approximation in the regime of interest. A commercial type 10 kilovolt energy-storage capacitor runs to some 1000 cm^3 per microfarad. The inductance requirement is actually the crucial factor in the feasibility of the ladder network approach: a few nanohenries would be difficult to realize while providing for capacitor connections and necessary insulation; a millihenry would require some type of coil having very low resistance while withstanding the electromagnetic stresses induced by currents of some hundreds of kiloamperes. Now two 25 cm. wide parallel plates spaced 1 cm. apart have an inductance of about 50 nanohenries per meter. Thus we can realize a pulse-forming network approximating a low-impedance transmission-line pulse generator by connecting lumped capacitances at intervals along the distributed inductance of parallel-plate conductors which are a few meters long.

This scheme has one important advantage for experimentation: versatility. A number of capacitor connection points can be provided along the parallel-plate inductance. The effective impedance of the network can thus be changed by varying the number of capacitor units and their spacing. Concentrating capacitance at one point yields a damped sinusoidal waveform, as does the conventional capacitor bank, but with easily variable frequency and amplitude. A multitude of other waveforms can be obtained from the various other accessible network configurations. The physical realization of this versatile continuous-inductance ladder network, and other components of the experimental apparatus are discussed in Chapter IV; several different current waveforms occur with the experimental results in Chapters V and VI.

3.4 OTHER TECHNIQUES

There is, of course, a vast body of electrical engineering literature on circuit synthesis techniques largely applicable to the small-signal sinusoidal steady state, which aim to produce a network having a specified input-output transfer response. The problem of transient high-power network response was attacked by Guillemin and co-workers at M.I.T.(26) (Radiation Laboratory) in the wartime radar development program. While the application of their techniques to a desired impedance level of some milliohms, instead of the 50 ohms range of the radar work, proceeds in a straightforward fashion,(27,28) there are definite disadvantages in their practical application to our purposes. One must a priori specify the required current, and then obtain from the analysis certain definite values of capacitance and inductance. Each desired waveform requires its own set of circuit elements; thus experimental flexibility is lacking. The physical realization of the separate small-value inductances is troublesome, as is the avoidance of unwanted inductance in the connections. Most importantly, high-voltage energy storage capacitors are not available in arbitrary sizes, and for reasonable cost must be procured in a batch all having the same nominal capacitance. In Appendix A we take up a systematic computation technique to adjust the inductance values of the ladder network to produce a desired waveform under the constraint that capacitance values are fixed.

A novel technique has recently been developed by Hayworth(29) and Gooding at General Dynamics/Convair. Desiring to obtain a very low-inductance capacitor bank to power a coaxial gun, they constructed a single large capacitor in a toroidal configuration to replace the massive assemblage of paralleled units previously attached in low-inductance fashion to the breech assembly of their gun. They were surprised to find a rather constant-amplitude waveform, instead of the usual damped sinusoidal current, but quickly realized that their "capacitor" was in fact an extremely low impedance distributed transmission line. The theory and practice of these energy-storage units are developed in Ref. 29, and it is now understood how the winding and geometry can be adjusted also to yield non-constant current waveforms. It seems that this distributed pulse-line innovation is the best possible low-mass, low impedance, fast rise-time system for application to a specific requirement. However, such units are not commercially available, and a separate custom-made unit is required for each waveform.

CHAPTER IV

EXPERIMENTAL APPARATUS

4.1 DISCHARGE CHAMBER AND SWITCH

A schematic cross-section view of the discharge chamber is shown in Fig. 4-1. The chamber is a cylindrical volume, 8" in diameter and 2" high, with aluminum electrodes and a glass insulator. The switch chamber is located directly above the discharge chamber, and is identical to the discharge chamber, but with a plastic insert added. This is an 8" diameter version of the gas-triggered pinch-discharge switch described in Reference 30, which in turn evolved from an earlier inverse-pinch configuration switch.(31)

4.2 OPERATING SEQUENCE

A mechanical pump evacuates the switch and discharge chamber to less than 1 micron pressure, the switch is then sealed off from the system. Argon is admitted to a pressure of several millimeters, and then evacuated to establish the desired operating pressure in the discharge chamber. The pressure is monitored by a Pirani gauge which has been calibrated against a McLeod gauge at the operating pressure. The valve which then seals off the discharge chamber seats directly into the electrode, so that an unbroken electrode

JPR 2507A

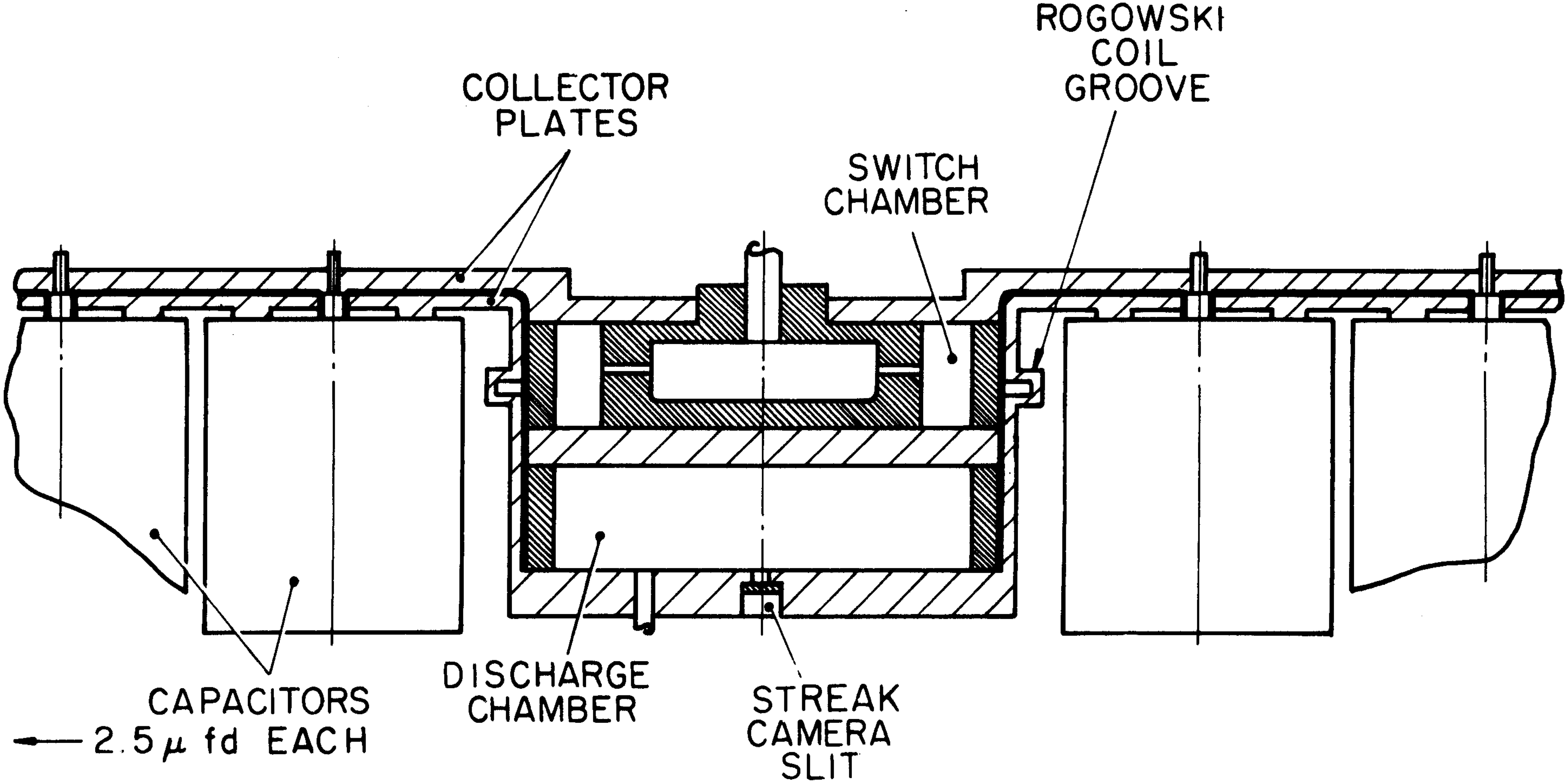

EXPERIMENTAL APPARATUS (SCHEMATIC)

FIGURE 4-1

surface is available to the discharge. A Variac-controlled high voltage power supply charges the capacitor bank; the Variac is manually regulated to hold the charging current to less than 10 milliamperes to avoid serious overloading of the high voltage supply. The two electrodes of the discharge chamber are connected by a 1000 ohm resistor, hence, in the absence of sensible current, these electrodes are at the same potential, and the entire voltage is impressed across the vacuum gap of the switch. Charging continues until the capacitor voltage is slightly in excess of 10,000 volts; the high-voltage supply is then disconnected, and the capacitors slowly discharge through a 100-megohm bleed resistance. At 10,000 volts a spring-loaded valve is manually actuated, admitting gas to the switch chamber. The switch breaks down, transferring the entire voltage to the discharge chamber, which in turn breaks down, and the high-current discharge occurs.

4.3 THE PULSE-FORMING NETWORK

Two parallel-plate transmission assemblies, or "wings," each about ten feet long, extend diametrally from the discharge assembly. Each wing has twenty equally-spaced capacitor stations; each station can hold 0, 1, or 2 capacitors. A schematic top view of the arrangement is shown in Fig. 4-2, which also shows the numbering scheme by which we specify an arrangement of capacitors; an example suffices to illustrate the notation: (1, 2, 21, 22) 1; (3-6, 23-26) 2 denotes a

AP25-JPR-4021-65

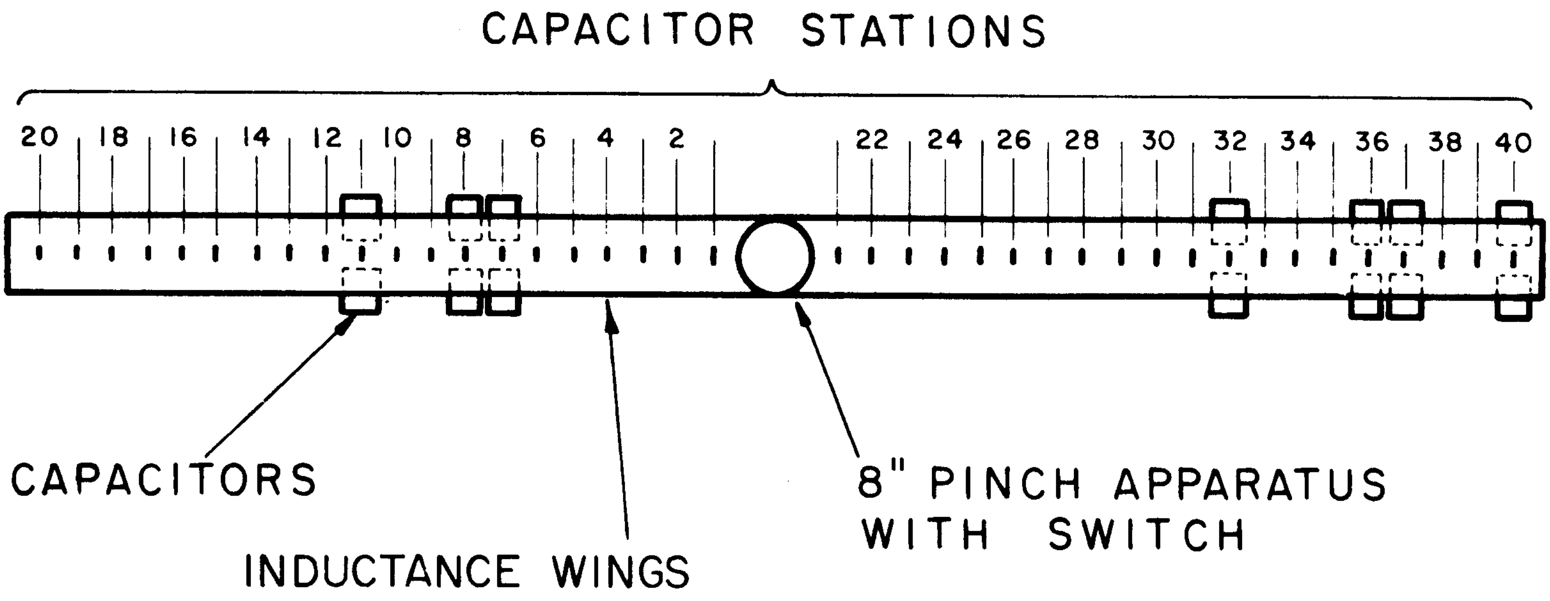

TOP VIEW OF PULSE FORMING NETWORK
(SCHEMATIC)

FIGURE 4-2

symmetric capacitor arrangement in which stations 1, 2, 21, and 22 have one capacitor, two capacitors occupy stations 3 through 6, and 23 through 26, inclusive, and the unspecified stations have no capacitors attached. The capacitors currently in use (see Fig. 4-3) are 2.5 microfarad 10,000 volt units manufactured for us by the Aerovox Corporation as their type number PX50D12. While the relatively thin central stud contributes excessively to the self-inductance of the unit, and failure to hold tolerances in vertical and horizontal plane placement of the contact surfaces posed some problems in assembly of the pulse-forming network, these units have given satisfactory service and, at a unit cost of under $50, represent a favorable cost/performance compromise.+ A schematic cross-section view of the network construction is shown in Fig. 4-4, and an over-all photographic view of the apparatus in Fig. 4-5.

4.4 ELECTRICAL CHARACTERISTICS

In pulsed discharge work resistive impedances are so small, and inductive effects so ubiquitous, that the conventional method of measuring current by monitoring the voltage across a series resistance in the circuit is extremely difficult: instead, the Rogowski (or Rogovsky) coil (or "belt") is generally used (Ref. 12, p. 164; Ref. 32, p. 947). The Rogowski coil is

---

+The Sangamo Electric Company offers capacitors having similar performance and cost.

AP25-R4112-66

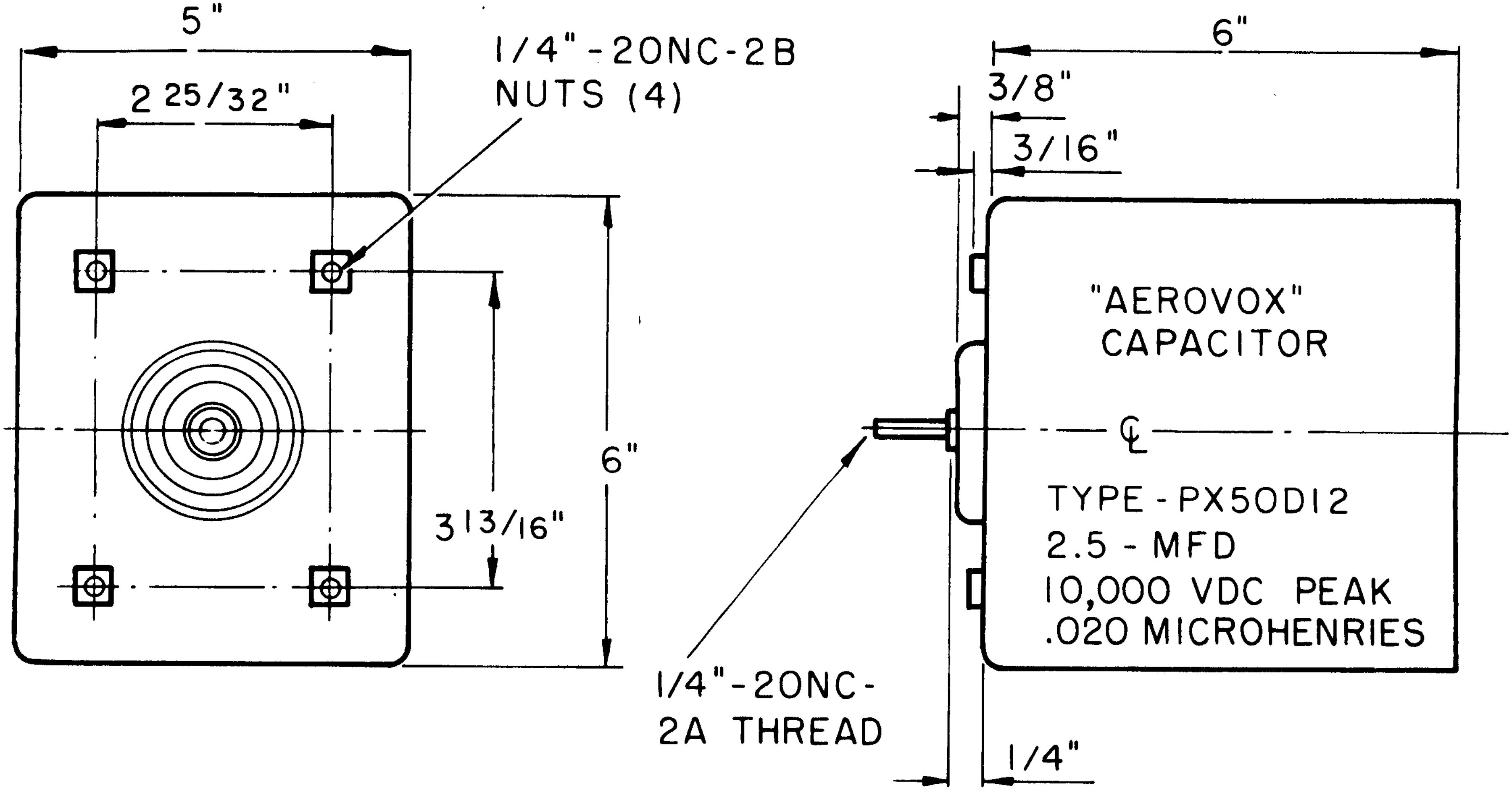

CAPACITOR UNITS

FIGURE 4-3

AP25-JPR-4017

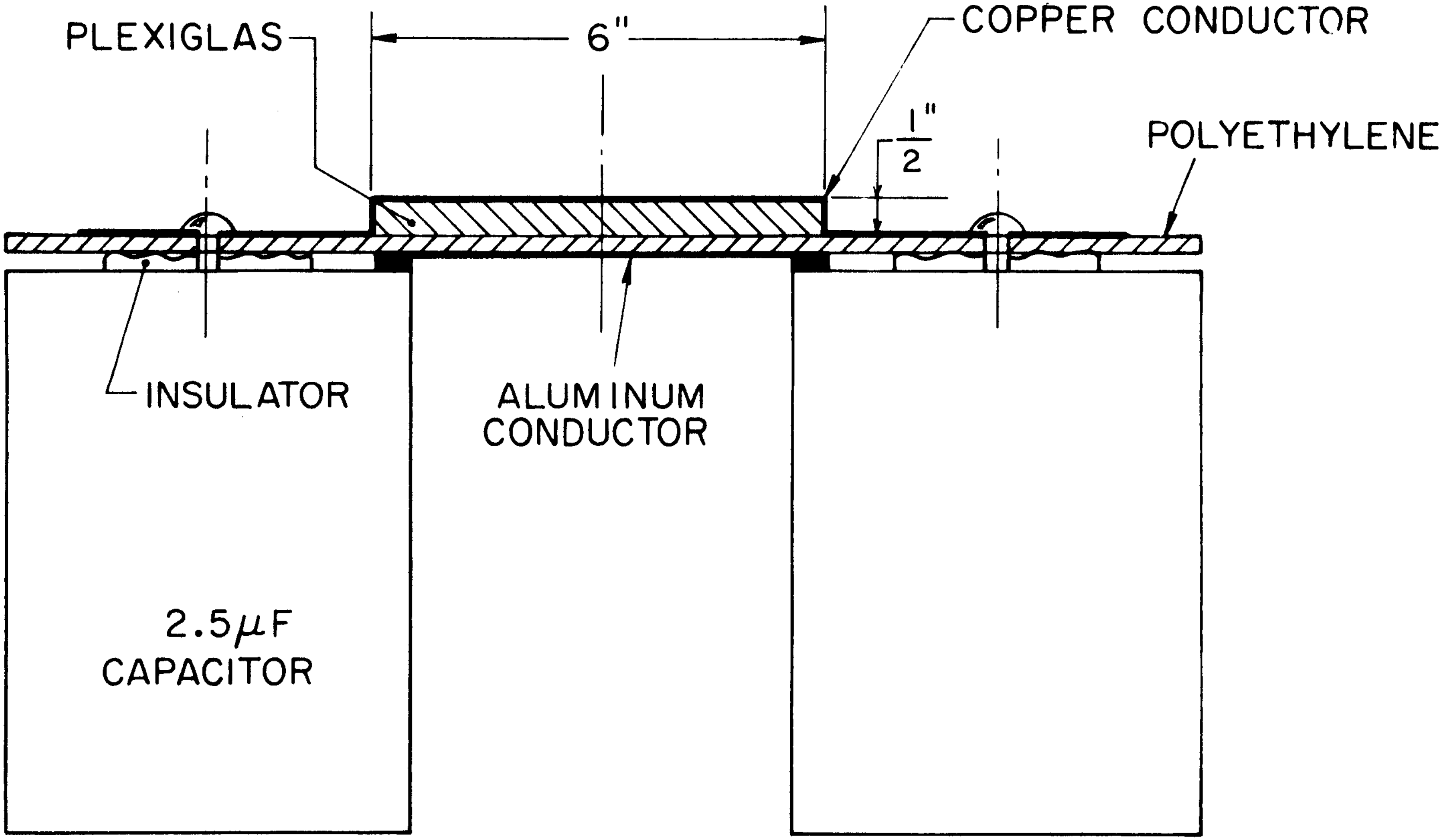

PULSE FORMING NETWORK CROSS SECTION (SCHEMATIC)

FIGURE 4-4

AP25-P16-65

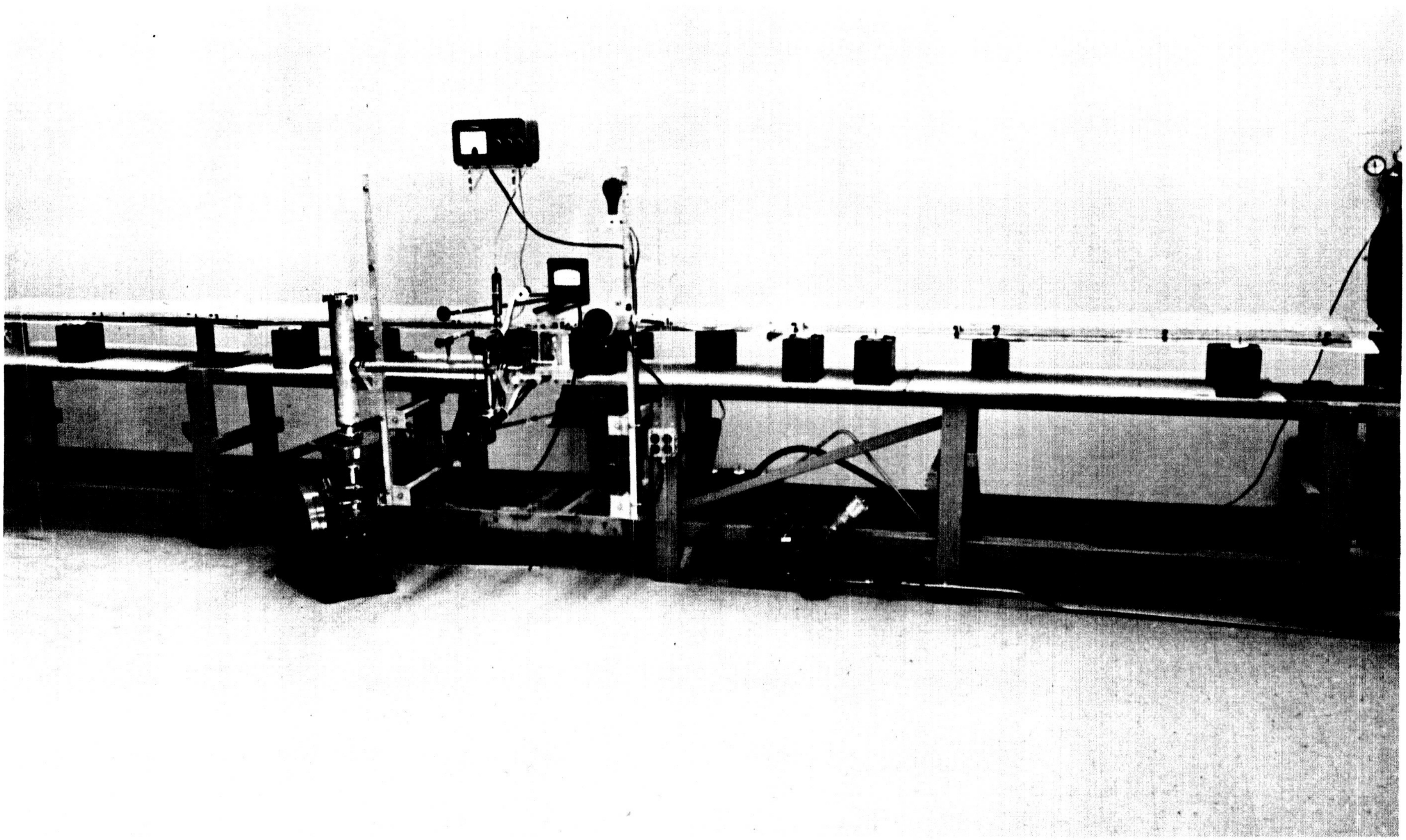

VIEW OF PULSE FORMING NETWORK

FIGURE 4-5

located in the groove indicated in Fig. 4-1, where it "sees" the total current flowing through the switch (the inductance penalty for this convenient location is a negligible 0.15 nanohenry) and generates a voltage proportional to dI/dt, the time rate of change of the total current. This signal is passively integrated by an RC circuit of adequate ($\approx$ 200 μsec) time constant.

If capacitance is lumped at one point, or corresponding points on the two wings, we have the situation of the conventional parallel-connected capacitor bank discharge, closely approximating a series RLC circuit. In this case, the current waveform is an exponentially damped sine wave. Knowing the voltage and capacitance, and measuring the frequency and damping constant, we can infer the circuit inductance and the current amplitude. The calibration factor of the Rogowski coil-integrating circuit combination is obtained in this fashion, and by varying the disposition and number of the capacitors we obtain the estimates of the apparatus circuit characteristics displayed in Table 4-1.

Table 4-1
Circuit Characteristics of the Apparatus

Station-to-station inductance	~12 nanohenries
Front section inductance	~ 6 nanohenries
Inductance of capacitor and its connection to the line	~16 nanohenries
Discharge impedance	~ 5 milliohms
Switch and network resistance (two sided) .	~ 5 milliohms
Discharge plus switch inductance	~ 5 nanohenries

4.5 INSTRUMENTATION

In addition to the Rogowski coil, a magnetic probe(33) and rotating mirror streak camera were used in this investigation. On occasion, a Kerr cell shutter unit, operating in a pulse-to-close mode, was used in conjunction with the streak camera to provide a positive time reference on the photographic records.

The magnetic probe used is a conventional 3-turn pickup coil, directly attached to a length of miniature 50-ohm coaxial cable. A glass tube, 5 mm O.D., vacuum-sealed to the glass insulator wall of the discharge chamber, extends radially to within 1/2" of the center. (The glass fails after a few shots if it extends completely into the central core of the pinch.) The magnetic probe can be positioned freely in the glass tube. With the coil axis perpendicular to an azimuthal plane, the probe signal is proportional to $\partial B/\partial t$, the time rate of change of the azimuthal magnetic field, at the probe radial position. A passive RC integrator ($\approx$ 200 μsec time constant) was used to obtain a record of the magnetic field, as a function of time.

For an axially-symmetric discharge with axial current flow, the current density j and the (azimuthal) magnetic field B are related by:

$$\frac{1}{r}\frac{\partial(Br)}{\partial r} = \mu_0 j \quad (\mathrm{MKS}) \qquad (4\text{-}1)$$

From a series of magnetic probe oscilloscope traces at several radii, we determine the values of B at a selected time for each of the radial probe positions, form the quantities ($B r$), and plot these data. A curve is then faired through the data points, and the values of $j(r)$ determined, by graphical differentiation, from Eq. (4-1). Of course, the discharge must have adequate shot-to-shot reproducibility in order that the cross-plot reconstruction of $B(r)$ from $B(t)$ can be performed meaningfully. The standard precaution was followed of taking a 3-shot overlay at each probe position; the records are generally reproducible to within one or two trace widths. Differentiating experimental data is, of course, an uncertainty magnifying process.

The Rogowski coil and magnetic probe signals are displayed on a Tektronix Type 555 dual-beam oscilloscope, whose time-base was referred to a Tektronix Type 181 time-mark generator. The graticule on this oscilloscope is an integral part of the cathode-ray tube, thus eliminating the parallax error occurring when the graticule is displaced from the surface of the tube. The use of ASA 3000-speed Polaroid film, together with an f1.9 lens, allows the single-shot transients to be photographed readily at a 1/2 microsecond per centimeter sweep speed.

An AVCO Corporation Type MC300 Model 2 rotating-mirror camera was used to obtain streak photographs of the discharge. This camera was particularly well-suited for our purposes because of its continuous writing property: any luminosity is always imaged somewhere on one of two pieces of film, so there is no need for synchronizing the discharge initiation to the position of the mirror. Since our switch is gas-triggered, and not initiated by an electrical impulse, such synchronizing could not readily be accomplished. The camera has a magnet on the rotating mirror shaft which induces two electrical pulses per revolution; displaying this pulse train allows evaluation of the camera writing speed at the instant of discharge. Pressurized nitrogen drives the mirror turbine, which is brought up to speed, about 3000 revolutions per second, while the capacitors are being charged. The sequence of events shown in the block-diagram of Fig. 4-6 is as follows:

When the discharge is initiated by admitting gas to the switch, breakdown occurs with a rapid growth of current, and a voltage is induced in the Rogowski coil. This signal is fed to the external trigger input of the oscilloscope, initiating the sweep of the upper beam time-base, generally at 1 microsecond per centimeter. The lower beam sweep, at 100 microseconds per centimeter, is initiated by the firing of the upper beam. As the single sweeps of the two beams proceed, the integrated Rogowski coil signal, i.e. the total circuit current, and the mirror-speed pulse train are displayed through the vertical pre-amplifiers on the upper and lower beams, respectively. At sweep initiation, the scope + GATE signal is sent to a pulse generator, which, after an adjustable time-delay, delivers a pulse to the Kerr-cell power supply unit

AP25-4082-66

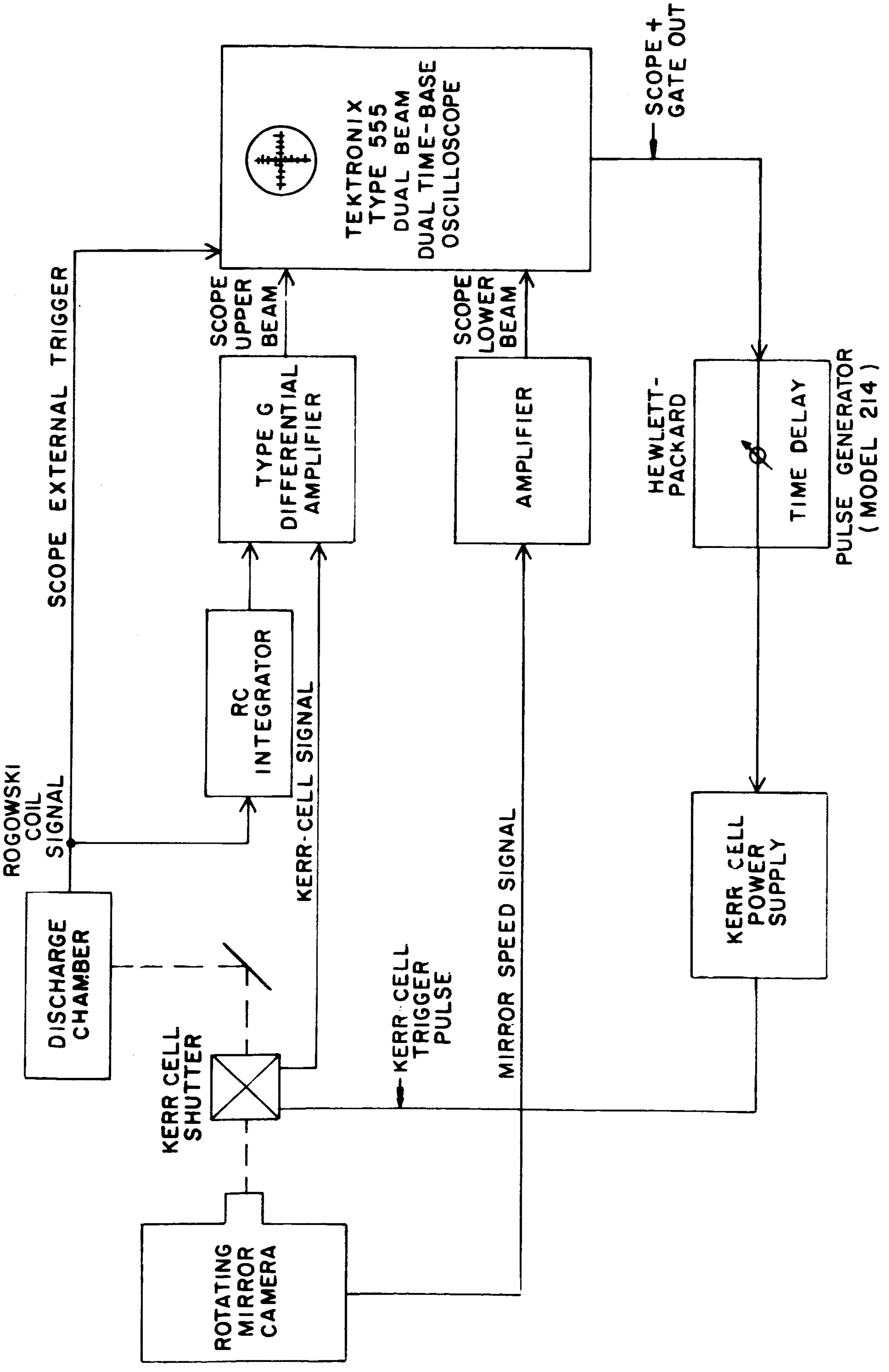

BLOCK DIAGRAM
STREAK PHOTOGRAPH OPERATION

FIGURE 4-6

which in turn triggers the Kerr-cell shutter, pulsing it closed for 50 nanoseconds, and producing a distinct thin black line on the streak photograph perpendicular to the time-axis. An attenuated sample of the 30 kilovolt shutter pulse is delivered to the differential amplifier which also receives the integrated Rogowski-coil signal, the sample thus appears as a distinctive narrow blip on the current trace, identifying the precise moment of shutter closure.

The combination of ASA 3000-speed (Polaroid) film (special film holders were fabricated so that the camera would take Polaroid film sheets), an f4.5 lens, and the intense luminosity of the discharge, provides more than adequate photographic sensitivity, despite the 88% intensity loss suffered by light passing through the "open" Kerr-cell.

For magnetic probe records, the signal (integrated or unintegrated) is fed to the lower beam vertical amplifier. The oscilloscope is triggered and the Rogowski coil signal displayed on the upper beam in the same fashion as for the streak photographs, but both beams are swept simultaneously by the upper-beam time base.

In either case, time is reckoned from the origin of the current trace. However, electrical noise, appearing as hash on the oscilloscope records, accompanies all high-current transient discharges, particularly at inception. Noise-elimination, a laboratory art not yet reduced to science, is essential to preserve the time origin on the records. Best results were obtained in these experiments by isolating the oscilloscope in a screen-room equpped with a low-pass filter in the power line, and avoiding any direct electrical contact to the apparatus. This is feasible since both the Rogowski coil and the magnetic probe couple inductively to the discharge. Their signals are transmitted over several feet of 50 ohm coaxial cable, through feed-through connections in the screen room wall, to the oscilloscope, but since the low output impedances of the pickup coils permit the signal cables to be properly terminated with their characteristic impedance, spurious effects due to cable reflection are avoided.

4.6 NETWORK RESPONSE

The ideal uniform line relationships, Eq. (3-5) and Eq. (3-6), are a serviceable guide to estimating the gross electrical characteristics of an equi-section network configuration; but it was necessary to resort to detailed calculation via digital computer to determine the feasibility of achieving a useful current waveform with a reasonable number of sections, and capacitors of minimal self-resonant frequency: capacitor cost is a steeply-rising function of self-resonant frequency. Estimated values of network parameters were used in this feasibility study; some details are presented in Appendix A.

In its most commonly used configuration, the network had one 2.5 microfarad capacitor at each even-numbered station of the inductance wings. The resulting current waveform, in a 100 micron argon discharge, is shown in Fig. 4-7, together with the computed waveform for this configuration, using the refined estimates of the network parameters given in Table 4-1. If the total inductance and capacitance of this configuration were uniformly distributed along an ideal line, discharging into a purely resistive 10 milliohm load, a rectangular current pulse would be produced. The amplitude and duration of this equivalent-line current are also shown in Fig. 4-7. Apparently the actual combined inductance of the switch, load, and front section of the network is slightly larger than that used in the computation, since the actual current rise-rate is somewhat less than calculated. But despite the implicit approximations, e.g. neglecting the time-dependent resistive losses in the metallic conductors and the capacitors themselves, representing the non-linear time-dependent impedance of the switch and discharge by an inductance-resistance combination, and neglecting the mutual inductance coupling of the capacitor connection and the network, direct calculation yields useful results. The initial overshoot evident in both the computed and observed waveforms is analogous to the Gibbs phenomenon occurring in the Fourier synthesis of a (steady state) square wave, and is inherent in representing a distributed line by a lumped

AP25-4090-66

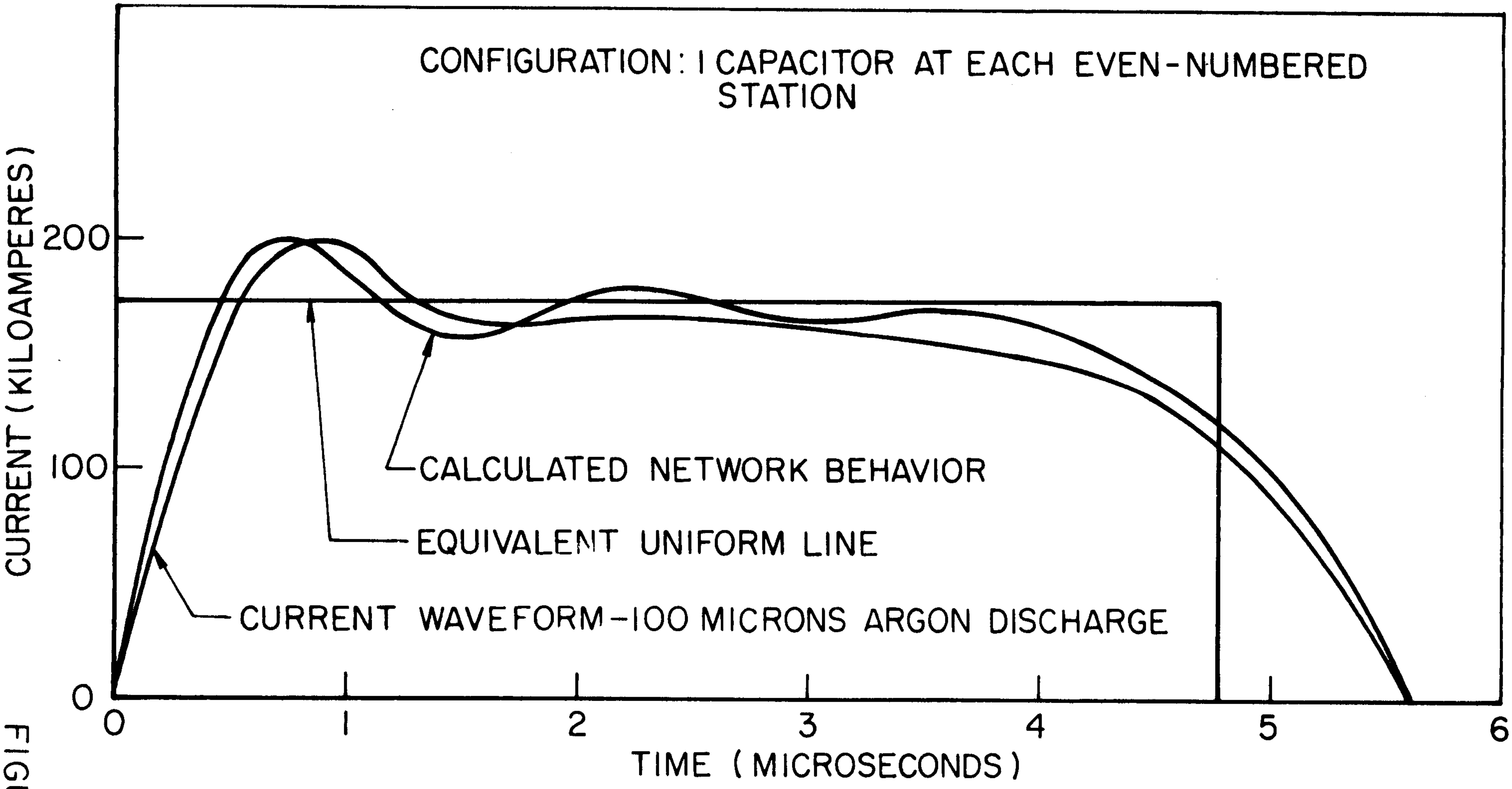

NETWORK BEHAVIOR IN UNIFORM LINE CONFIGURATION

FIGURE 4-7

network. However, as we show in Appendix A, an overshoot phenomena is also produced by a hypothetical uniform distributed line having a distributed shunt inductance equivalent to the parasitic inductance of the capacitors in the lumped circuit realization.

The overshoot can be removed by increasing the effective inductance of the load, at the cost of a more slowly rising current.

CHAPTER V

EXPERIMENTAL OBSERVATIONS

5.1 QUALITATIVE DISCHARGE BEHAVIOR

In developing a pulse-network current source, we hoped to avoid secondary breakdown and hence decoupling of the initial current sheet from the energy storage bank. We expected that if this were achieved a single-intense current sheet would be driven to the center under sustained acceleration.

Streak photographs show that this expectation is realized. Two streak photographs are displayed in Fig. 5-1, together with the corresponding driving-current waveforms. The rotating mirror of the camera sweeps the image of the slit in one electrode (Fig. 4-1) along the film, thus effectively producing a plot in the r-t plane of the trajectory of the inward moving luminosity front. Since the slit extends across a complete diameter, the photographic record is symmetric about the time axis to the extent that the discharge is symmetric. Small wire markers across the slit produce the horizontal black lines on the photographs, corresponding to 1" intervals along the diameter of the discharge.

The first photograph of Fig. 5-1 illustrates the typical behavior of a discharge driven by an oscillating current:

AP25-P14-1-65

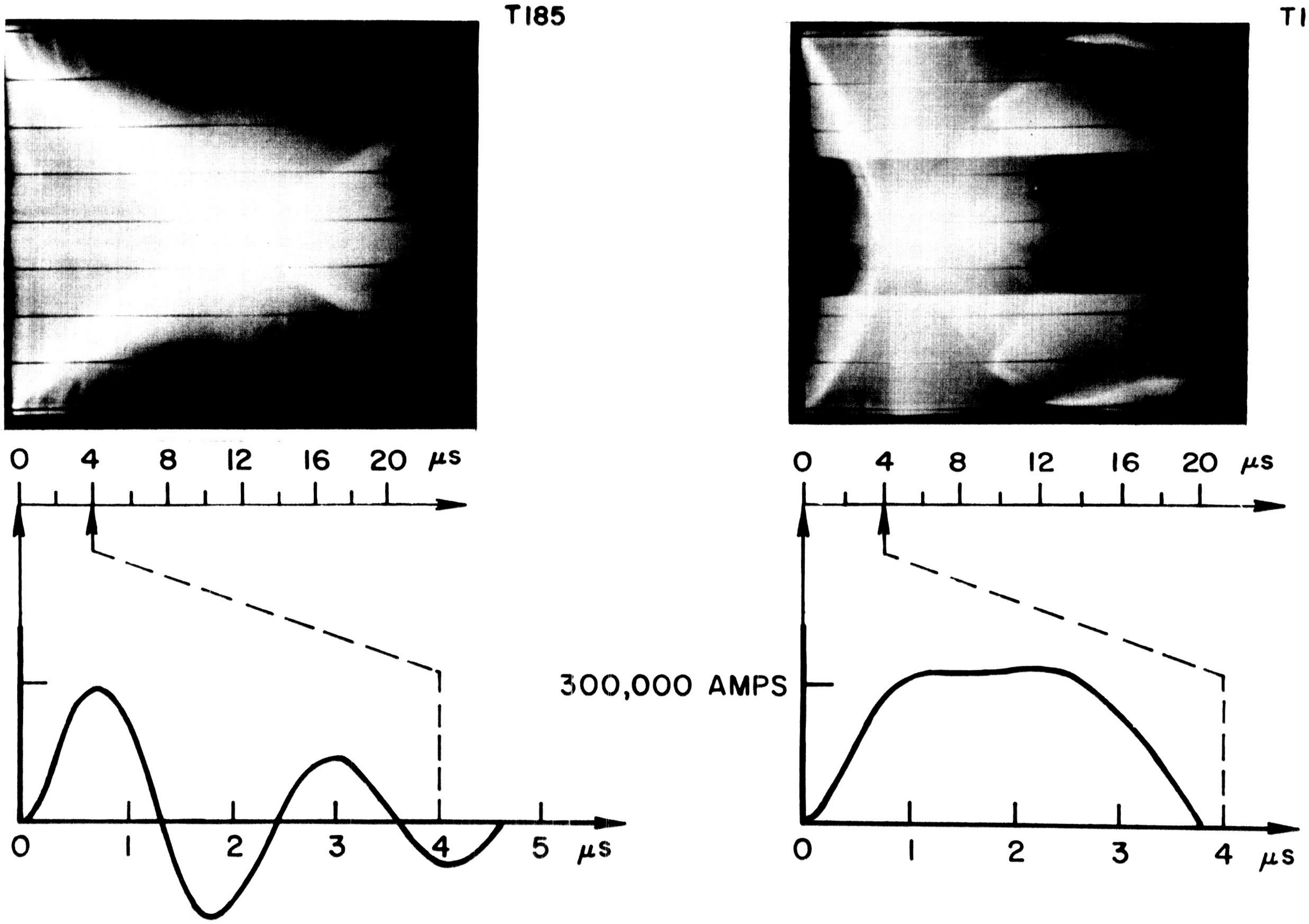

COMPARISON OF STREAK PHOTOGRAPHS
FOR TWO CURRENT WAVEFORMS

FIGURE 5-1

multiple luminous fronts initiate at the wall, at successive half cycles of the discharge, coalescing with the primary front which propagates inward with decreasing velocity. In the second photograph of Fig. 5-1, we see that only one luminous front is generated by the pulse current; the front accelerates throughout its inward excursion, in this instance reaching a terminal velocity 4 or 5 times as great as the sine-driven case. A neutral density filter placed across the central portion of the slit, which causes the dark band across the middle of the photograph, reduces the glare from the intense radiance of the pinch column and thus permits the front progress to be followed to the center.

The appearance of only one luminous front suggests strongly that only one current sheet is formed which is coupled to the external circuit throughout its entire radial motion. Magnetic probe records indicate that this is so. The probe output, for a cylindrically symmetric discharge, is proportional to the time derivative of the total current flowing inside the probe position. Thus, a signal appears which is essentially indicative of the local current density at the probe position. Two such magnetic probe records, for sine- and pulse-driving currents, are displayed in Fig. 5-2 for 3 radial positions. The signals are reproduced to the same scale. The rectangular pulse-driven current sheets are of substantially greater amplitude and propagate further than the corresponding sine-wave results. In Section (5-2), we

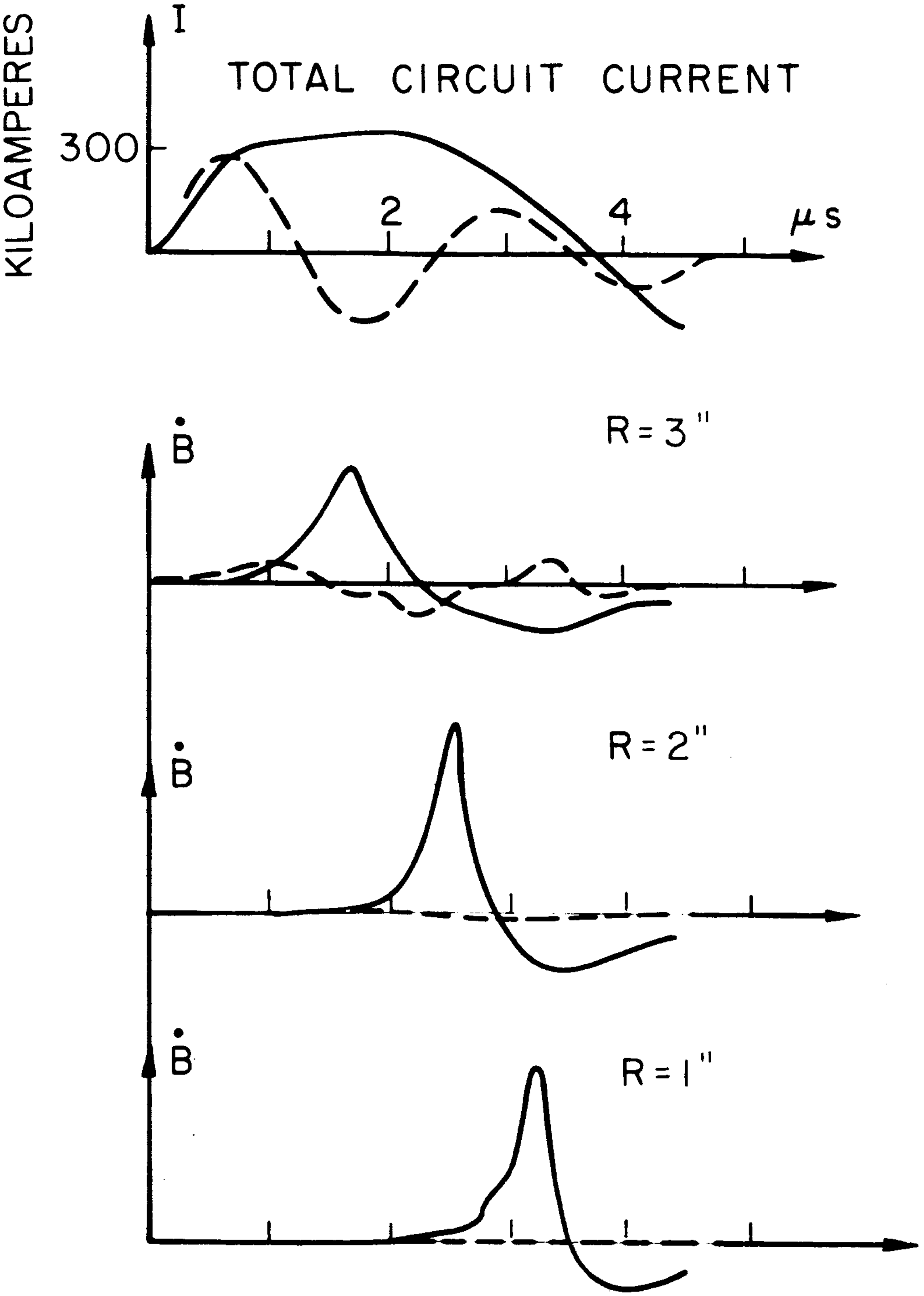

COMPARISON OF MAGNETIC PROBE RESPONSES
FOR TWO CURRENT WAVEFORMS

AP25-JPR-4020a-65

FIGURE 5-2

compare in detail the development and progress of the current sheets in pulse- and oscillating-current driven discharges.

The response of the discharge to four distinct waveforms is shown in Fig. 5-3. Secondary breakdowns are commonly somewhat loosely associated with "current reversal"; the streak photograph (a) clearly shows the formation of a second luminous front while the driving current maintains constant sign, although its amplitude fluctuates considerably. (However, since the discharge is predominantly inductive, the voltage is approximately proportional to the derivative of the current, and does change sign.) The current amplitude in part (b) does not vary as rapidly, and a single front is formed propagating with near-constant velocity.

Rise-time of the driving current has an important effect on the discharge dynamics. We have in part (c) of Fig. 5-3 a slowly-rising (approximately) sinusoidal driving current, while in part (d) the discharge is driven by our "standard" constant-current pulse. The slowly-rising discharge begins with a diffuse zone of luminosity; a well-defined luminous front is not apparent until the three-inch radius is reached. In contrast, the fast-rising waveforms (a), (b), and (d) all generate thin fronts from the beginning. Waveforms on (c) and (d) are of comparable peak amplitude, yet the pinch time is considerably less for the constant-current pulse.

The "precursor luminosity" is particularly evident in part (a) of Fig. 5-3. A region of intense luminosity appears at the center of the discharge column several tenths of a microsecond before the arrival of the initial luminous front.

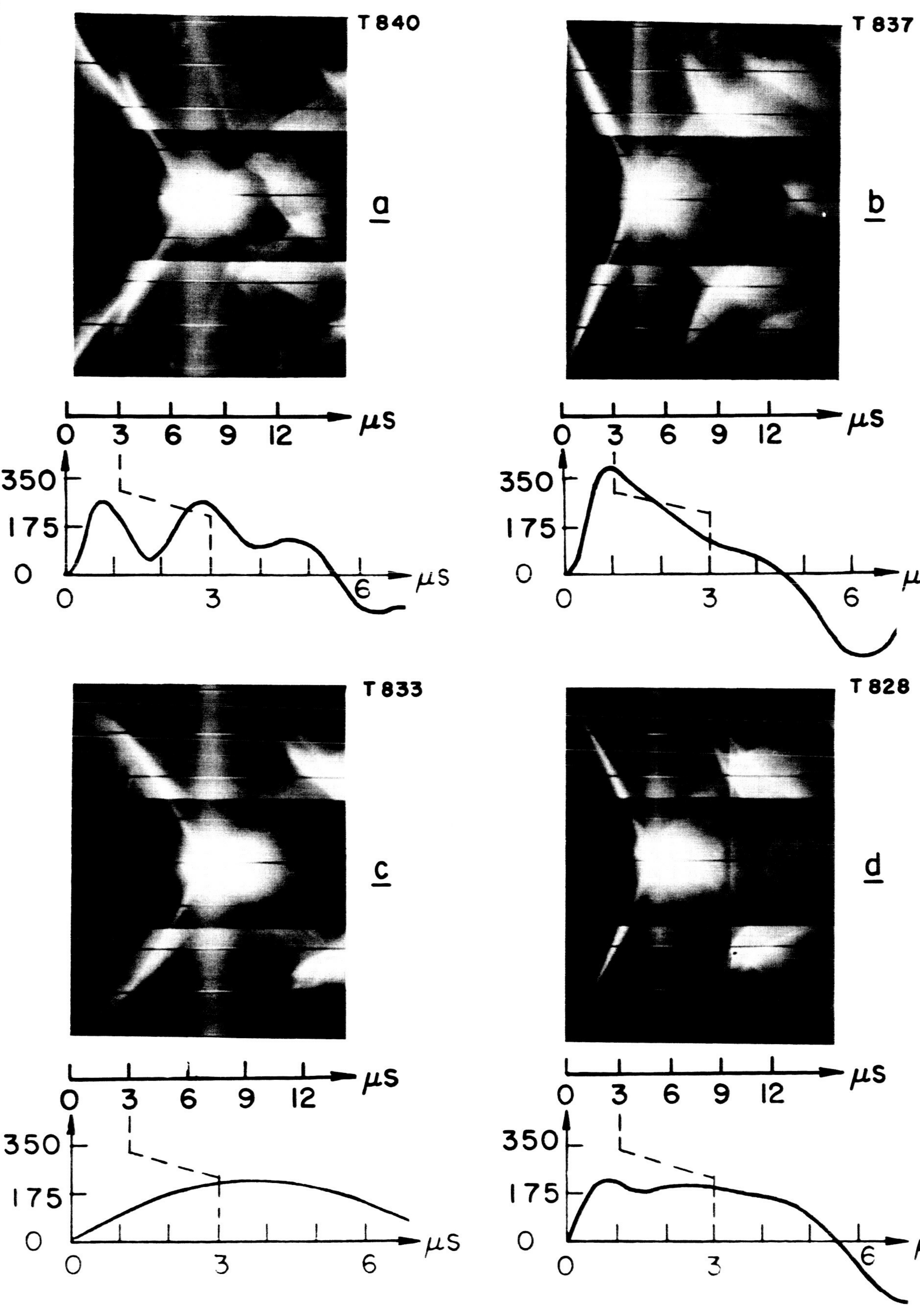

AD25-P29-65

EFFECT OF VARIOUS DRIVING CURRENTS ON 100 μ ARGON DISCHARGE

FIGURE 5-3

The same effect is evident in varying degrees on the other photographs, and was noted in earlier work.(21)

5.2 CURRENT DENSITIES

It is instructive to compare the temporal development of the spatial distribution of current density in the discharge chamber for two contrasting driving currents, an oscillating- and (approximately) constant- amplitude waveform. These waveforms, for brevity termed "sine" and "pulse" respectively, are displayed in Fig. 5-4; the peak amplitude and period of the oscillating current are comparable with the amplitude and duration of the positive pulse. Current densities for these two driving waveforms are plotted at successive times in Figs. 5-5(a-j) at intervals of approximately 0.56 microseconds. The markers labeled (a) through (j) on the waveforms of Fig. 5-4 identify the times at which the current density plots were made. The current densities, which are of order 100 megamperes/m^2, were obtained from the magnetic probe data by the technique discussed in Section (4-5).

In parts (a) - (c) of Fig. 5-5 we see the current sheets assembling at the wall and commencing their inward excursion. Both sine- and pulse-driven sheets exhibit characteristic thickness of about 1/2". The sine case has a definite, and as yet unexplained, negative current region appearing ahead of the main (positive) current sheet. At 2.2 microseconds the sine current has gone through almost a complete half-cycle, and the net circuit current, as shown in Fig. 5-4, is near zero, yet

AP25-A111-66

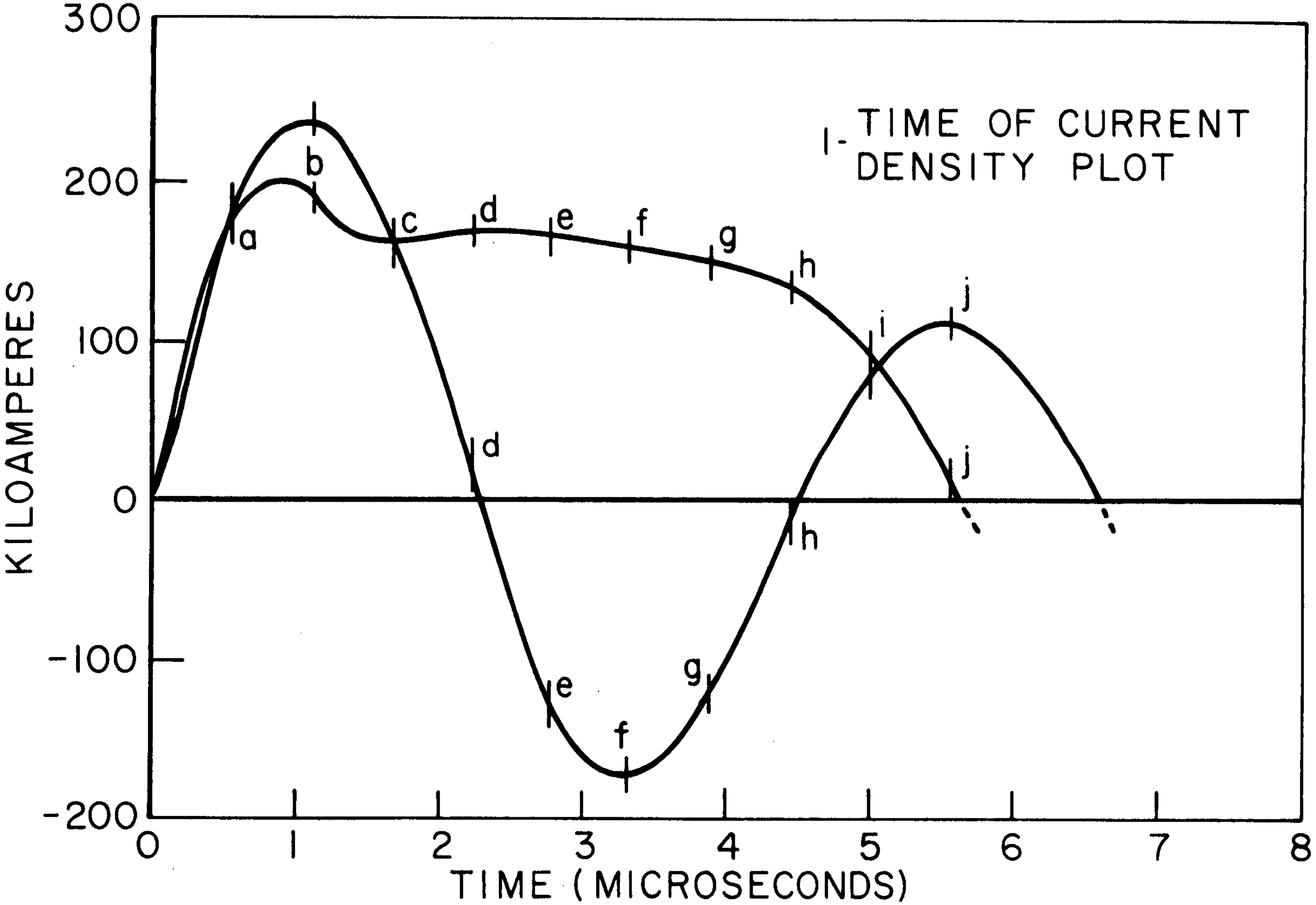

SINE AND PULSE DRIVING CURRENTS

FIGURE 5-4

the initial positive current sheet proceeds substantially unchanged; the net circuit current is balanced by the appearance of a negative current density zone immediately behind the initial positive sheet. As the (sine) driving current swings negative, however, the adjustment takes place at the outer boundary. Thus at 2.8 microseconds the sine-driven discharge has the complicated current distribution shown in (e), with two regions each of positive and negative current. In contrast, the pulse-driving current has been effectively constant for some two microseconds, and a single positive current sheet has progressed steadily inward, while leaving a wake of significant current density over a considerable portion of the chamber.

By 3.9 microseconds, the maximum current density for the pulse-driven case is now located in the central 1/2" radius of the discharge. Since we cannot follow the magnetic field distribution in this central region, the average current density is calculated from the magnetic field value at 1/2" radius. The wake continues to be driven to the center, as shown in parts (g) through (i).

The sine driving current has its maximum negative amplitude near 3.3 microseconds; at this time, (f), the negative sheet which appeared at the wall, Fig. 5-5(e), is now well-defined and proceeds inwards, as seen in (g). However, as the current algebraically increases, this negative sheet is decoupled from the external circuit, and the familiar sequence of current

AP25-R4110-66

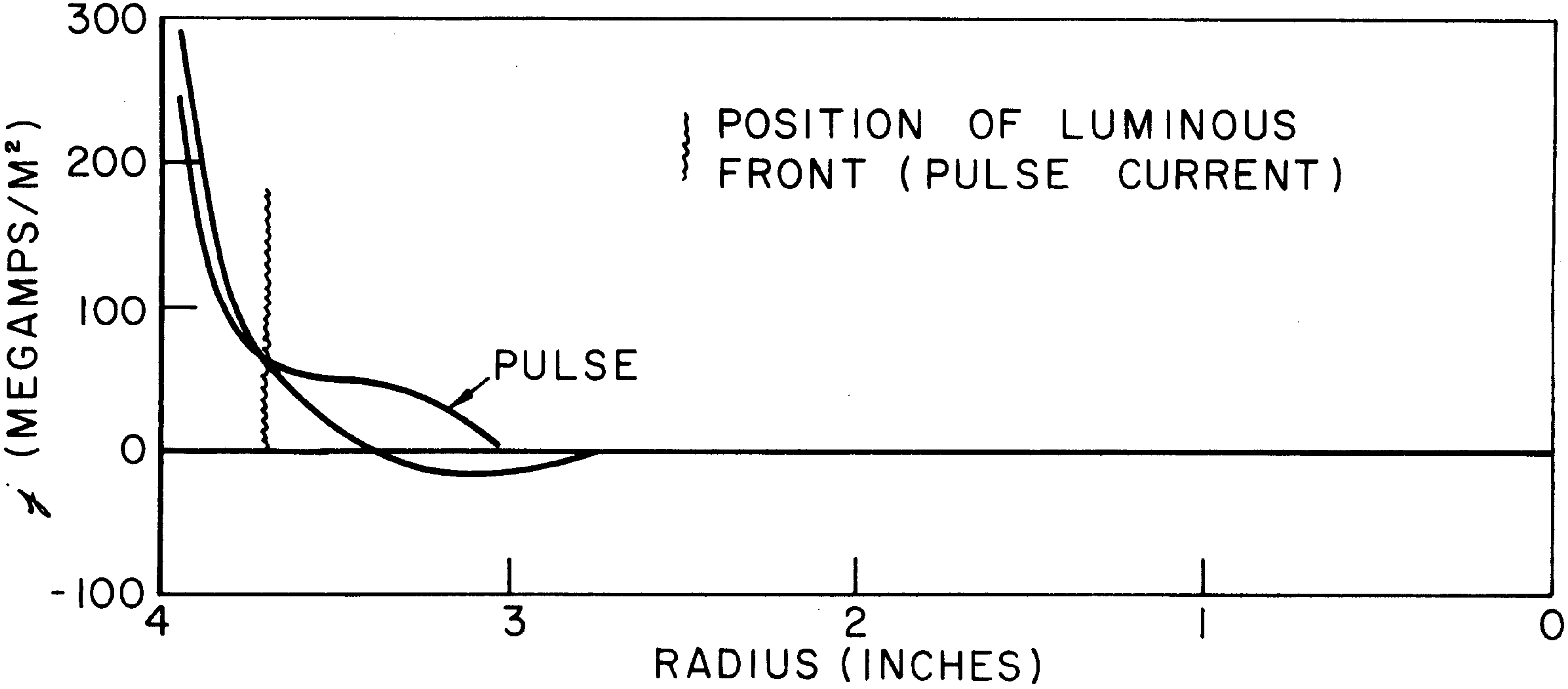

CURRENT DENSITY: 0.6 MICROSECONDS

FIGURE 5-5 (a)

AP25-R4109-66

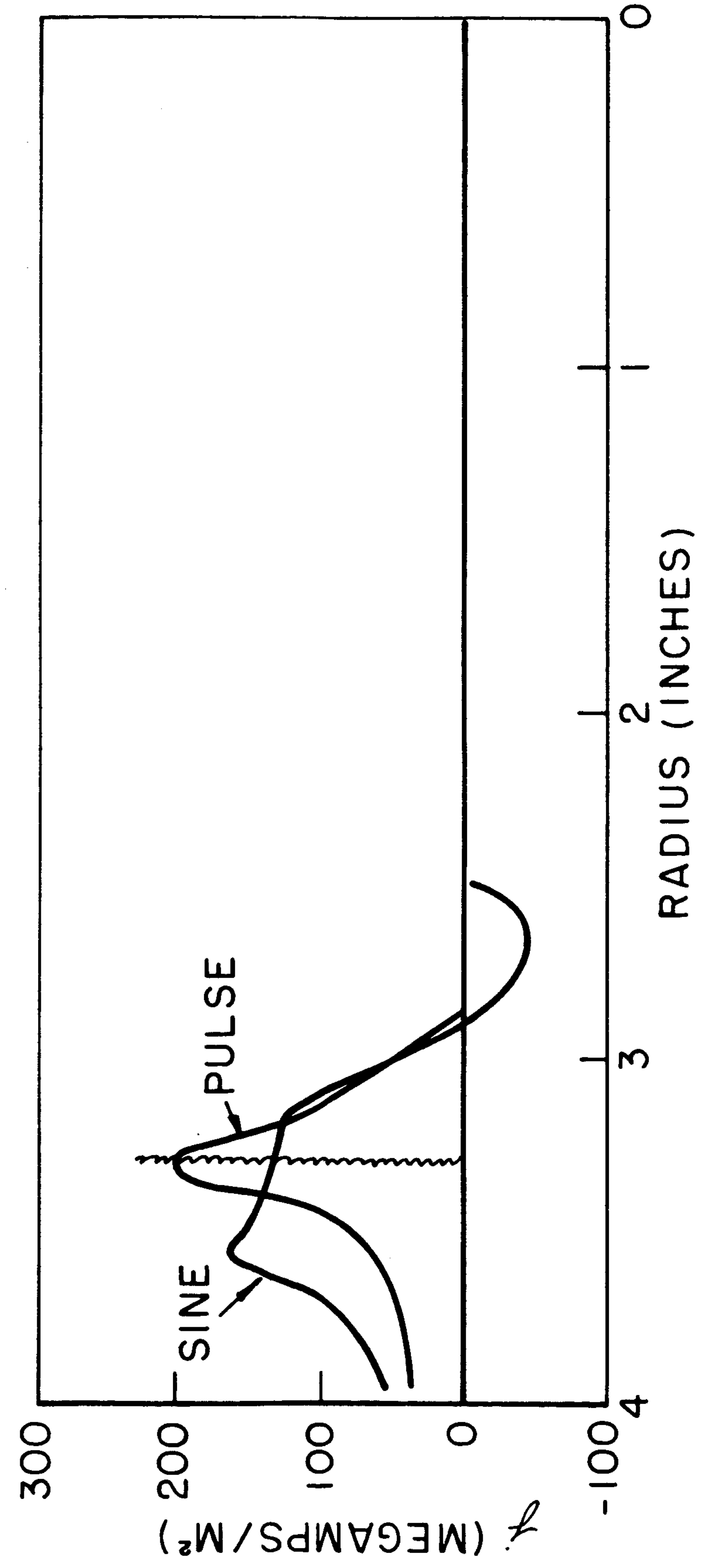

CURRENT DENSITY: 1.1 MICROSECONDS

FIGURE 5-5(b)

AP25-R4108-66

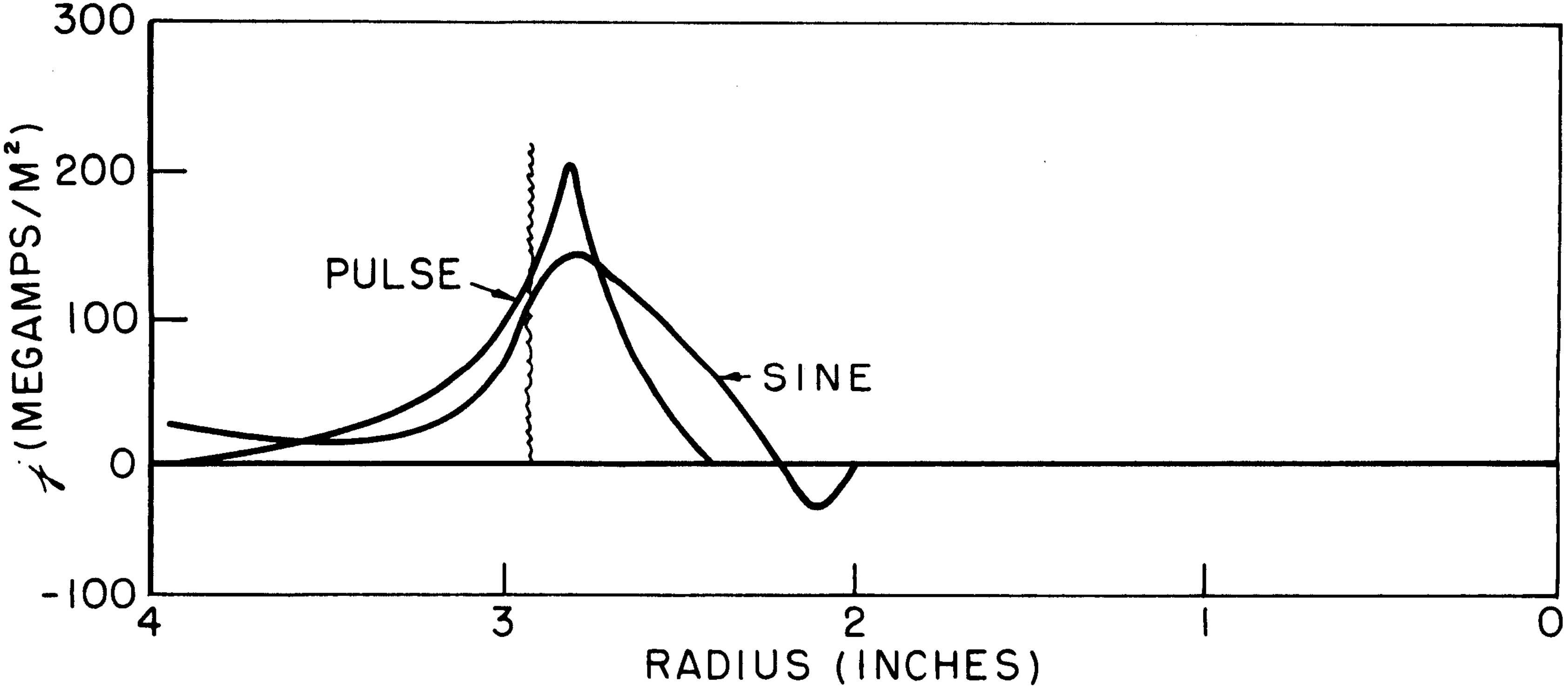

CURRENT DENSITY : 1.7 MICROSECONDS

FIGURE 5-5 (c)

AP25-R4107-66

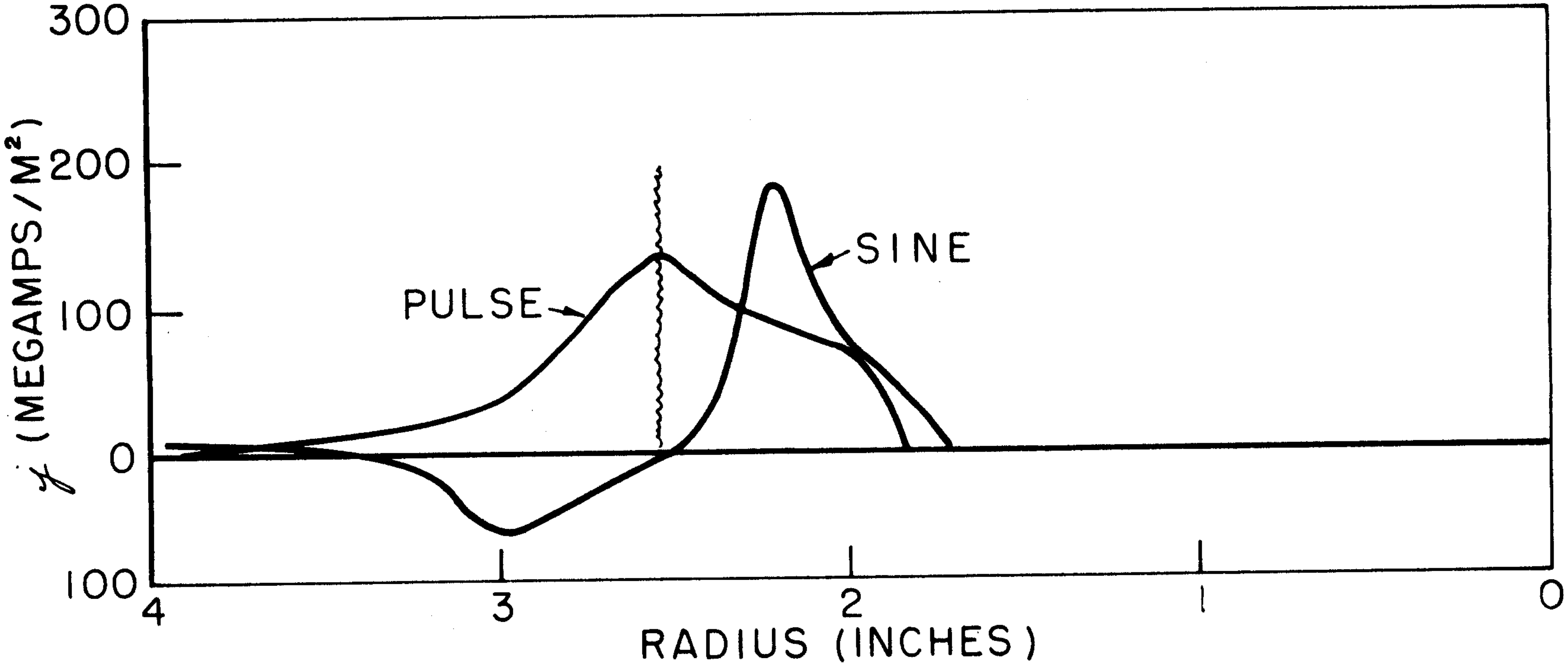

CURRENT DENSITY: 2.2 MICROSECONDS

FIGURE 5-5 (d)

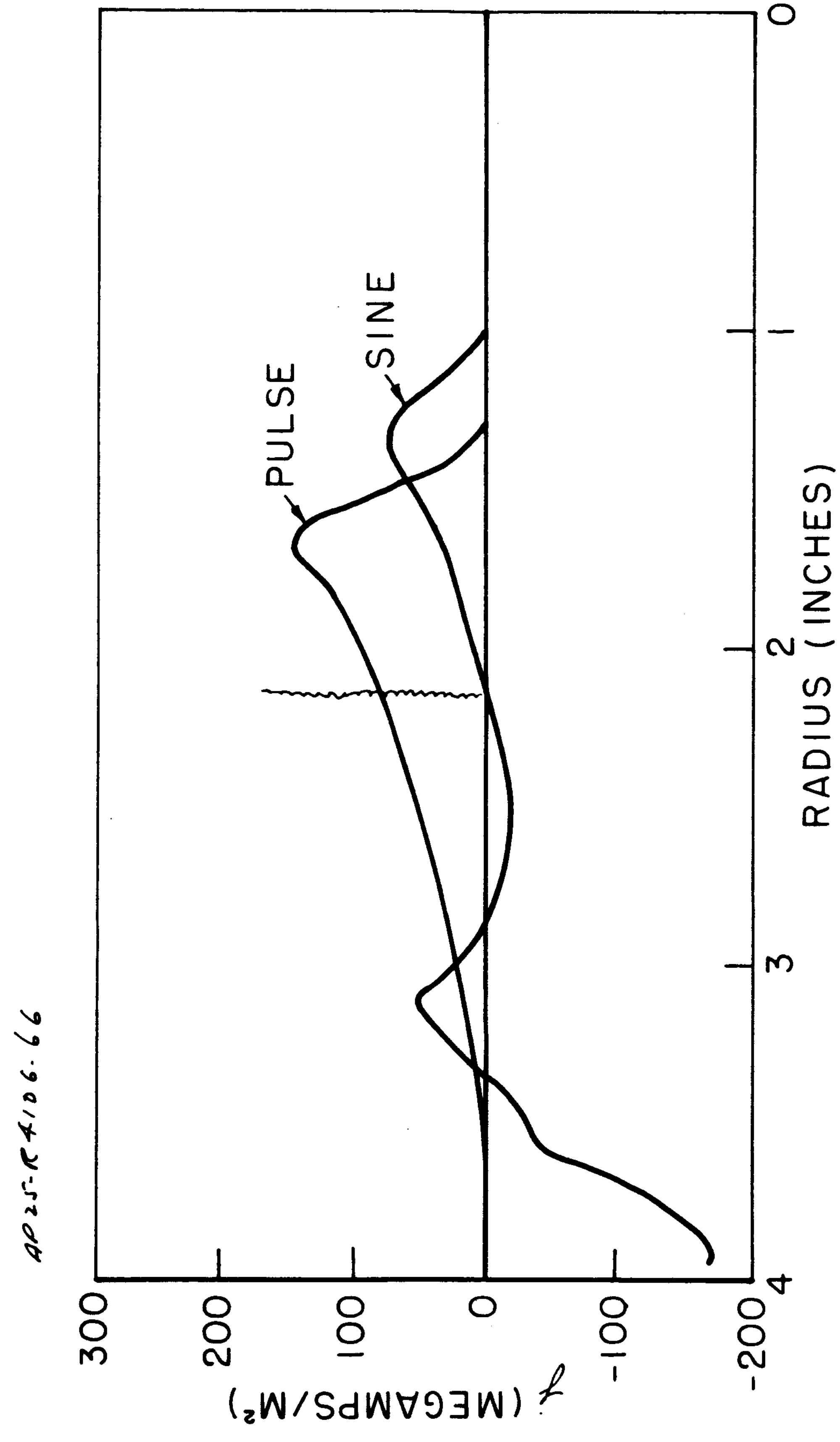

AP25-R4106.66

CURRENT DENSITY: 2.8 MICROSECONDS

FIGURE 5-5(e)

AP25-R4105-66

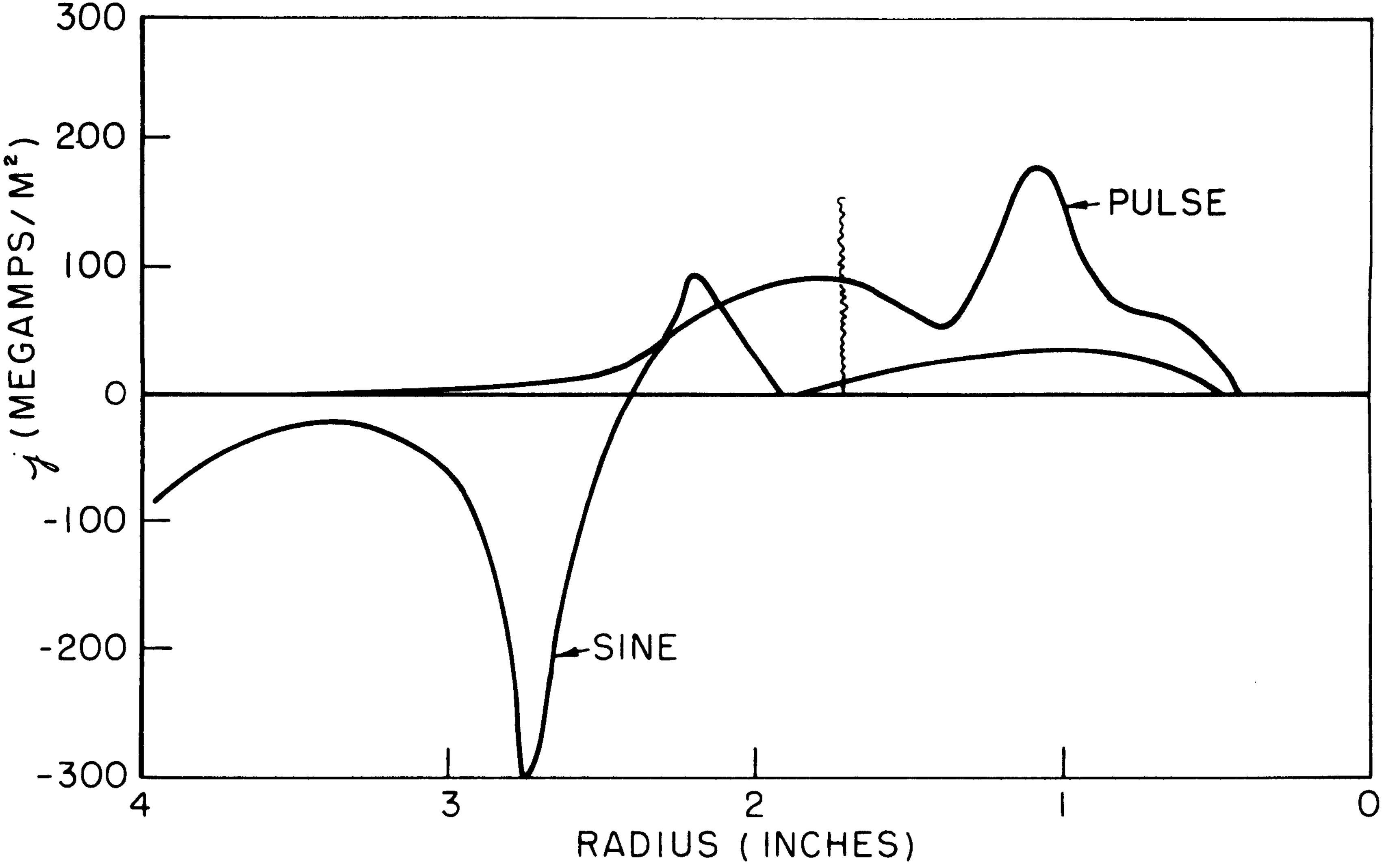

CURRENT DENSITY: 3.3 MICROSECONDS

FIGURE 5-5(f)

AP25-R4/03-66

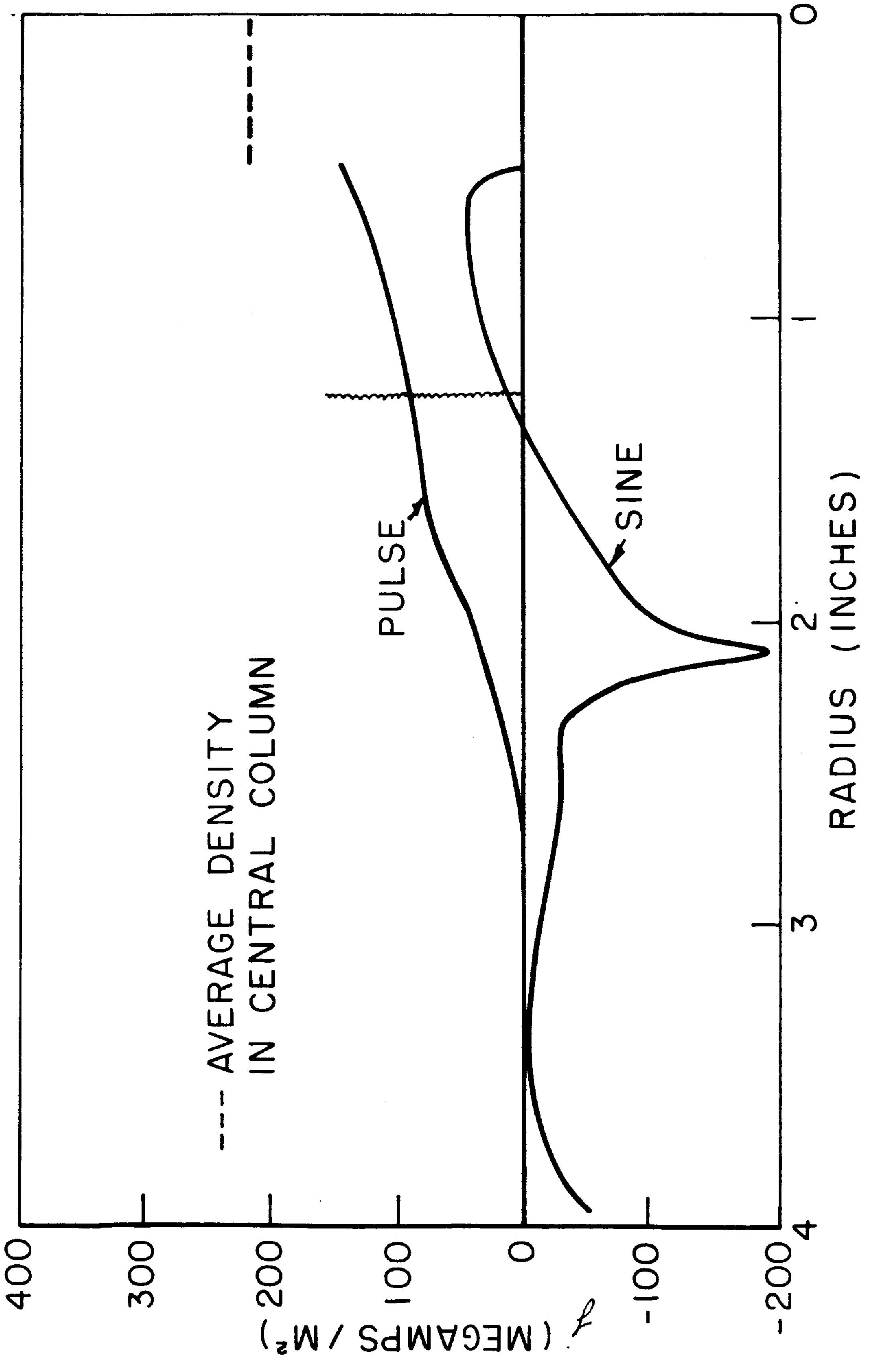

CURRENT DENSITY: 3.9 MICROSECONDS

FIGURE 5-5 (g)

AP25-R4104-66

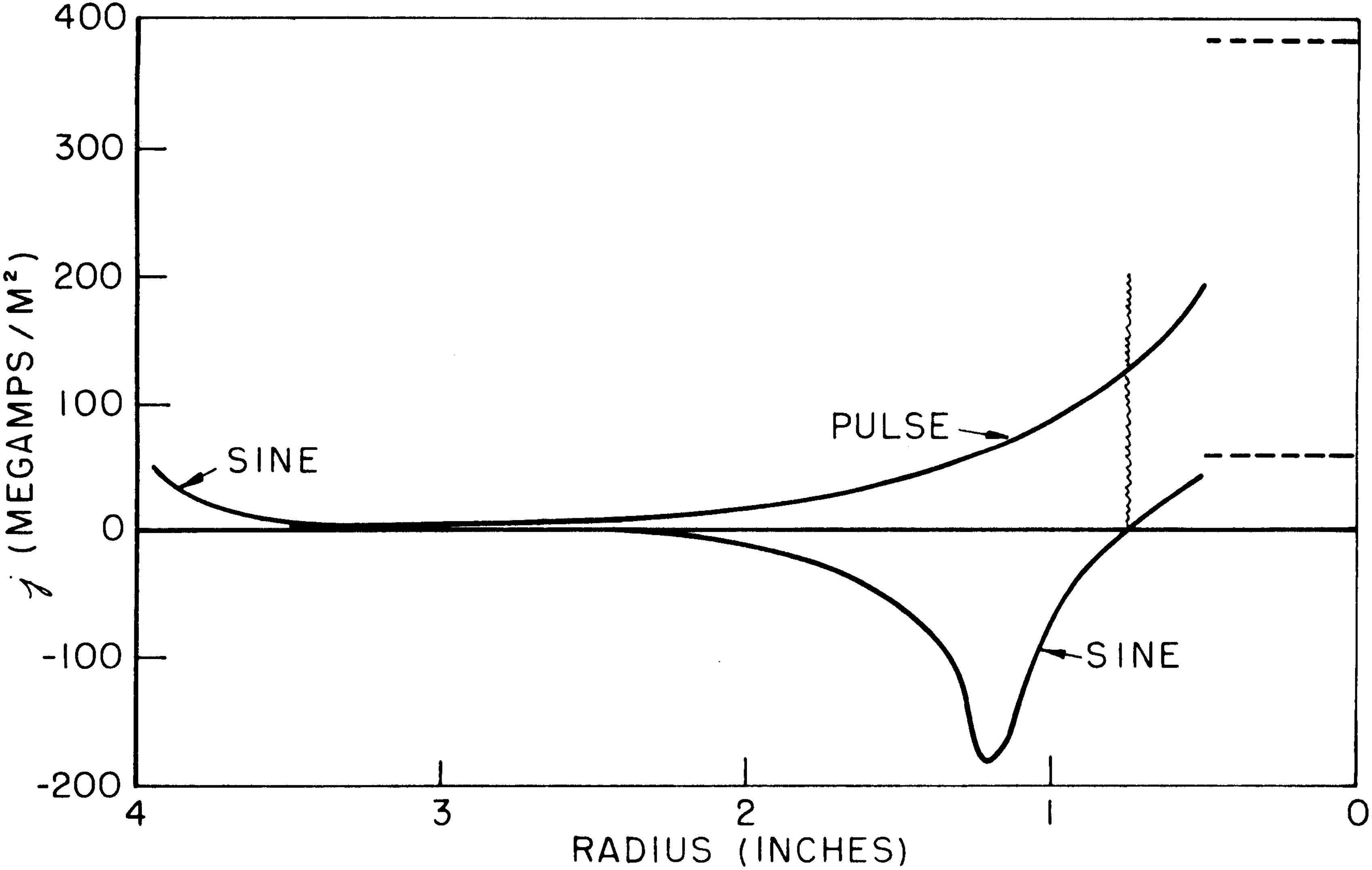

CURRENT DENSITY: 4.4 MICROSECONDS

FIGURE 5-5(h)

AP25-R 4101-66

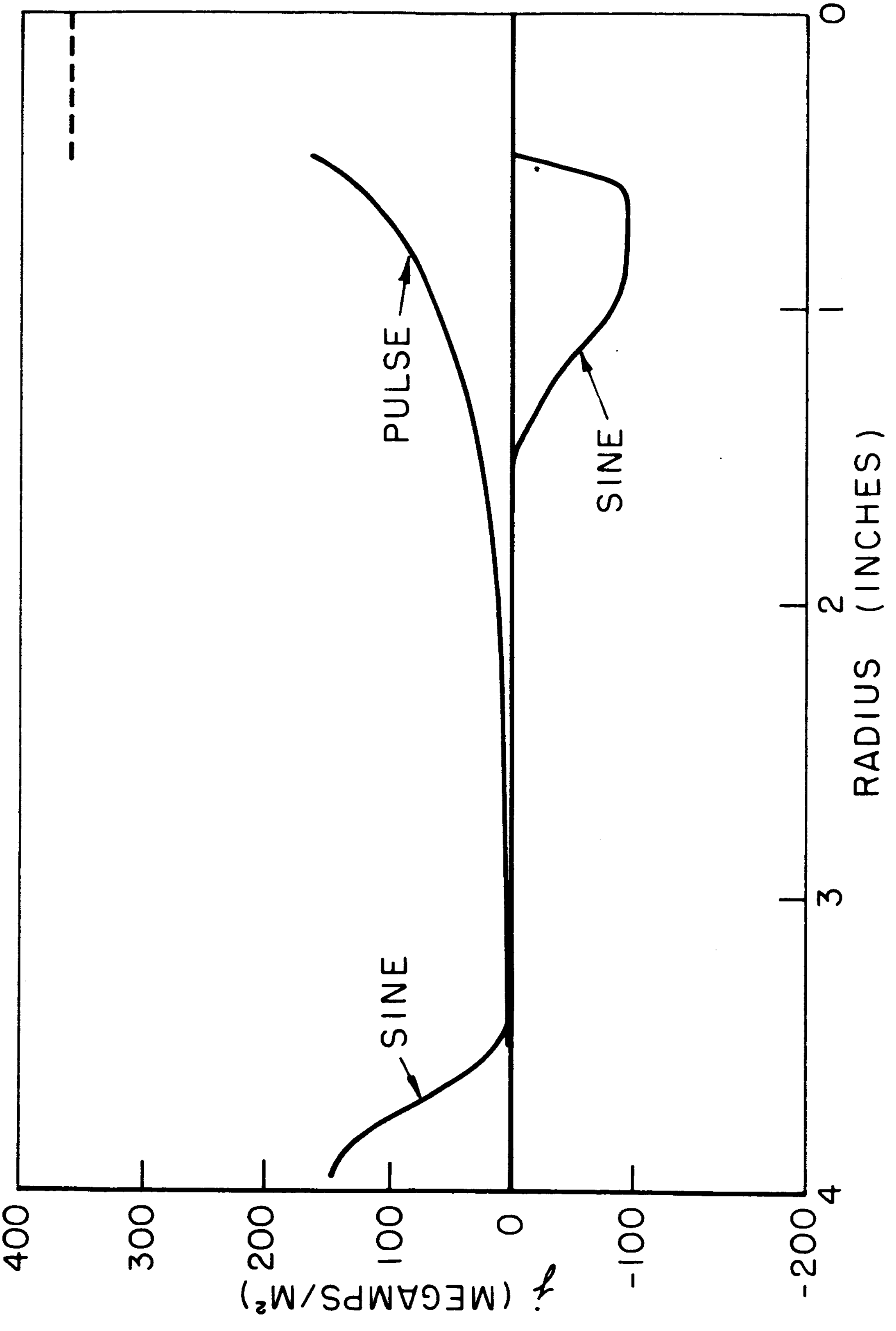

CURRENT DENSITY : 5 MICROSECONDS

FIGURE 5-5 (i)

AP25-R4/02-66

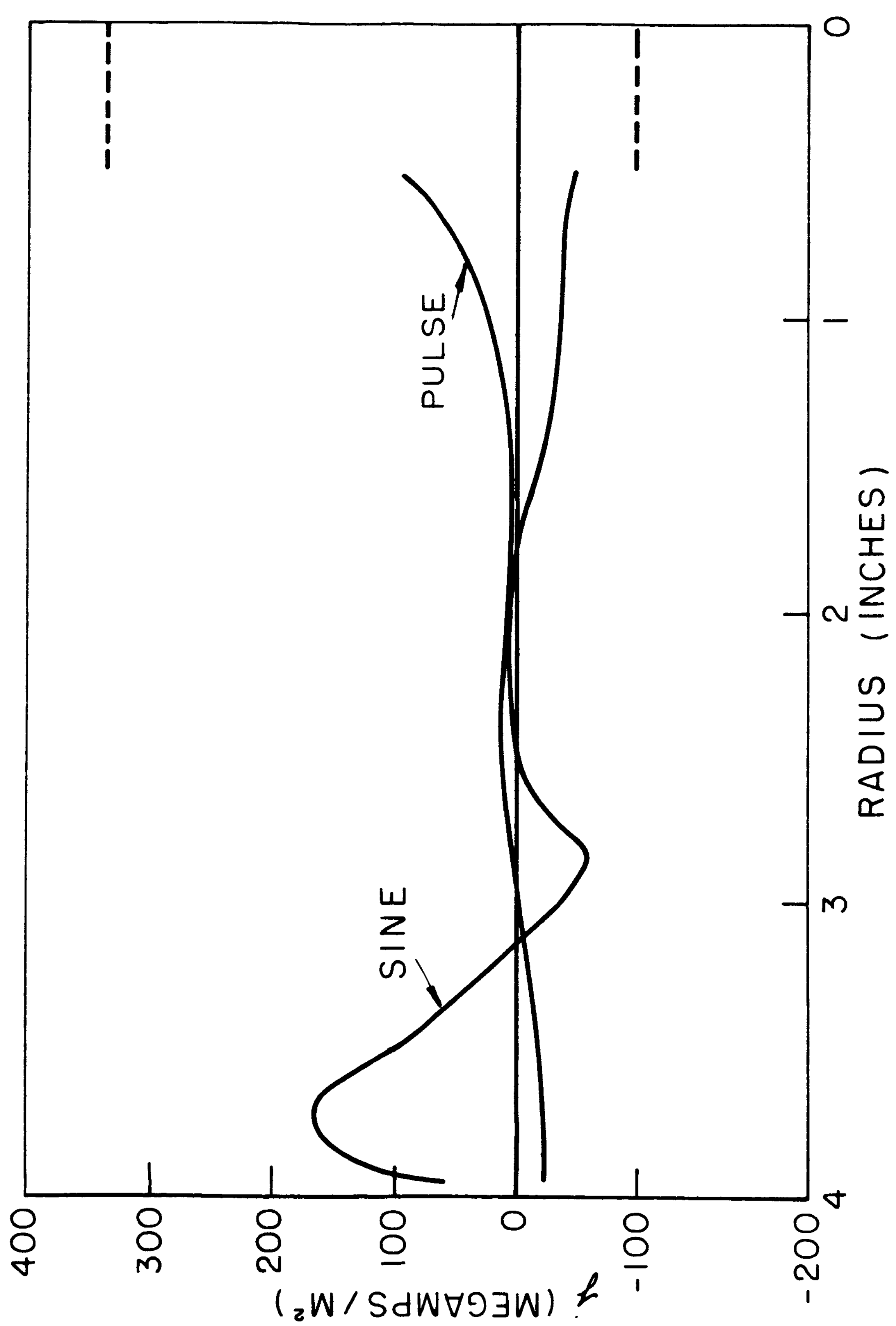

CURRENT DENSITY: 5.6 MICROSECONDS

FIGURE 5-5(j)

sheet formation and motion begins again, (h) - (j). Decoupling occurs for the first time in the pulse discharge as the pulse-driving current nears zero at 5.6 microseconds, (j), and negative current appears at the outer radius.

The positions of the luminous front at the times of current density plots, for the pulse-driven discharge, are also shown in Figs. 5-5(a-h). At early times the luminosity appears ahead of the maximum current density, subsequently it lags behind, but the trajectory of the luminous front is generally commensurate with that of the current sheet.

5.3 CURRENT SHEET BIFURCATION

In Fig. 5-5(f), two distinct maxima are evident in the (pulse) current density distribution. This bifurcation of the current sheet is clearly evident on the unintegrated ($\partial B/\partial t$) magnetic probe records. One such record is displayed in Fig. 5-6, taken with the probe 1.5" from the axis. The double-humped signal seen here can only be generated by two closely spaced propagating current sheets of like sign following each other into the center of the chamber. The bifurcation effect has only been observed at the 100 μ argon initial condition, with the (pulse) driving current waveform shown in Fig. 5-4.

5.4 DISCHARGE DYNAMICS

A variety of streak photographs and magnetic probe data make evident the dependence of the trajectories of the current

AP25-P50-66

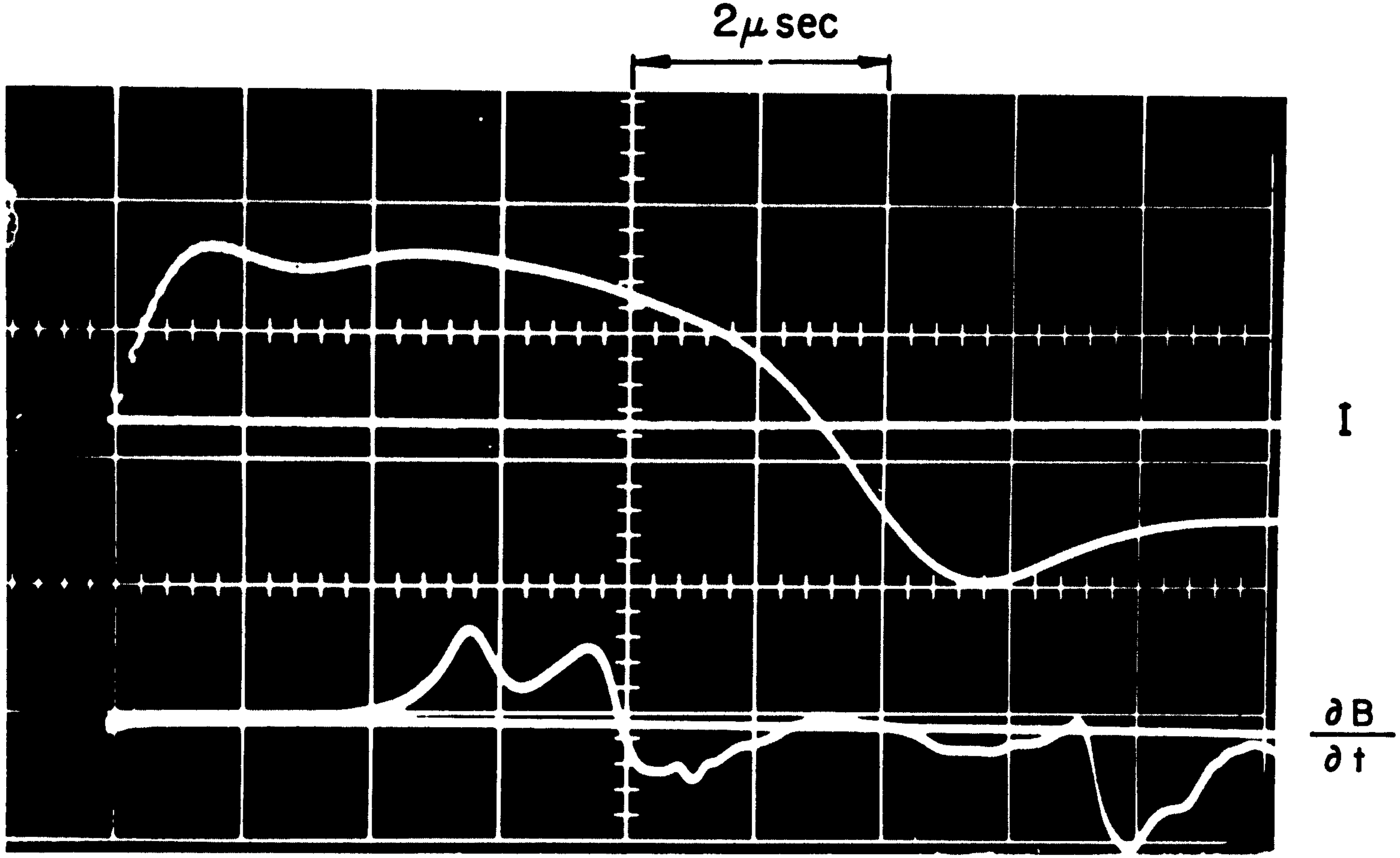

PINCH DISCHARGE CURRENT I AND PROBE RESPONSE
$\partial B/\partial t$, AT R = 1.5"

FIGURE 5-6

sheet and associated luminous front on the driving current and initial density. The more intense and sustained the driving current, the shorter the pinch time. Conversely, pinch time becomes longer when the initial density is increased. It is evident that the pinch phenomenon is dynamic in nature, driven by electrodynamic forces and restrained by momentum transfer. In the next chapter we show how the dynamic behavior of the discharge can be quantitatively correlated with the driving current and initial density by a model based on momentum conservation: the snowplow model.

CHAPTER VI

THE SNOWPLOW MODEL

6.1 THE MODEL

In 1954, Rosenbluth(15) proposed a simple physical model for the dynamics of the pinch effect. It has become widely known as the snowplow model. The thin current-sheet interface between the magnetic field and the undisturbed gas is presumed to act as an impermeable "magnetic piston" and in Rosenbluth's words: "We assume that all material which has been swept up by the magnetic piston is piled up in a very thin layer at the piston and travels with it."

If we had an actual material wall cylindrically collapsing, this piston would drive a cylindrical shock wave,(34)+ with a region of varying gas properties occurring between the piston and the shock front. The distance between the shock and piston is governed by the density ratio across the shock. For a strong shock in a real gas, where dissociation, excitation, and ionization become important internal energy "sinks," the ratio of specific heats, γ , approachs 1 and the density ratio can become quite large. Chu(36) has shown that the

---

+There is an extensive literature on cylindrical shock waves. Many commonly cited works are in the list of references in a 1961 University of Michigan technical report by Cole and Laporte.(35)

snowplow model is the zeroth order term in a power series expansion solution of the gasdynamic problem with the reciprocal of the density ratio as the expansion parameter.

The snowplow model is given a quantitative form by applying the principle of momentum conservation and thus equating the driving force of the magnetic-field current-sheet interaction to the time rate of change of momentum of the gas as it is swept up by the magnetic piston. Rosenbluth originally applied the model to the linear pinch; subsequently it was used for the θ-pinch, and coaxial gun accelerators.

6.2 THE LINEAR PINCH SNOWPLOW EQUATION

We consider a pinch discharge, depicted schematically in Fig. 6-1, in which we assume purely axial current flow, azimuthal symmetry, and the absence of axial gradients. We assume for the moment that the current is flowing axially in the region between r_1 and r_2. There is then only an azimuthal magnetic field whose amplitude is given by Ampere's law:

$$\frac{2\pi r B}{\mu_0} = I(r) \tag{6-1}$$

where $I(r)$ is the current flowing inside radius r. In the present situation with the total discharge current denoted by I:

$$\begin{aligned} I(r) &= I \qquad r \geqslant r_2 \\ I(r) &= 0 \qquad r \leqslant r_1 \end{aligned} \tag{6-2}$$

AD25-R4117-66

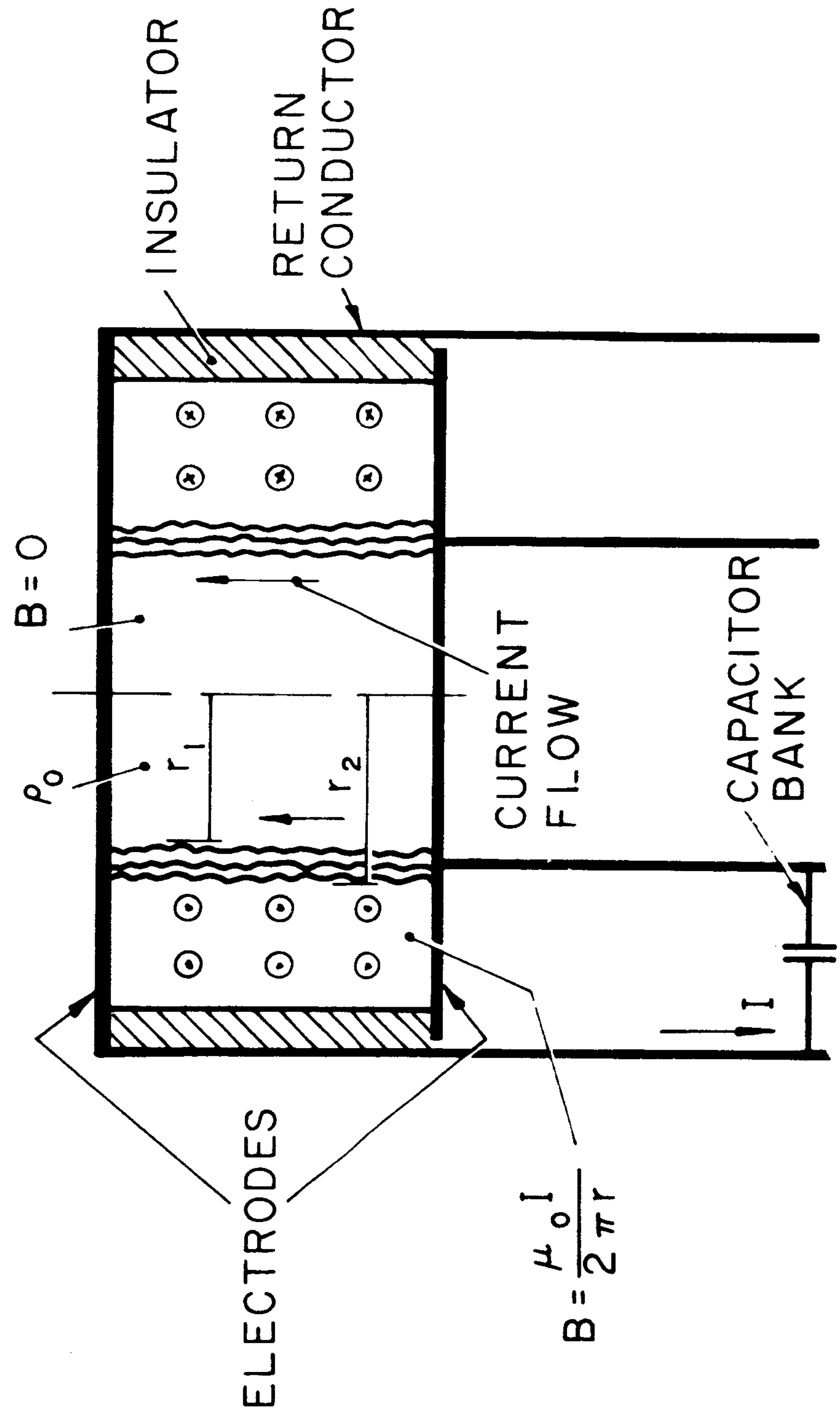

PINCH DISCHARGE

FIGURE 6-1

The local current density $\bar{j} = j\hat{e}_z$, where $\hat{e}_z$ is the axial unit vector, is given by Maxwell's equations, when displacement current is neglected:

$$\bar{j} = \frac{1}{\mu_0} \nabla \times \bar{B}$$

$$j = \frac{1}{\mu_0 r} \frac{\partial (B r)}{\partial r} \qquad (6\text{-}3)$$

In the region $r_1 \leq r \leq r_2$ there is a body force per unit volume:

$$\bar{F} = \bar{j} \times \bar{B} = -\frac{B}{\mu_0 r} \frac{\partial (B r)}{\partial r} \hat{e}_r \qquad (6\text{-}4)$$

and thus a net inward force per unit area of the cylindrical column

$$P = \int_{r_1}^{r_2} F_r \, dr = \frac{1}{\mu_0} \int_{r_1}^{r_2} \frac{B}{r} \frac{\partial (B r)}{\partial r} \, dr \qquad (6\text{-}5)$$

Now let us invoke the thin sheet assumption of the snowplow model; then the variation of r in the integral can be neglected and we have

$$P = \frac{1}{\mu_0} \int_{r_1}^{r_2} B \frac{\partial B}{\partial r} \, dr = \frac{1}{\mu_0} \left(\frac{B^2}{2} \right) \Bigg|_{r_1}^{r_2} \qquad (6\text{-}6)$$

From Eqs. (6-1) and (6-2) it follows that $B(r_1) = 0$, and thus

$$p = \frac{B^2}{2\mu_0} = \frac{\mu_0 I^2}{8\pi^2 r^2} \qquad \frac{\text{newtons}}{(\text{meter})^2} \qquad (6\text{-}7)^{+}$$

Equating the force to the time rate of change of momentum, per unit length, of the discharge column, we have:

$$2\pi r p = -\frac{d}{dt}\left(M \frac{dr}{dt}\right) \qquad (6\text{-}8)$$

where M is the mass per unit length that has been swept up by the inward moving sheath. With uniform initial mass density in the discharge chamber,

$$M = \pi(r_0^2 - r^2)\rho_0 \qquad (6\text{-}9)$$

Substituting Eqs. (6-7) into (6-6), we arrive at the snowplow equation for the linear pinch:

$$r \frac{d}{dt}\left[(r_0^2 - r^2)\frac{dr}{dt}\right] = \frac{-\mu_0 I^2}{4\pi^2 \rho_0} \qquad (6\text{-}10)$$

[+] The quantity p defined by (6-7), where B in general is the local magnetic field magnitude, with no special geometry presupposed, is commonly called the magnetic pressure, and is of special significance in the design of very high field magnets, inductive energy-storage assemblies, and megampere-current transmission assemblies. For p in atmospheres and B in kilogauss, one has the approximate relationship $p = (B/5)^2$.

The basic significance of the snowplow model to the pinch experiments of the fusion program lay in its prediction of a scaling law relating to the pinch time, i.e. the time required for the collapsing magnetic piston to (approximately) reach the axis, to such characteristics of the discharge as the initial density and the size of the apparatus. Rosenbluth initially formulated the problem in terms of the electric field applied across the discharge tube, the current then being a derived quantity coupled to the dynamics through the relation between current sheet radius and inductance of the discharge, and obtained, for the special case of constant electric field, a pinch time proportional to the one-fourth power of the initial density. Leontovich and Osovets(16) obtained the same dependence for the case of current linearly increasing in time. The latter case corresponded closely to experiments being performed with large capacitor banks, in which the pinch time occurred during the first quarter cycle of an inherently sinusoidal current so that the current was approximately linearly rising before the pinch. Agreement of the model with experiment was good; the one-fourth power dependence thus became an oft-quoted result, and acquired the status of a general law.(37) In a review article,(38) Cole pointed out "the critical role played by the current in determining the exact details of the plasma pinching," after showing that a parabolically rising ($I \sim t^{1/2}$) current, in the snowplow model, led to a one-third power dependence of pinch time on density. Goto,(39) et al. showed that the one-fourth power scaling relationship followed from dimensional analysis, without reference to the special assumptions of the snowplow model. In Appendix B we develop by dimensional analysis the consequences of assuming that the pinch process is describable by a small set of macroscopic parameters, and discuss special solutions and scaling laws obtained from a direct attack on the linear pinch snowplow equation.

6.3 COMPARISON OF OBSERVED AND CALCULATED TRAJECTORIES

In order to apply the snowplow model to our experimental situation, the actual discharge current for the particular capacitor configuration, as measured by the Rogowski coil, was used in evaluating the right hand side of Eq. (6-10). (The driving current is essentially unaffected by the dynamics of the discharge, because of the impedance mismatch between the network and the discharge.) Integration of the snowplow equation was accomplished with the aid of an IBM 1620 digital computer. A library differential equations subroutine performed the actual numerical integration using a predictor-corrector variable step-size technique. This subroutine is called by a Fortran program which takes as input the initial discharge radius, in inches, the molecular weight of the gas, and the initial gas pressure in microns. For each driving current waveform, a subroutine must be provided which delivers the instantaneous value of the driving current, in kiloamperes, as a function of the time in microseconds.

The effect of initial density on the snowplow trajectory is shown in Figs. 6-2 and 6-3 for two amplitudes of "constant" driving current. A solid curve defines the snowplow trajectories

AP25-4080-66

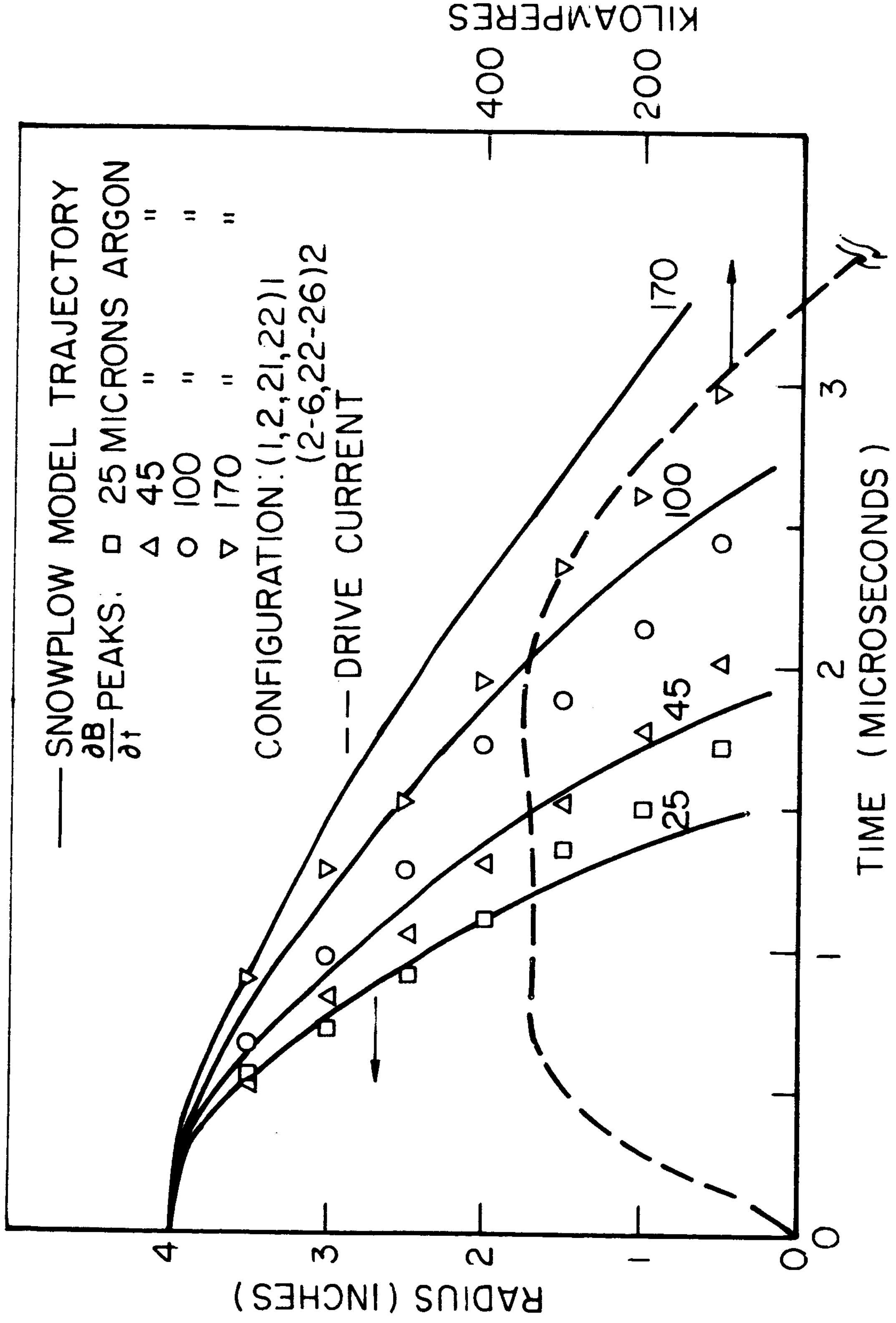

SNOWPLOW MODEL AND CURRENT-SHEET TRAJECTORIES

FIGURE 6-2

AP25-4081-66

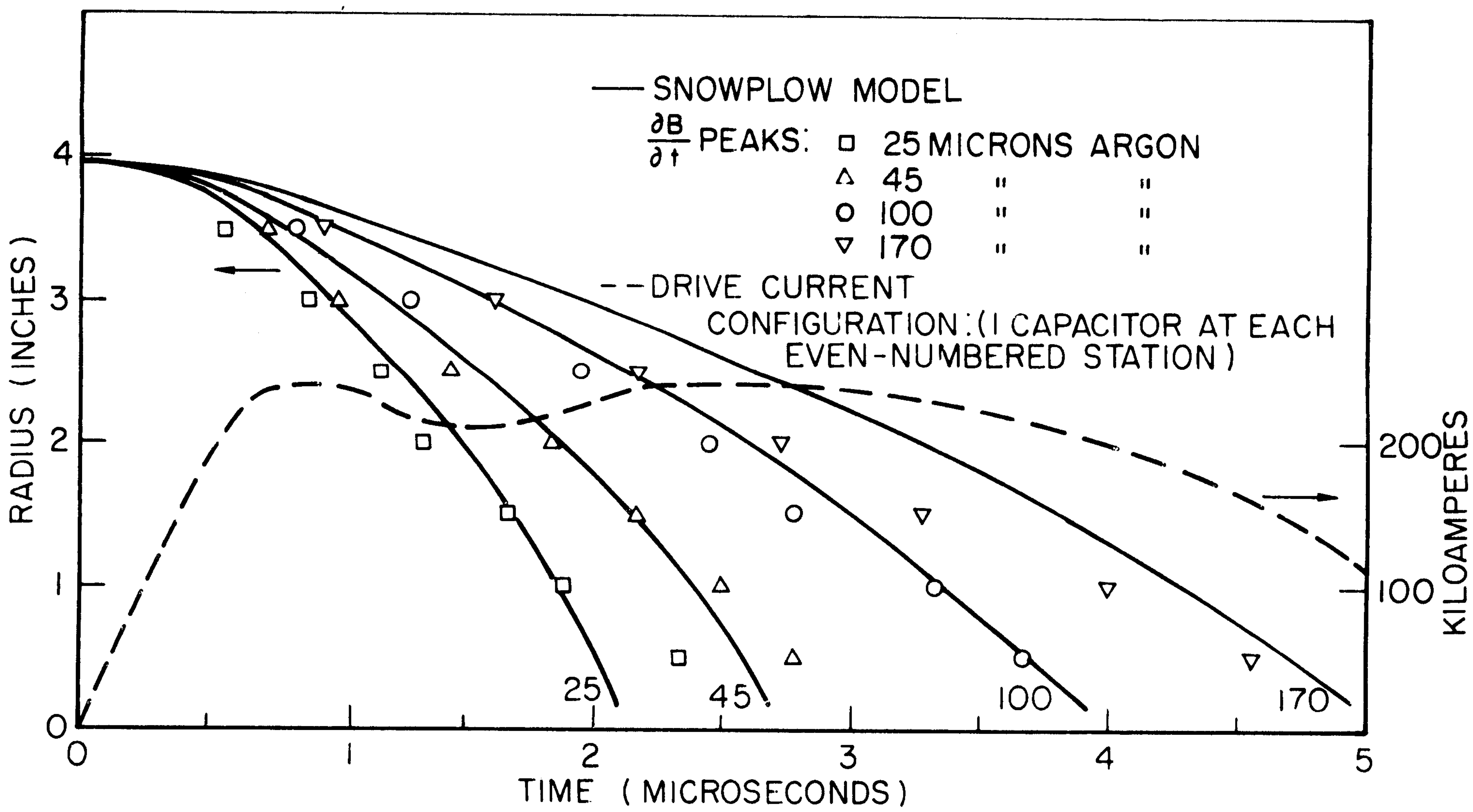

SNOWPLOW MODEL AND CURRENT-SHEET TRAJECTORIES

FIGURE 6-3

corresponding to initial (argon) pressures of 25, 45, 100, and 170 microns; a dashed line is used to display the driving current, which is plotted against the trajectory time axis.

These figures also illustrate the effect of two different current amplitudes on the trajectory for the same initial density. As one expects from the physical basis of the snowplow model, the velocity is greater for the larger driving current. However, while the two "constant current" waveforms differ principally in their amplitudes--about 340,000 and 230,000 amperes for Figs. 6-2 and 6-3 respectively--the non-negligible rise time invalidates the scaling relationship for constant driving current developed in Appendix B. The effect of the driving current is further exemplified by Figs. 6-4 and 6-5, which display the (100 μ) trajectories for two quite dissimilar current waveforms.

The broad range of densities and driving current waveforms involved in Figs. 6-2 - 6-5 constitute a severe test of the applicability of the snowplow model to the experimental situation described in Chapters IV and V. In Section (5-1) we made use of the unintegrated magnetic probe signal to indicate the amplitude and arrival time of the current sheet at a given radial position. From a series of records at several radial positions, for a given initial density and driving current, we can obtain the current sheet trajectory by plotting the time of the peaks against the probe-position radii. Data obtained in this fashion are superimposed on the theoretical trajectories of Figs. 6-2 - 6-5. It is seen that the snowplow

AP25-4079-66

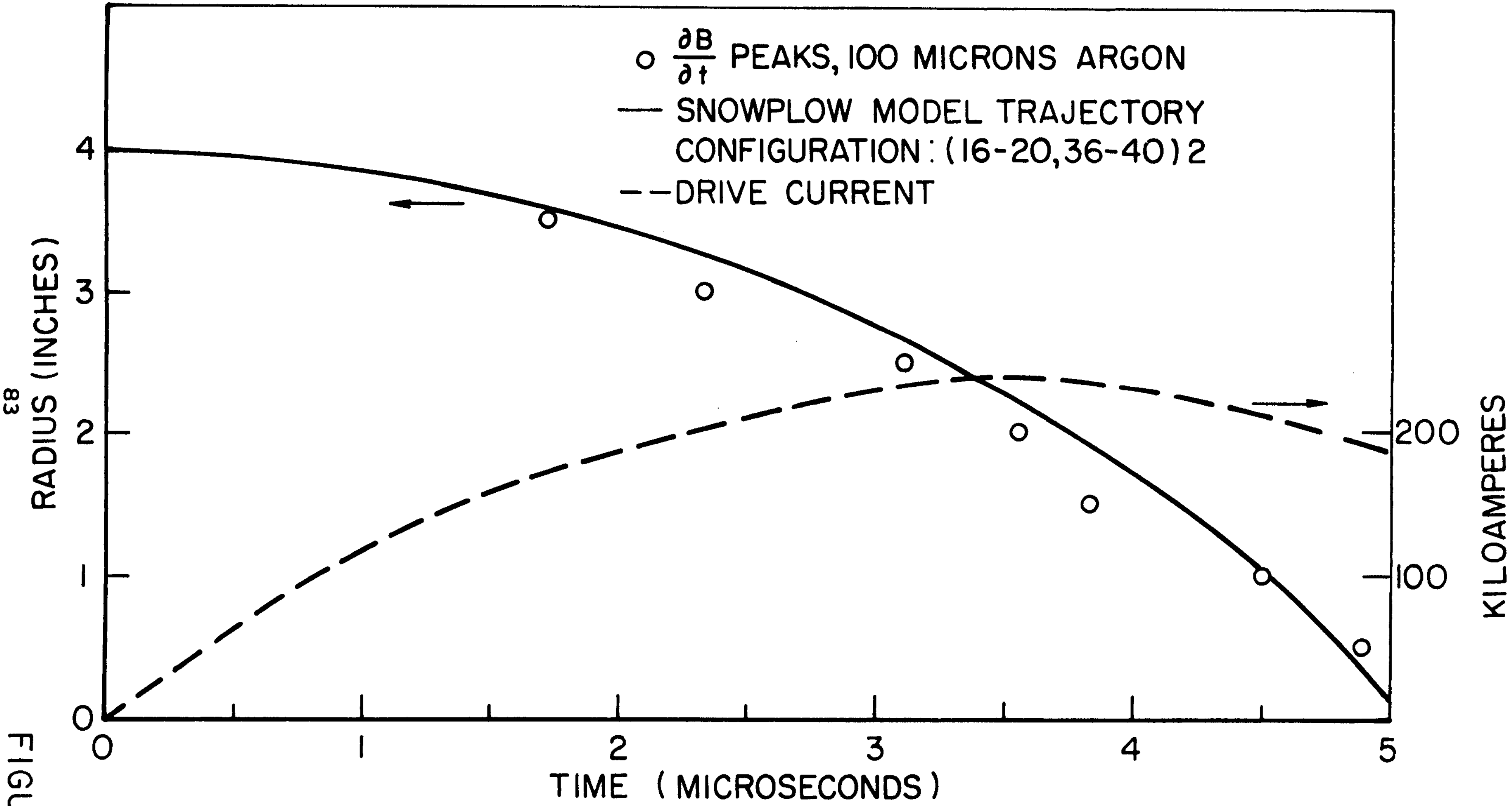

FIGURE 6-4

SNOWPLOW MODEL AND CURRENT-SHEET TRAJECTORIES

AP25-4078-66

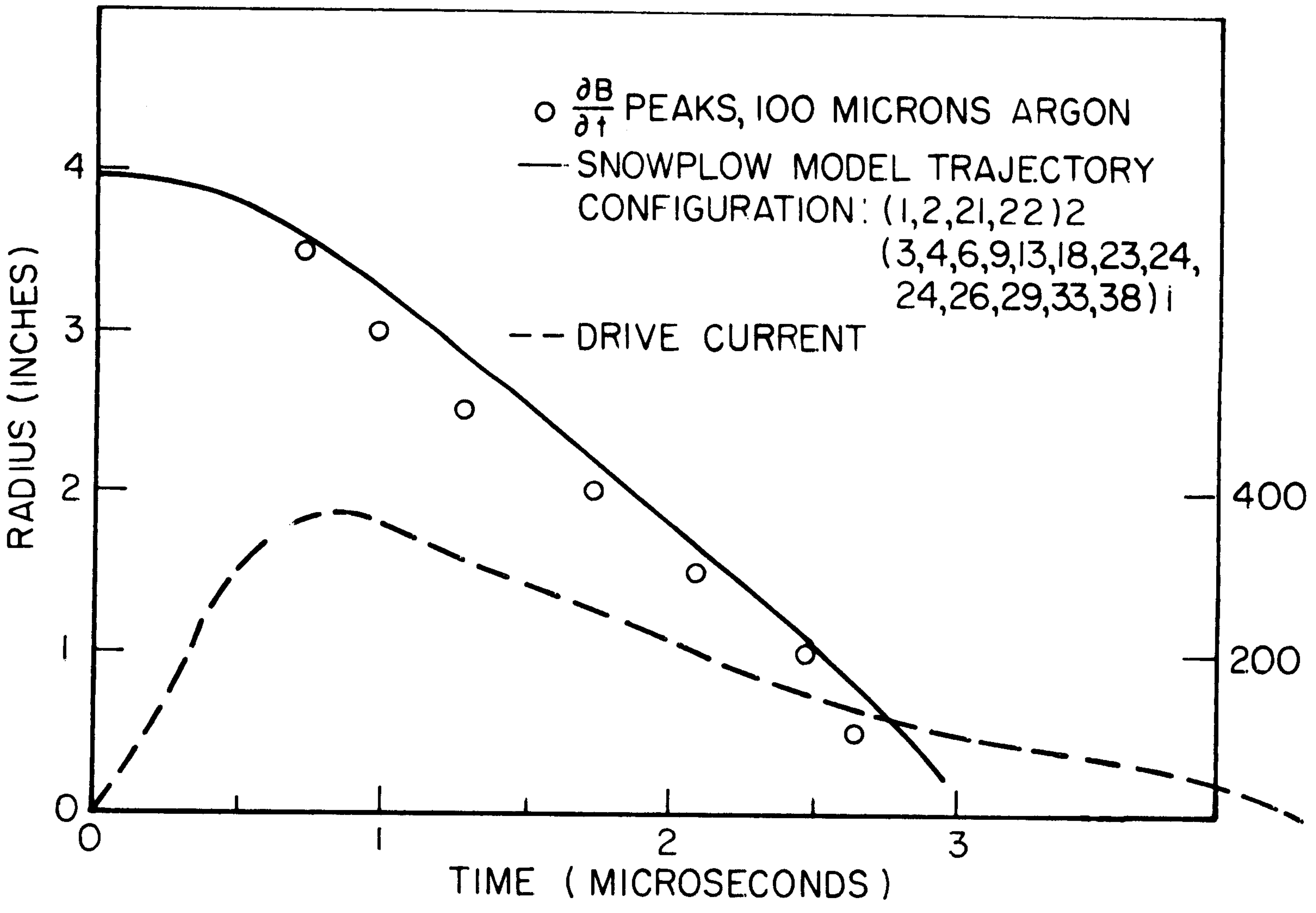

SNOWPLOW MODEL AND CURRENT-SHEET TRAJECTORIES

FIGURE 6-5

model indeed adequately predicts the behavior of this linear pinch discharge over a range of initial densities and diverse driving currents.

The demonstrated relevance of the simple snowplow representation justifies examination of certain other aspects of the dynamical behavior on this basis. For example, in Section (6-5), we investigate the dynamic efficiency of the acceleration process within this framework; some mathematical aspects of the snowplow equation, Eq. (6-10), are discussed in Appendix B.

6.4 TRAJECTORY BIFURCATION

The phenomenon of current sheet bifurcation, noted in Section (5-3), makes ambiguous the use of the peaks of the $(\partial B/\partial t)$ signals to define a unique current sheet trajectory. Snowplow model, luminosity front, and $(\partial B/\partial t)$ trajectories are plotted in Fig. 6-6, for the experimental situation in which bifurcation occurs. The luminous front trajectory was obtained from Kerr-cell synchronized streak photographs. A separate point is plotted for both $(\partial B/\partial t)$ peaks when bifurcation commences. Over the first half radius of travel, the (single) peaks follow the luminous front and snowplow trajectory quite closely. When bifurcation occurs, it is the second peak that continues to follow these trajectories; the first peak propagates ahead with greater velocity.

There are two clues to the significance of the fore-running pulse. First, its velocity appears to be just twice that of the

AP25-4099-66

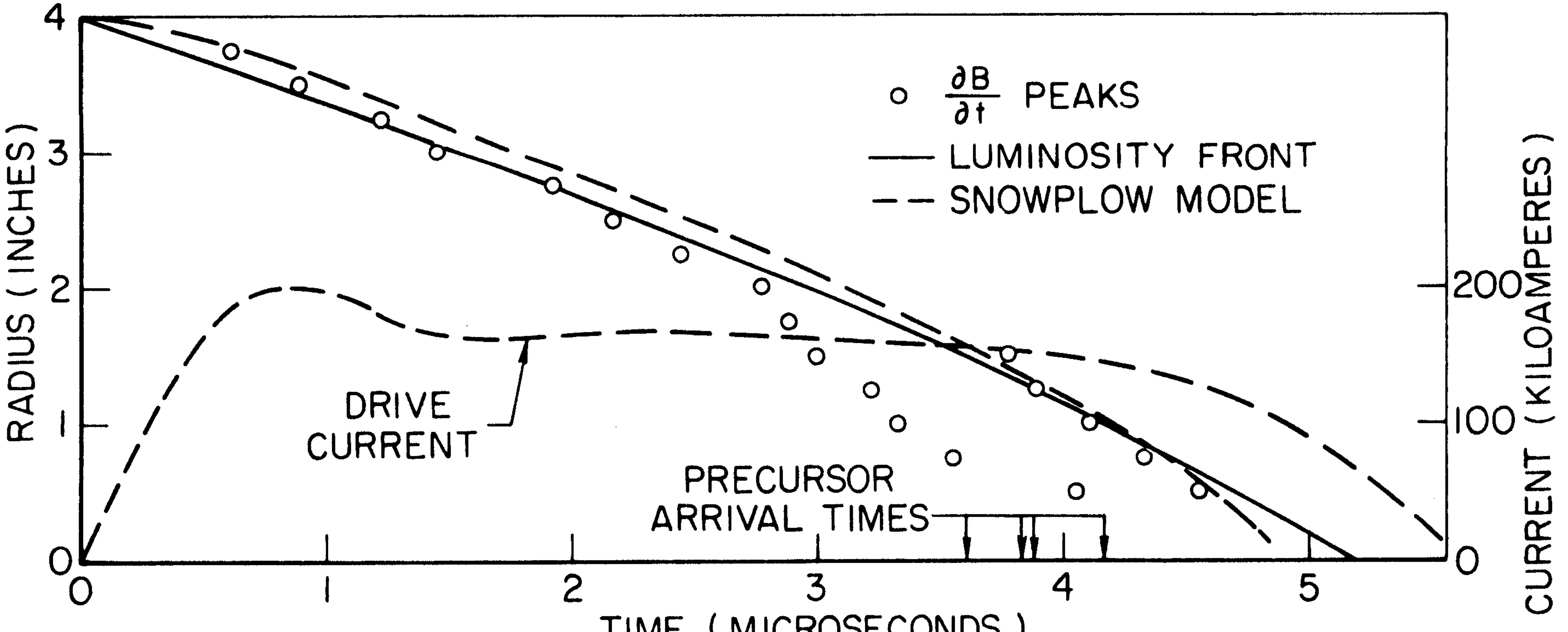

TRAJECTORIES OF: $\frac{\partial B}{\partial t}$ MAXIMA, LUMINOUS FRONT AND SNOWPLOW MODEL IN 8" PINCH DISCHARGE AT 100μ ARGON

FIGURE 6-6

main front. This brings to mind the "reflecting piston" alternative to the snowplow model, in which particles are assumed to elastically "bounce off" the magnetic piston and thus acquire twice the piston velocity. Second, precursor luminosity occasionally is seen to arise at the center of the chamber before the arrival of the main luminous front.(21) The time of occurrence of this precursor luminosity on the centerline of several streak photographs is also indicated in Fig. 6-6. These points are seen to be reasonable extrapolations of the fore-running $(\partial B/\partial t)$ peak. This correlation may be spurious, since we have observed such precursor luminosity, and even bifurcated luminosity fronts, in cases which show little indication of a bifurcated current distribution.

6.5 DYNAMICAL EFFICIENCY OF THE SNOWPLOW MODEL

It is well known that a strong shock propagating at constant velocity into a gas at rest converts about 50% of the available energy into organized streaming motion of the shocked gas and 50% into its internal, i.e., random thermal energy. The 50% figure has achieved a certain currency as representing the limiting efficiency of a pulsed plasma thrustor, since it has been contended that, in the range of shock strengths prevalent in useful pulsed plasma thrustors, the specific enthalpy of the shocked gas is so high that the bulk of its internal energy will be lost by radiation before it can be recovered by expansion at the orifice. There is, however, certain experimental evidence that the internal equilibration and radiation processes are not sufficiently rapid to dispose of the bulk of the internal energy on the time scale involved.(40) But, even conceding no recovery of internal energy for useful thrust work, the 50% criterion applies to the special gasdynamic situation of constant-velocity shock propagation into ambient gas at rest. Guman,(41) for example, has shown that a prior streaming motion of the ambient gas fill substantially alters the energy division for constant shock velocity.

Consider that the snowplow piston has accumulated mass m, is moving with velocity v, and is subject to the instantaneous driving force F. Then the equation of motion is:

$$\frac{d}{dt}(mv) = F \tag{6-11}$$

from which we can identify two components of the rate of energy deposition

$$vF = v\frac{d}{dt}(mv) = \frac{d}{dt}\left(\frac{1}{2}mv^2\right) + \frac{v^2}{2}\frac{dm}{dt} \tag{6-12}$$

The first term on the right is the rate of increase of streaming kinetic energy of the swept gas immediately useful for propulsion. The second term represents the dissipation associated with the inelastic collision of the incoming particles with the snowplow piston.

Imagine that the preceding process starts with some initial velocity v_0 and continues over a period of time t_f, at the end of which the piston has progressed a distance y_f and has accumulated a total mass m_f, which is now moving at a velocity v_f. We form the ratio of the integrals of the two terms of the right hand side of Eq. (6-12):

$$\alpha = \frac{\int_0^{t_f} \frac{v^2}{2} \frac{dm}{dt}\, dt}{1/2\, m_f v_f^2} \qquad (6\text{-}13)$$

which determines the dynamic efficiency of the process

$$\eta = \frac{1}{1+\alpha} \qquad (6\text{-}14)$$

At this point it might be noted that, in the very special case where the piston begins its motion with the total mass to be accelerated already entrained ("slug" model), dm/dt will be zero thereafter, and the efficiency η will be identically unity.

Returning to the general problem, we convert to dimensionless distance, velocity, mass, and time variables:

$$Y = y/y_f\,,\quad V = v/v_0\,,\quad M = m/m_f\,,\quad T = tv_0/y_f \qquad (6\text{-}15)$$

Note that our analysis is not restricted to the linear pinch snowplow equation, but is applicable to any one-dimensional accelerator, e.g. a coaxial gun with varying inter-electrode spacing. The geometry of a specific accelerator and the ambient gas density distribution are embodied in the functional dependence of accumulated mass on piston position

$$M = \mu(Y) \tag{6-16}$$

In terms of the dimensionless quantities, the energy-division ratio α becomes

$$\alpha = \frac{\int_0^{T_f} \left(\frac{dY}{dT}\right)^3 \frac{d\mu}{dY}\, dT}{\left(\frac{dY}{dT}\right)_f^2} = \frac{\int_0^1 V^2 \frac{d\mu}{dY}\, dY}{V_f^2} \tag{6-17}$$

In general, the development of the dimensionless velocity profile $V(Y)$ is determined by the magnitude and waveform of the discharge current as well as by the geometry and ambient gas distribution. However, it is instructive to examine the behavior of α for various assumed velocity profiles.

For example, a constant velocity accelerator has $V = 1$ throughout, then

$$\alpha = \int_0^{\mu_f} d\mu = 1 \tag{6-18}$$

and from Eq. (6-14) η = 50%. Note that this result is independent of accelerator geometry and initial gas distribution.

The effect of gas distribution and velocity profile on the efficiency is demonstrated by considering the two cases of the linear pinch and the simple, i.e. constant electrode spacing, coaxial gun, assuming a constant density initial gas fill, for the family of non-dimensional velocity profiles $V = e^{kY}$. For the linear pinch, on the one hand, the displacement of the piston is given by $y = r_o - r$, where r_o is the initial current sheet radius, and the corresponding dimensionless coordinate is $Y = (1 - r/r_o)$. The mass accumulation function is then $\mu(Y) = Y(2-Y)$ and $d\mu/dY = 2(1-Y)$ is seen to be a decreasing function of Y. On the other hand, for the simple coaxial gun, $\mu(Y) = Y$ and $d\mu/dY = 1$, independent of Y. By substituting the foregoing relationships into Eq. (6-17), we obtain the results of Table 6-1.

Table 6-1

Dynamic Efficiencies $V = e^{kY}$; Uniform Initial Density

k	α Coaxial Gun	α Linear Pinch	η Coaxial Gun	η Linear Pinch
0	1.00	1.00	0.50	0.50
1	0.43	0.300	0.70	0.770
2	0.25	0.110	0.80	0.900
3	0.17	0.050	0.85	0.950
10	0.05	0.005	0.95	0.995
∞	0.00	0.000	1.00	1.000

These calculations demonstrate explicitly that the dynamic efficiency of pulsed plasma accelerators does not have a general bound, but is determined by specific details of the piston velocity profile, channel geometry, and ambient gas distribution. In general, this efficiency is seen from our numerical examples, together with qualitative examination of Eq. (6-17), to be favored by vigorously accelerating velocity profiles, converging accelerator geometries, and decreasing ambient density profiles in the direction of propagation.

6.6 A GASDYNAMIC ARGUMENT

In this section we reconcile gasdynamics and the snowplow model by showing, for a simple gasdynamic situation, that an accelerating shock can convert more than 50% of the available energy to streaming kinetic energy.

Consider the situation of Fig. 6-7(a): a piston moving at constant speed V drives a shock at speed V_s into a gas at rest having pressure p_0 and density ρ_0, thus giving the gas speed V at pressure p and density ρ. For this situation, the continuity equation is

$$\rho(V_s - V) = \rho_0 V_s \tag{6-19a}$$

Assuming a strong shock, we neglect the pressure and internal energy of the unshocked gas, and thus obtain for the momentum

AP25-R4119-66

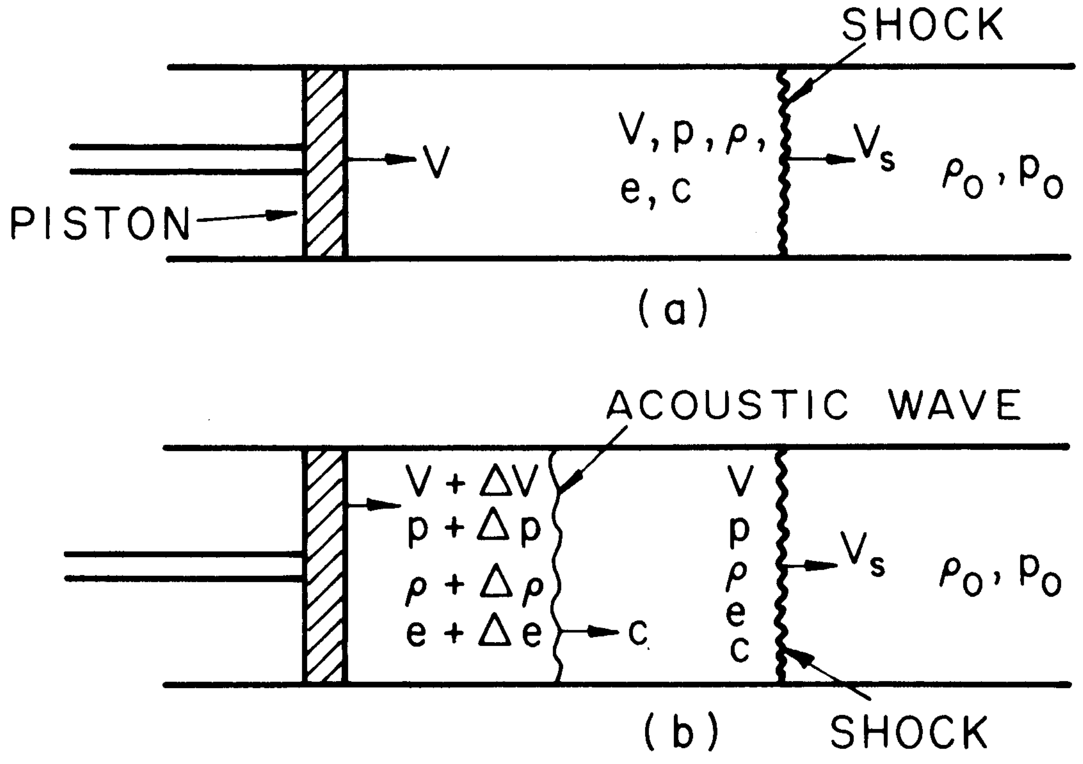

PISTON DRIVEN SHOCK WAVE

FIGURE 6-7

and energy equations

$$\rho(V_s - V)V = p \tag{6-19b}$$

$$\rho(V_s - V)(\tfrac{1}{2}V^2 + e) = pV \tag{6-19c}$$

where e is the internal energy of the shocked gas. By eliminating p from Eqs. (6-19b) and (6-19c) we find $e = 1/2 V^2$ i.e. the energy division is 50% internal and 50% kinetic.

Imagine now that the (massless) piston is suddenly given a small increase in velocity ΔV ; the changed state of affairs is communicated to the gas between the shock and the piston by a wave propagating at sonic speed c with respect to the shocked gas, Fig. 6-7(b). The gas between the piston and the wave has properties $V + \Delta V$, $p + \Delta p$, $\rho + \Delta \rho$, and $e + \Delta e$. Prior to the increase in velocity the piston was delivering power $W = pV$ to the system, the increase in power is accordingly given by

$$\Delta W = (p + \Delta p)(V + \Delta V) - pV = p\Delta V + V\Delta p \tag{6-20}$$

This additional power goes into additional kinetic energy at the rate

$$\Delta K.E. = \frac{1}{2}\rho c\left[(V + \Delta V)^2 - V^2\right] = \rho c V \Delta V \tag{6-21}$$

and into additional internal energy at the rate

$$\Delta E = \rho c \Delta e \tag{6-22}$$

We are interested in the ratio

$$\frac{\Delta (K.E.)}{\Delta E} = V\left(\frac{\Delta V}{\Delta e}\right) \tag{6-23}$$

From continuity across the wave

$$\rho c = (\rho + \Delta\rho)(c - \Delta v) \tag{6-24}$$

we have

$$\Delta V = \frac{c\,\Delta\rho}{\rho} \tag{6-25}$$

Now assume a perfect gas

$$de = 1/\gamma \; dh \tag{6-26a}$$

$$dh = de + d(p/\rho) \tag{6-26b}$$

thus

$$de = \frac{1}{\gamma - 1}\, d(p/\rho) \tag{6-27}$$

While for a weak (isentropic) wave

$$p/\rho^{\gamma} = \text{CONSTANT} \tag{6-28}$$

and we obtain

$$\Delta e = \frac{c^2}{\gamma\rho}\,\Delta\rho \tag{6-29}$$

Combining Eqs. (6-29) and (6-25), and substituting into (6-23), we have

$$\frac{\Delta K.E.}{\Delta E} = \frac{\gamma V}{c} \equiv \theta \tag{6-30}$$

We would like to know the conditions under which the energy division ratio $\theta = \gamma V/c$ is large. Now

$$\frac{V}{c} = \frac{V_s}{c} - M \tag{6-31}$$

where M is the Mach number with respect to the shock of the flow behind the strong shock. For a strong shock, M $\rightarrow \left(\frac{\gamma-1}{2\gamma}\right)^{1/2}$ We note that

$$\frac{V_s}{c} = \frac{M_s c_o}{c} = M_s \left(\frac{T_o}{T}\right)^{1/2} \tag{6-32}$$

where the subscript o denotes pre-shock conditions. The general expression for the free-stream temperature ratio is given by:(42)

$$\frac{T_o}{T} = \frac{\frac{(\gamma+1)^2}{2(\gamma-1)} M_s^2}{\left(1+\frac{\gamma-1}{2} M_s^2\right)\left(\frac{2\gamma}{\gamma-1} M_s^2 - 1\right)} \tag{6-33}$$

which for large M_s becomes

$$\frac{T_o}{T} = \frac{(\gamma+1)^2}{4\gamma\left(1+\frac{\gamma-1}{2} M_s^2\right)} \tag{6-34}$$

Thus from (6-32)

$$\frac{V_s}{c} = \frac{\gamma+1}{2\gamma^{1/2}} \frac{M_s}{\left(1+\frac{\gamma-1}{2} M_s^2\right)^{1/2}} \tag{6-35}$$

The worst case occurs when $(\gamma-1)M_s^2$ is large, then θ becomes

$$\theta = \frac{\gamma V}{c} = \frac{\gamma(\gamma+1)}{[2\gamma(\gamma-1)]^{1/2}} - \left(\frac{\gamma-1}{2\gamma}\right)^{1/2}$$

$$= \frac{\gamma^2+1}{[2\gamma(\gamma-1)]^{1/2}} \qquad (6\text{-}36)$$

which equals 2.53 for $\gamma = 5/3$. The energy division ratio is increasingly favorable as $(\gamma-1)M_s^2$ becomes of order unity.

The increase in efficiency achievable with accelerating pistons, in the snowplow and simple gasdynamic analyses, is a consequence of the fact that kinetic energy is not invariant under a Galilean transformation. In both cases a small increase in velocity represents a large increase in kinetic energy, with respect to the "laboratory" energy source coordinates.

CHAPTER VII

REVIEW AND RECOMMENDATIONS

The principal accomplishments of the research program described in the preceding chapters may be summarized as follows:

1. A versatile high-current pulse-forming network, which is capable of driving a low-impedance discharge having parameters applicable to pulsed plasma propulsion, has been constructed using relatively low grade commercial energy storage capacitors. In its present form, the mechanical assembly of this network is no more difficult than that of a conventional low-inductance capacitor bank.

2. The output current of this network can be accurately computed from a straightforward equivalent circuit representation.

3. Discharges driven by an (essentially) constant amplitude current pulse from the network exhibit several advantages over those powered by conventional capacitor banks: the secondary breakdown phenomenon is suppressed; the single current sheet remains coupled to the external circuit throughout its excursion, and thus maintains greater intensity as it undergoes sustained acceleration and achieves higher terminal velocity.

4. The dynamic behavior of these pulse-driven current sheets is adequately represented by a simple snowplow model.

5. Criteria for the dynamic efficiency of pulsed plasma accelerators have been developed on the basis of the snowplow formulation. In general this efficiency is found to be favored by vigorously accelerating velocity profiles, converging accelerator geometries, and decreasing ambient density profiles in the direction of propagation.

6. Under certain circumstances current sheets driven by the pulse-forming network are found to bifurcate midway in their excursion, yielding a substantial precursor current sheet having twice snowplow velocity.

As a logical extension of the program described above, it is recommended that the experimental conditions be extended to a regime where the impedance of the discharge and the pulse-forming network are more closely matched so as to manifest directly the essential electrodynamic coupling between the discharge dynamics and the current source. Under these conditions, a greater fraction of the initial stored energy will be transferred to the discharge before the circuit current reverses, and the current waveform will be seriously affected by the discharge dynamics. The discharge impedance results primarily from the change of inductance due to the current sheet motion, as discussed in Appendix C, and thus may be increased by increasing the velocity of the current sheet or the height of the discharge chamber. In the standard configuration used in the present experiments, the pulse-forming network impedance is about 50 milliohms, and the discharge impedance about 5 milliohms. Using the constant-current scaling relationship of Appendix B, which shows that the mean velocity is proportional to the current amplitude, one finds (for 10 KV charging voltage) that the network and discharge should be approximately matched for a network impedance of about 12 milliohms. The variational approach of Appendix A may be employed to determine the feasibility of achieving a respectable current waveform at this low line impedance. The requirements on the network could be eased by using a lower atomic weight gas, i.e. helium instead of argon, to obtain a lower initial mass density, and hence higher sheet velocity, while preserving the same particle number density.

The phenomenon of current sheet bifurcation, as noted in Chapter VI, may possibly be associated with elastic reflection of ambient ionized particles from the propagating magnetic piston. To pursue this effect further one might consider a sequence of experiments wherein the ambient gas would be pre-ionized to various levels by such means as an auxiliary discharge, ultraviolet irradiation, or radio-frequency excitation, and then attempt to correlate the precursor current sheet with the pre-ionization level.

APPENDIX A

TRANSMISSION LINES AND PULSE-FORMING NETWORKS

A.1 THE IDEAL UNIFORM TRANSMISSION LINE

We consider an ideal uniform transmission line, e.g. dissipationless coaxial cable, whose properties are specified by L' and C', the inductance per unit length and capacitance per unit length respectively. The voltage and current relationships for the line are:$^{(43)}$

$$\frac{\partial V}{\partial \ell} = -L' \frac{\partial I}{\partial t} \tag{A-1a}$$

$$\frac{\partial I}{\partial \ell} = -C' \frac{\partial V}{\partial t} \tag{A-1b}$$

where ℓ is the length coordinate.

We introduce a reference voltage, V_0, and a characteristic length, D. These serve to define a characteristic time

$$T_D \equiv (L'C')^{1/2} D \tag{A-2}$$

and current

$$I_0 \equiv V_0 (C'/L')^{1/2} \tag{A-3}$$

so we can establish the set of non-dimensional variables defined by

$$\begin{aligned} V &\equiv \phi V_0 \\ \ell &\equiv x D \\ I &\equiv j I_0 \\ t &\equiv \tau T_0 \end{aligned} \qquad \text{(A-4)}$$

Equations (A-1) then transform to

$$\frac{\partial \phi}{\partial x} = -\frac{\partial j}{\partial \tau} \qquad \text{(A-5a)}$$

$$\frac{\partial j}{\partial x} = -\frac{\partial \phi}{\partial \tau} \qquad \text{(A-5b)}$$

If we Laplace-transform equations (A-2), with respect to τ, and denote transformed quantities by a bar, we have

$$\frac{d\bar{\phi}}{dx} = -s\bar{j} + j(x,0) \qquad \text{(A-6a)}$$

$$\frac{d\bar{j}}{dx} = -s\bar{\phi} + \phi(x,0) \qquad \text{(A-6b)}$$

Our initial conditions are $V = V_0$ and $I = 0$, for all ℓ, at $t = 0$, therefore:

$$\frac{d\bar{\phi}}{dx} = -s\bar{j} \qquad \text{(A-7a)}$$

$$\frac{d\bar{j}}{dx} = -s\bar{\phi} + 1 \qquad \text{(A-7b)}$$

which yield the equations

$$\frac{d^2\bar{\phi}}{dx^2} = s^2\bar{\phi} - s \tag{A-8}$$

$$\frac{d^2\bar{j}}{dx^2} = s^2\bar{j} \tag{A-9}$$

having the general solutions

$$\bar{\phi} = A_1 e^{sx} + B_1 e^{-sx} + 1/s \tag{A-10}$$

$$\bar{j} = A_2 e^{sx} + B_2 e^{-sx} \tag{A-11}$$

where the A's and B's are constants.

For an infinite line, $A_1 = A_2 = 0$, and from Eqs. (A-7), (A-10), and (A-11) we find that $B_1 = B_2$. The solutions then become:

$$\bar{\phi} = B_1 e^{-sx} + 1/s \tag{A-12}$$

$$\bar{j} = B_1 e^{-sx} \tag{A-13}$$

Therefore:

$$\phi = j + 1 \tag{A-14}$$

and hence

$$V = I Z_L + V_0 \tag{A-15}$$

where $Z_L = (L'/C')^{1/2}$ is the characteristic impedance of the line.

At $\ell = 0$, we have the terminal properties of the line, $V_T = V$ and $I_T = -I$ since I_T is the current drawn from the line. It then follows from Eq. (A-15) that

$$V_T = V_0 - I_T Z_L \tag{A-16}$$

But this is just the equation for the voltage across the load in the simple circuit below:

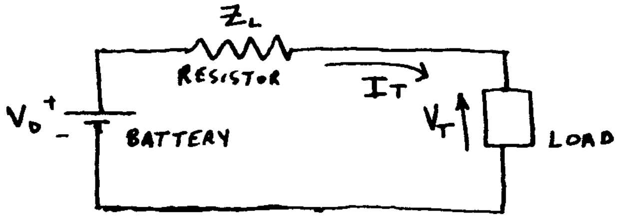

A finite-length line, switched across a load, must behave as an infinite length line for time less than the two-way transit time, since the initial disturbance must propagate to the open-circuit end, and a signal be sent back to the load, before any distinction can appear between the finite and infinite lines.

We can therefore state for time less than the two-way transit time: An ideal, uniform transmission line, having uniform initial charge, switched at $t = 0$ into an arbitrary impedance, has the terminal characteristics of an ideal battery, with output voltage equal to the line charging voltage, in series with a resistance equal to the characteristic impedance of the line.

Note that the impedance need not necessarily be linear, lumped, passive, or time-independent.

A.2 THE EQUI-SECTION NETWORK

A finite-length distributed line can be described in terms of its total capacitance and inductance, C and L respectively. The N-section lumped approximation to such a line is then

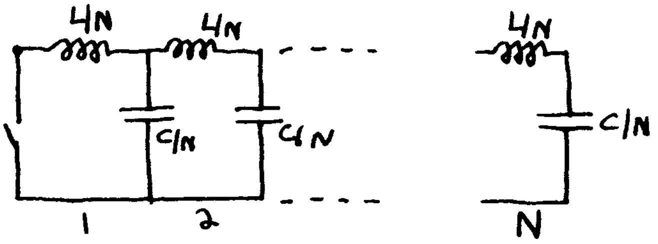

The short-circuit (first loop) current resulting from such a network (with capacitors initially charged to a uniform voltage) is displayed in Fig. A-1, for 3, 5, 10, and 20 sections, during the time the current is greater than zero. These curves were obtained by direct digital-computer integration of the coupled network circuit equations. The normalization is such that the ideal equivalent (distributed) line delivers unit current for twice the (one-way) unit-time. As one would expect, the greater the number of sections, the more nearly the network approximates the ideal response. However, the initial overshoot is almost exactly the same--about 9 percent--in all cases.

Unfortunately, as we pointed out in Section (4-3), the self-inductance of the capacitors is comparable with the

AP25-R4113-66

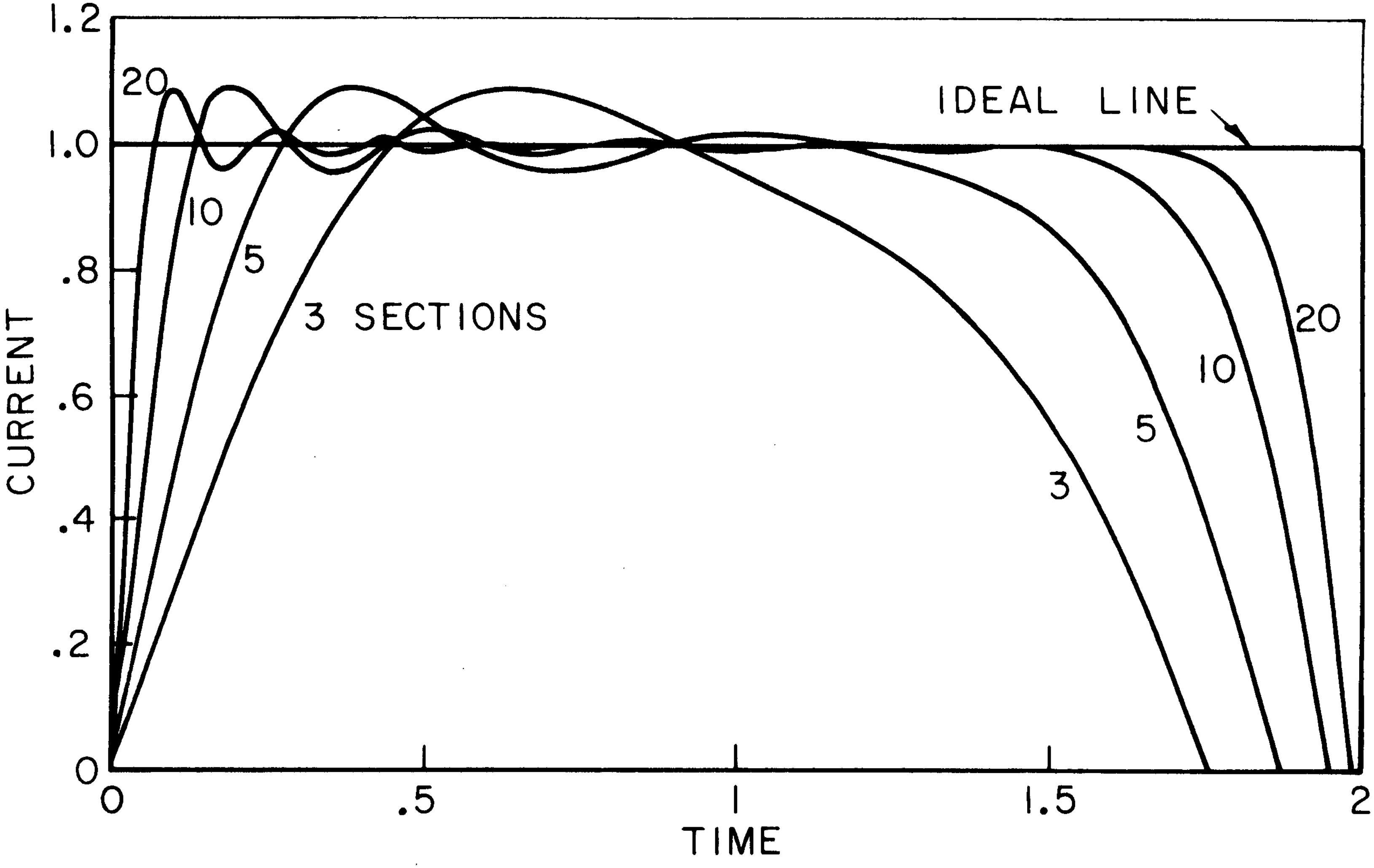

RESPONSE OF EQUI-SECTION NETWORKS

FIGURE A-1

network per-section inductance. The effect of capacitor self-inductance has been explored for a 10-section line having the circuit representation:

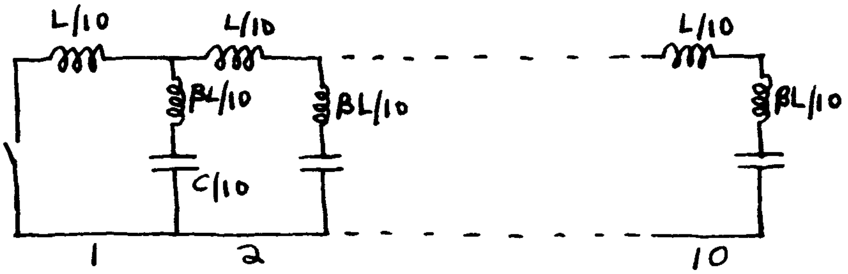

Short-circuit current for this network is shown in Fig. A-2, for several values of β , together with the normalized equivalent ideal line response. The waveform is systematically degraded, having increased rise-time and overshoot, by increasing β . Of course, in the limit of large β the effect of the line section inductances becomes negligible, and we effectively have a parallel connected capacitor bank.

The approximation of a uniform line by an equi-section network is limited by the realizable self-resonant frequency of the capacitors; the self-resonant frequency in turn is limited by technology, or cost, which increases sharply with self-resonant frequency. The one-section approximation to a line of total inductance L , and capacitance C , is:

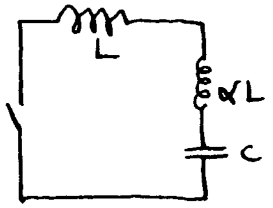

where α is the ratio of the self-inductance of the capacitor

AP25-RA115-66

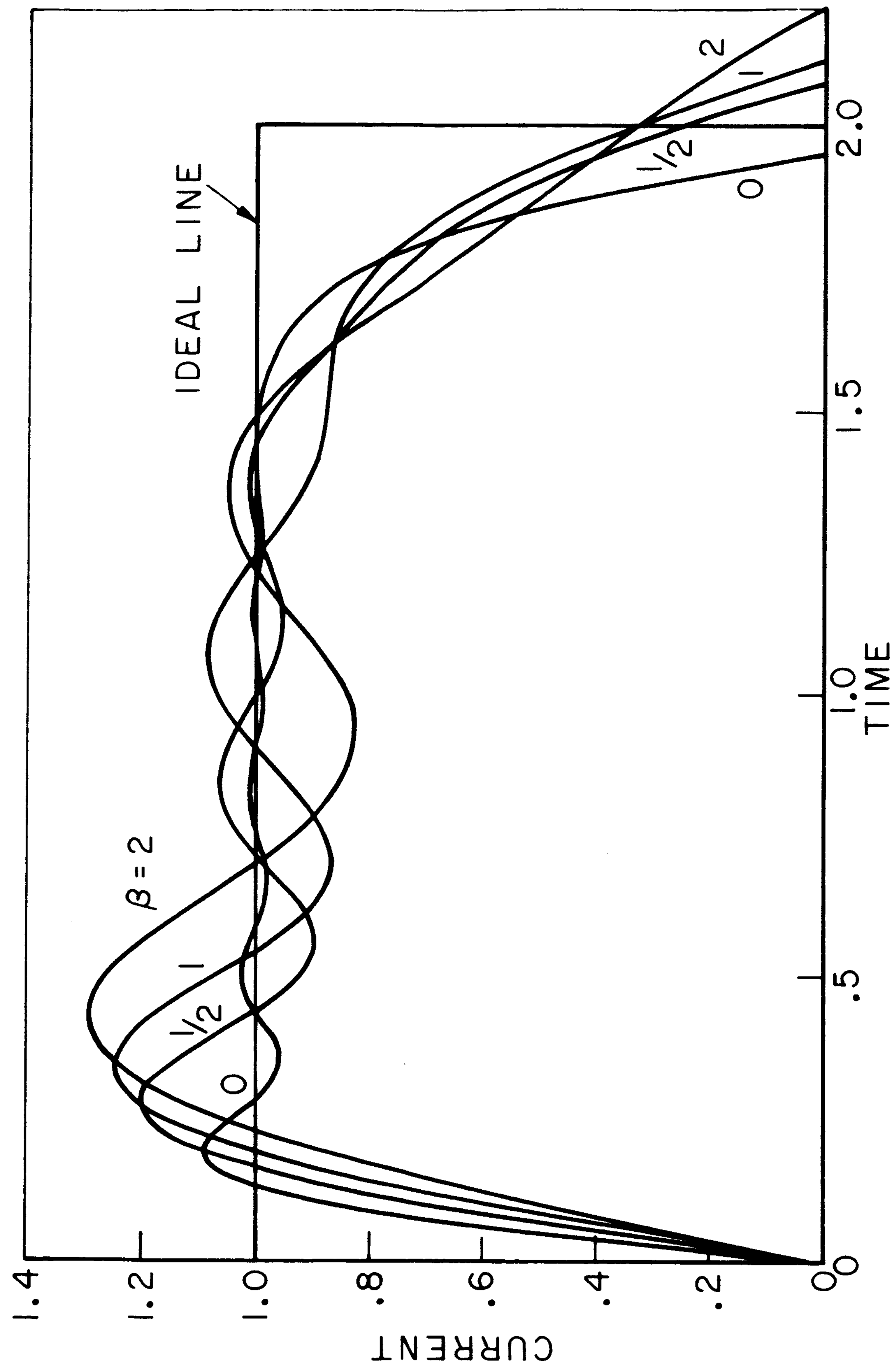

EFFECT OF PARASITIC INDUCTANCE, 10-SECTION NETWORK

FIGURE A-2

to the total line inductance. Thus the capacitor characteristic time is $\tau_C = (\alpha LC)^{1/2}$, and the line characteristic time is $\tau_L = (LC)^{1/2}$. Now the corresponding N-section network having the same total L and C is:

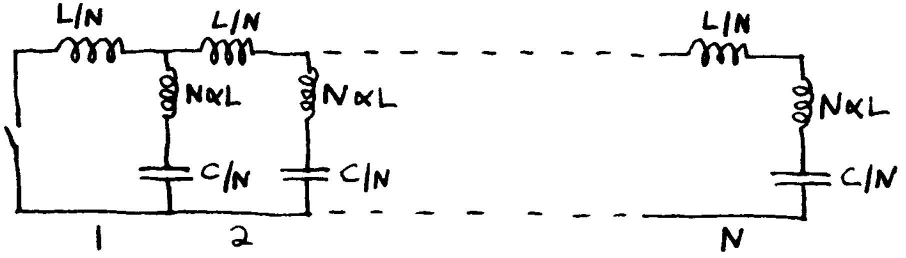

so that the characteristic time for each capacitor is $\tau_C = (N\alpha L \cdot C/N)^{1/2} = (\alpha LC)^{1/2}$, while the line characteristic time is also invariant, $\tau_L = N(L/N \cdot C/N)^{1/2} = (LC)^{1/2}$. So by holding α constant, and varying N, in the equivalent circuit above, we can explore the response of equi-section network having the same nominal characteristics L and C, constructed from capacitors of constant self-resonant frequency $f = [2\pi(\alpha LC)^{1/2}]^{-1}$, for a varying number of sections. Then the ratio of the capacitor self-inductance to the per-section inductance of the line becomes

$$\beta = \frac{N\alpha L}{L/N} = \alpha N^2 \tag{A-19}$$

On the one hand we expect from Fig. A-1 that the waveform is improved by increasing the number of sections, on the other hand increasing N means increasing β, from Eq. (A-19), and Fig. A-2 shows that the waveform is degraded by increasing β.

The resolution of these two opposing effects is shown in Fig. A-3. For capacitors of constant self-resonant frequency, the rise-time is improved by increasing the number of sections, but the overshoot is worsened.

It should be noted that the results displayed in Figs. A-1, -2, and -3 are all for a short-circuited network, and thus represent the worst case as far as the overshoot and oscillation about the nominal current are concerned. An inductive load component will damp the oscillation, though at the expense of increased rise time. A resistive load component will shorten the relative rise time--i.e. the time to reach a certain fraction of the nominal current--but not the absolute rate of current rise. With these considerations in mind, we can formulate the somewhat empirical proposition that useful performance will be obtained from a 10-section network with unit ratio of capacitor self-inductance to per-station inductance. The pulse waveform used for the current-density survey, Fig. 5-4, resulted from a configuration of the apparatus having some 24 nanohenries per-station, and 16 nanohenries per capacitor.

In Fig. A-3, the amplitude of the overshoot is seen to increase with the number, N , of network sections, but it is not reasonable that this trend continue without limit. The oscillations damp, even though the circuit contains no dissipative elements, but before they die out, the current is truncated at the characteristic time of the network. Additional insight into the questions of the natural amplitude

AP25-R4116-66

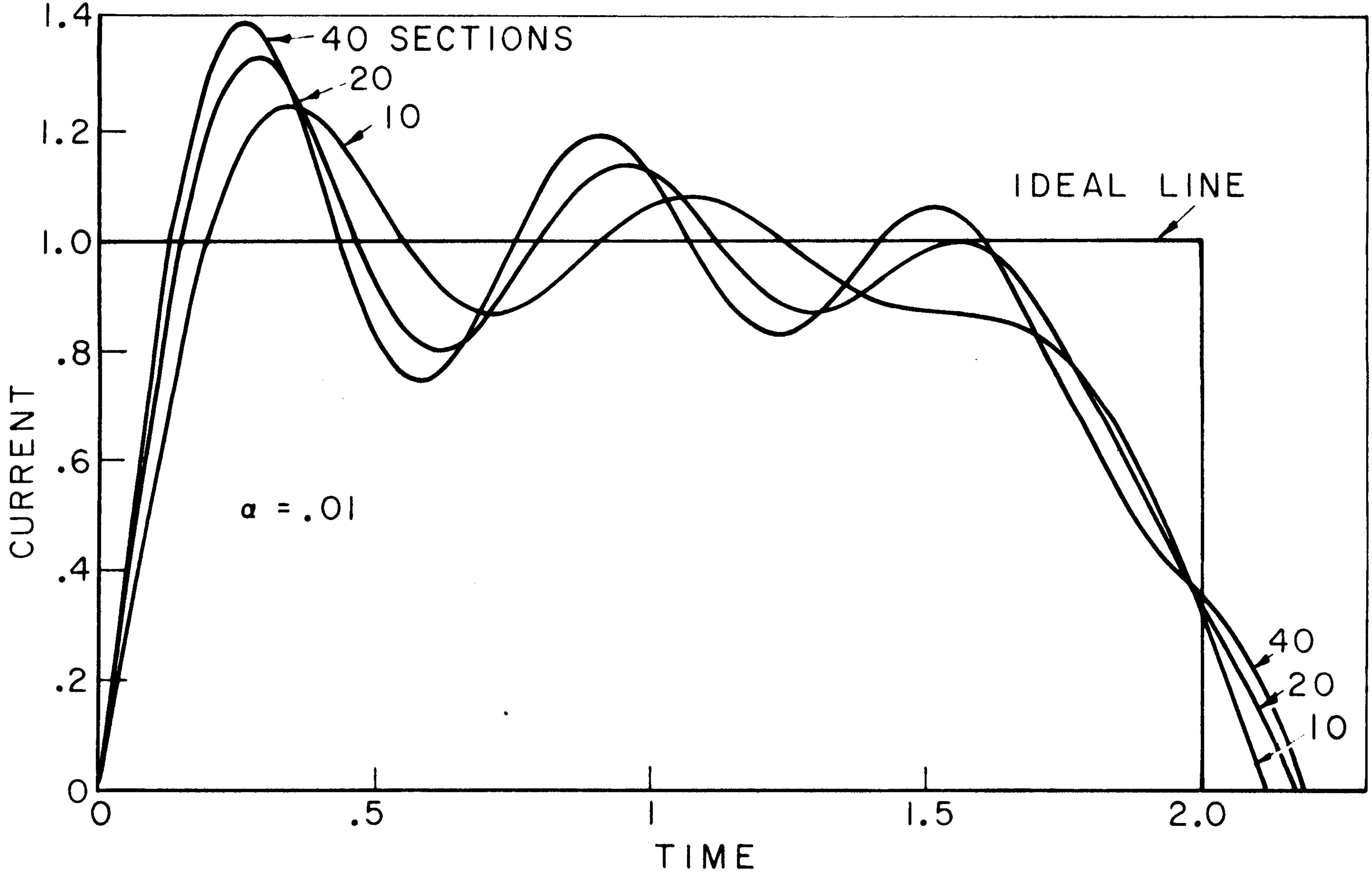

EFFECT OF NUMBER OF SECTIONS,
CONSTANT RESONANT FREQUENCY CAPACITORS

FIGURE A-3

and duration of these parasitic-inductance oscillations can be gleaned by considering the corresponding distributed line, which we take up in the next section.

A.3 THE DISTRIBUTED LINE WITH PARASITIC INDUCTANCE

We imagine a distributed uniform transmission line whose shunt admittance consists of a series inductance and capacitance. No attempt is made to visualize how such a structure could be physically realized. The line is characterized by L' and C', the inductance and capacitance per unit length, as in the normal case, and an additional parameter L^* having dimensions (inductance x length). The line equations are derived from considering the elemental line segment of length $d\ell$:

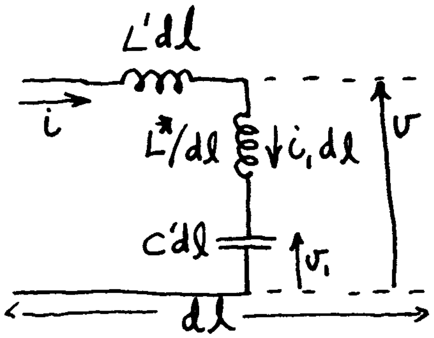

(A-20)

$$\frac{\partial v}{\partial \ell} = -L'\frac{\partial i}{\partial t}$$

$$\frac{\partial i}{\partial \ell} = -i_1$$

$$L^*\frac{\partial i_1}{\partial t} = v - v_1$$

$$C'\frac{\partial v_1}{\partial t} = i_1$$

If we now introduce the normalizing parameters

$$\begin{aligned} I_0 &\equiv V_0 (C'/L')^{1/2} \\ D_0 &\equiv (L^*/L')^{1/2} \\ T_0 &\equiv (L^*C')^{1/2} \end{aligned} \tag{A-21}$$

where V_0 is the charging voltage, and non-dimensionalize our variables by setting

$$\begin{aligned} l &= x D_0 \\ t &= \tau T_0 \\ i &= j I_0 \\ i_1 &= j_1 I_0 / D_0 \\ v &= \phi V_0 \\ v_1 &= \phi_1 V_0 \end{aligned} \tag{A-22}$$

the line equations become

$$\begin{aligned} \frac{\partial \phi}{\partial x} + \frac{\partial j}{\partial \tau} &= 0 \\ \frac{\partial j}{\partial x} + \frac{\partial \phi_1}{\partial \tau} &= 0 \\ \frac{\partial j}{\partial x} &= 0 \\ \frac{\partial j_1}{\partial \tau} &= \phi - \phi_1 \end{aligned} \tag{A-23}$$

We Laplace-transform with respect to τ, with initial conditions $j(x,0) = j_1(x,0) = 0$, $\phi(x,0) = \phi_1(x,0) = 1$, and eliminate $\bar{\phi}_1$ and $\bar{j}_1$, obtaining

$$(1+s^2)\bar{\phi}_{xx} = s^2\bar{\phi} - s \tag{A-24}$$

$$(1+s^2)\bar{j}_{xx} = s^2\bar{j} \tag{A-25}$$

where the bar denotes transformed variables.

These equations have the general solutions

$$\bar{\phi} = Ae^{\gamma x} + Be^{-\gamma x} + 1/s \tag{A-26}$$

$$\bar{j} = Ce^{\gamma x} + De^{-\gamma x} \tag{A-27}$$

with

$$\gamma = (s^2/s^2+1)^{1/2} \tag{A-28}$$

For an infinite line we must have $A=C=0$; to obtain the short-circuit response we have $\phi(x=0)=\bar{\phi}(x=0)=0$ so $B=-1/s$, and therefore

$$\bar{\phi} = \frac{1}{s}(1-e^{-\gamma x}) \tag{A-29}$$

$$\bar{j} = De^{-\gamma x} \tag{A-30}$$

But from the Laplace transform of the first of Eq. (A-23):

$$\bar{\phi}_x + s\bar{j} = 0 \tag{A-31}$$

Substituting Eq. (A-31) into Eqs. (A-29) and (A-30), we obtain

$$\bar{j} = -\frac{r}{s^2} e^{-rx} \tag{A-32}$$

We are interested in the short circuit current out of the line

$$j_T = -j(x=0)$$

$$\bar{j}_T = \frac{r}{s^2} = \frac{1}{s(s^2+1)^{1/2}} \tag{A-33}$$

The inversion yields(44)

$$j_T(\tau) = \int_0^\tau J_0(u)\,du \tag{A-34}$$

where J_0 is the zero-order Bessel function. This short-circuit current, I/I_0 is shown in Fig. A-4 as a function of $\tau = t/(L^*C')^{1/2}$. The oscillations damp slowly, even at τ = 33.8, a local maximum, the overshoot amplitude is nearly 14 percent.(45) It should be noted that the parasitic inductance parameter L^* controls only the time-scale of the phenomena, the amplitude of the overshoot is invariant, being a maximum of 47 percent at τ = 2.4.

AP25-RA120-66

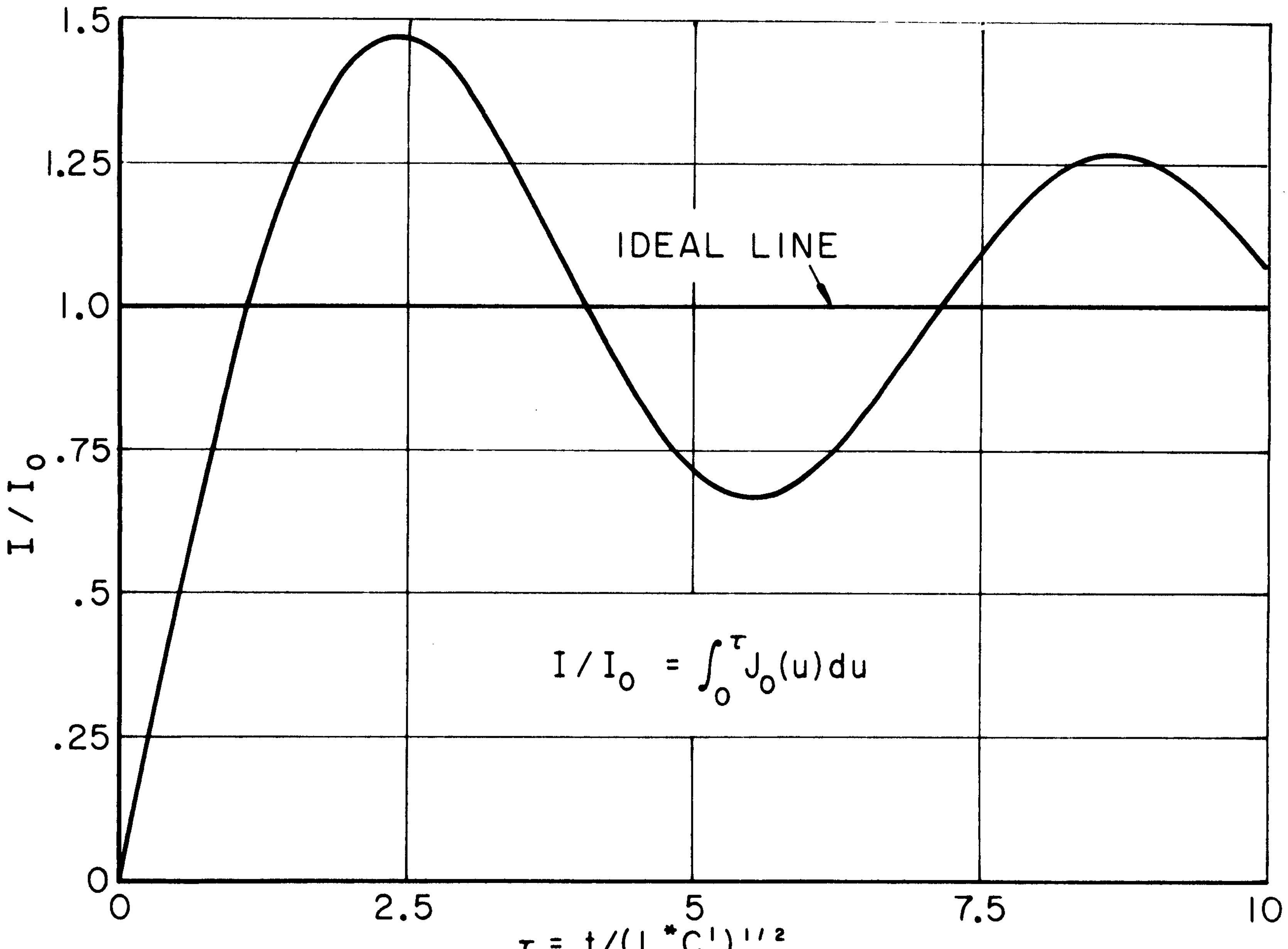

SHORT-CIRCUIT CURRENT FOR DISTRIBUTED LINE WITH PARASITIC INDUCTANCE

FIGURE A-4

The trends shown in Fig. A-3, and discussed in the last paragraph of Section (A-2), can now be interpreted in light of the above results.

The network for Fig. A-3 had N -sections of shunt capacitance C/N , shunt inductance αNL , and series inductance L/N ; the time scale for Fig. A-3 is in units of the network characteristic time $N(LC/N^2)^{1/2} = (LC)^{1/2}$ However, the parasitic inductance time-scale, corresponding to τ in the distributed line analysis, is in units of $(\alpha NL \times C/N)^{1/2} = \alpha^{1/2}(LC)^{1/2}$. In the numerical example considered, α =.01. Thus time of maximum (47 percent) overshoot, τ = 2.4, for the distributed parasitic line, corresponds to 0.1 x 2.4 = .24 on the time-scale of Fig. 3, while the 40-section network is seen to approach this distributed-line maximum, having its maximum overshoot of 39.5 percent at time = .26.

A.4 A VARIATIONAL APPROACH[+]

While we have confined our analytical discussion to the equi-section network as a means of generating a rectangular current waveform, there remains the larger question of obtaining an arbitrary waveform, or an improved approximation to the rectangular waveform, from a more general network configuration. However we wish to impose certain constraints

---

[+] We are indebted to Professor L. E. McBride, Jr., of the Department of Electrical Engineering at Princeton, New Jersey, for suggesting this method.

of an engineering nature which invalidate the usual techniques of circuit synthesis: high voltage energy-storage capacitors are expensive and reasonably procurable only in batches of units having the same nominal capacitance, instead of a continuum of values; further, real capacitors have self-inductance which cannot be ignored in the low-impedance regime. Because of the relative ease of realizing low-inductances, it is desirable to retain the parallel-plate ladder network construction. A variational approach lets us optimize the inductance under the constraint of fixed capacitor values.

The coupled circuit equations can be cast into the form a set of simultaneous first-order constant-coefficient O.D.E.'s, in matrix notation:

$$\dot{X} = AX \tag{A-35}$$

where the individual loop currents and capacitor charges are an appropriate set of dependent variables. Now suppose we establish some error measure, $\mathcal{J}$, which expresses the deviation of the actual current waveform from that desired, and thus is a function of the load current, which we can take to be X_1 , taking the form:

$$\mathcal{J} = \int_0^t f[X_1(\tau)]\,d\tau \tag{A-36}$$

We seek to minimize $\mathcal{J}$ over some interval, by varying certain of the series inductance elements, L_i of the ladder network. Now

$$\frac{\partial J}{\partial L_i} = \int_0^t \frac{\partial f}{\partial x_1}\frac{\partial x_1}{\partial L_i}\, dt \tag{A-37}$$

Define a set of vectors $z_i = \partial X/\partial L_i$, then

$$\frac{\partial \dot{x}}{\partial L_i} = \dot{z}_i = \frac{\partial A}{\partial L_i} X + A z_i \tag{A-38}$$

using Eq. (A-35). Equation (A-38) shows how the vectors z_i can be carried along in time (by numerical integration) simultaneously with , and thus the first element of z_i, $\frac{\partial x}{\partial L_i}$, can be extracted for the computation of $\partial J/\partial L_i$ through Eq. (A-37). The gradients $\partial J/\partial L_i$, at the end of the desired pulse time, indicate how to change the inductances L_i to reduce J in a successive iteration.

One point was glossed over in introducing the circuit equations in the form of Eq. (A-35). The circuit equations actually present themselves in the form $B\dot{X} = CX$. Thus $A = B^{-1}C$. It is impractical to express A analytically in terms of the elements of the known matrices B and C, but we need to obtain $\partial A/\partial L_i$ from B and C.

One step is gained by noting that

$$\frac{\partial A}{\partial L_i} = \frac{\partial (B^{-1}C)}{\partial L_i} = B^{-1}\frac{\partial C}{\partial L_i} + \frac{\partial B^{-1}}{\partial L_i}C \tag{A-39}$$

The matrix $(\partial C/\partial L_i)$ is available, since we initially have C in analytic form. Furthermore

$$\frac{\partial (BB^{-1})}{\partial L_i} = \frac{\partial I}{\partial L_i} = 0 = \frac{\partial B}{\partial L_i}B^{-1} + B\frac{\partial B^{-1}}{\partial L_i} \tag{A-40}$$

where I is the unit matrix. Therefore

$$\frac{\partial B^{-1}}{\partial L_i} = -B^{-1}\frac{\partial B}{\partial L_i}B^{-1} \tag{A-41}$$

so $(\partial A/\partial L_i)$ can be obtained from the known matrices B and C.

Despite the relatively straightforward formulation of the variational method, a considerable amount of computation may be involved.

For an N-section network, X is a vector of rank 2N (N loop currents and N capacitor charges). If the L_i are to be all N series inductances:

we must store

2(N+1) N-th order matrices B, C, $\partial B/\partial L_i$, $\partial C/\partial L_i$

and integrate

2N first order O.D.E.'s $\dot{X} = AX$

2N(N) first order O.D.E.'s $\dot{z}_i = (\partial A/\partial L_i)X + Az_i$

or 2N(N+1) equations in all, i.e. 220 equations for a 10-section network.

APPENDIX B

SNOWPLOW MATHEMATICS

B.1 DIMENSIONAL ANALYSIS(46,47)

A great arsenal of mathematical techniques, supplemented in recent years by powerful computational engines, is available to hammer quantitative results from equations that describe a physical problem. But the crucial step is often the formulation of an adequate set of equations; there is always some degree of approximation inherent in any mathematical description of the physical world. To many, dimensional analysis is somewhat mystical since it produces results--in textbook examples--seemingly without recourse to any equations. But the selection of a set of parameters in terms of which it is supposed that the phenomena can be described is also the first step in formulating a set of equations. In Langhaar's words (Ref. 47, p. v): "The application of dimensional analysis to any particular phenomenon is based on the assumption that certain variables, which are named, are the independent variables of the problem, and that all variables, other than these and the dependent variable, are redundant or irrelevant. This initial step--the naming of the variables--often requires a philosophic insight into natural phenomena." Now a high-current plasma discharge, which can reasonably be expected to involve elements of fluid mechanics, electrodynamics, and charged-particle collisions, has a large number of not obviously irrelevant variables: Pai(48) lists twenty-two of them.

We follow the trail blazed by Rosenbluth in formulating the snowplow model, and assume that a very limited set of parameters determine the time-to-pinch, t_p, of a high-current transient discharge, namely:

the size, expressed by the initial radius of the discharge, R ;

the initial mass density, ρ_0 ;

the discharge current, $I(t)$;

the MKSQ dimensional constant, μ_0 .

The last of these is clearly not an experimental <u>variable</u>, but enters the analysis as a "dimensional constant" necessary to account for the coupling between currents and forces; the matter of dimensional constants is discussed in Chapter V of Bridgman's book.(46)

We now assume the current to be of the form $I = At^n$; note that this includes the interesting case of constant current for $n = 0$. The dimensional matrix (Ref. 47, Chap. 3) of our parameters, taking mass, length, time, and current as the independent dimensions, has the form:

$$\begin{array}{c|ccccc} & t_p & \rho_0 & A & R & \mu_0 \\ \hline M & 0 & 1 & 0 & 0 & 1 \\ L & 0 & -3 & 0 & 1 & 1 \\ T & 1 & 0 & -n & 0 & -2 \\ I & 0 & 0 & 1 & 0 & -2 \end{array}$$

One can readily show that the matrix has rank 4, and thus our 5 parameters yield 5-4 = 1 dimensionless group which we write in the form

$$t_p = K \rho_0^{s_1} A^{s_2} R^{s_3} \mu_0^{s_4} \qquad \text{(B-1)}$$

and find

$$\begin{aligned} s_1 &= 1/2(n+1) \\ s_2 &= -1/(n+1) \\ s_3 &= 2/(n+1) \\ s_4 &= -1/2(n+1) \end{aligned} \qquad \text{(B-2)}$$

leading to the dependence of pinch time on the powers of the parameters, for various n, displayed in Table B-1.

Table B-1

Power-Dependence of Pinch-Time on Parameters

		Powers	
n	ρ_0	A	R
0	1/2	-1	2
1/4	2/5	-4/5	8/5
1/2	1/3	-2/3	4/3
1	1/4	-1/2	1
2	1/6	-1/3	2/3
3	1/8	-1/4	1/2
4	1/10	-1/5	2/5
10	1/22	-1/11	2/11

We thus recover the "classic" 1/4-power-dependence of pinch time on ρ_0 for the (n = 1) linearly rising current, as well as Cole's(38) 1/3-power-dependence for the $t^{\frac{1}{2}}$ current. Furthermore, we see that the n = 0 (constant current) case, which is of special interest to us, shows the most sensitive dependence of pinch time on the experimental parameters.

B.2 SIMILARITY RELATIONS OF THE SNOWPLOW EQUATION

In Chapter III, we obtained the linear pinch snowplow equation, Eq. (3-10), in the form

$$r \frac{d}{dt}\left[(r_0^2 - r^2)\frac{dr}{dt}\right] = \frac{-\mu_0 I^2}{4\pi^2 \rho_0} \tag{B-3}$$

We introduce normalizing variables and non-dimensionalize:

$$\begin{array}{lll} r = X r_0 & r_0 = & \text{initial radius} \\ t = T t_0 & t_0 = & \text{some reference time} \\ I = I_0 G(T) & I_0 = & \text{some reference current} \end{array} \tag{B-4}$$

so without loss of generality Eq. (B-3) goes over to the non-dimensional form:

$$X \frac{d}{dT}\left[(1 - X^2)\frac{dX}{dT}\right] = \frac{-\mu_0 I_0^2 t_0^2 G^2(T)}{4\pi^2 \rho_0 R_0^4} \tag{B-5}$$

Similarity relationships follow from imposing restrictions on the functional form of the driving current; as usual, the more severely the problem is restricted, the more powerful the resulting similarity relationship, as we see in the following cases:

Case I: Constant current, $I = I_0$.

Since there is no dependence of the driving current on time, G becomes unity in Eq. (B-5), whose right-hand side is thus a pure number, the magnitude of which depends on our choice of t_0. The simplest form results from setting

$$t_0 = 2\pi \rho_0^{1/2} r_0^2 / \mu_0^{1/2} I_0 \tag{B-6}$$

so that Eq. (B-5) becomes

$$X \frac{d}{dT}\left[(1-X^2)\frac{dX}{dT}\right] = -1 \tag{B-7}$$

There is thus a universal $X(T)$ similarity solutions for all constant-current cases, provided that the initial conditions also are similar. We can readily assume $X(0) = 1$, but as we show in the next section, the initial velocity must be $dX/dT|_{T=0} = -1/\sqrt{2}$. This solution is plotted in Fig. B-1. Note we have in Eq. (B-6) the same scaling law previously obtained by dimensional analysis.

Case II: Linearly rising current $I = \alpha t$.

Here $G = \frac{\alpha t_0 T}{I_0}$, in general the right-hand side of Eq. (B-5) becomes $(-CT^2)$, where C is a constant that is made unity by the choice

$$t_0 = (4\pi^2 \rho_0 r_0^4 / \mu_0 \alpha^2)^{1/4} \tag{B-8}$$

CP25 R-4121-66

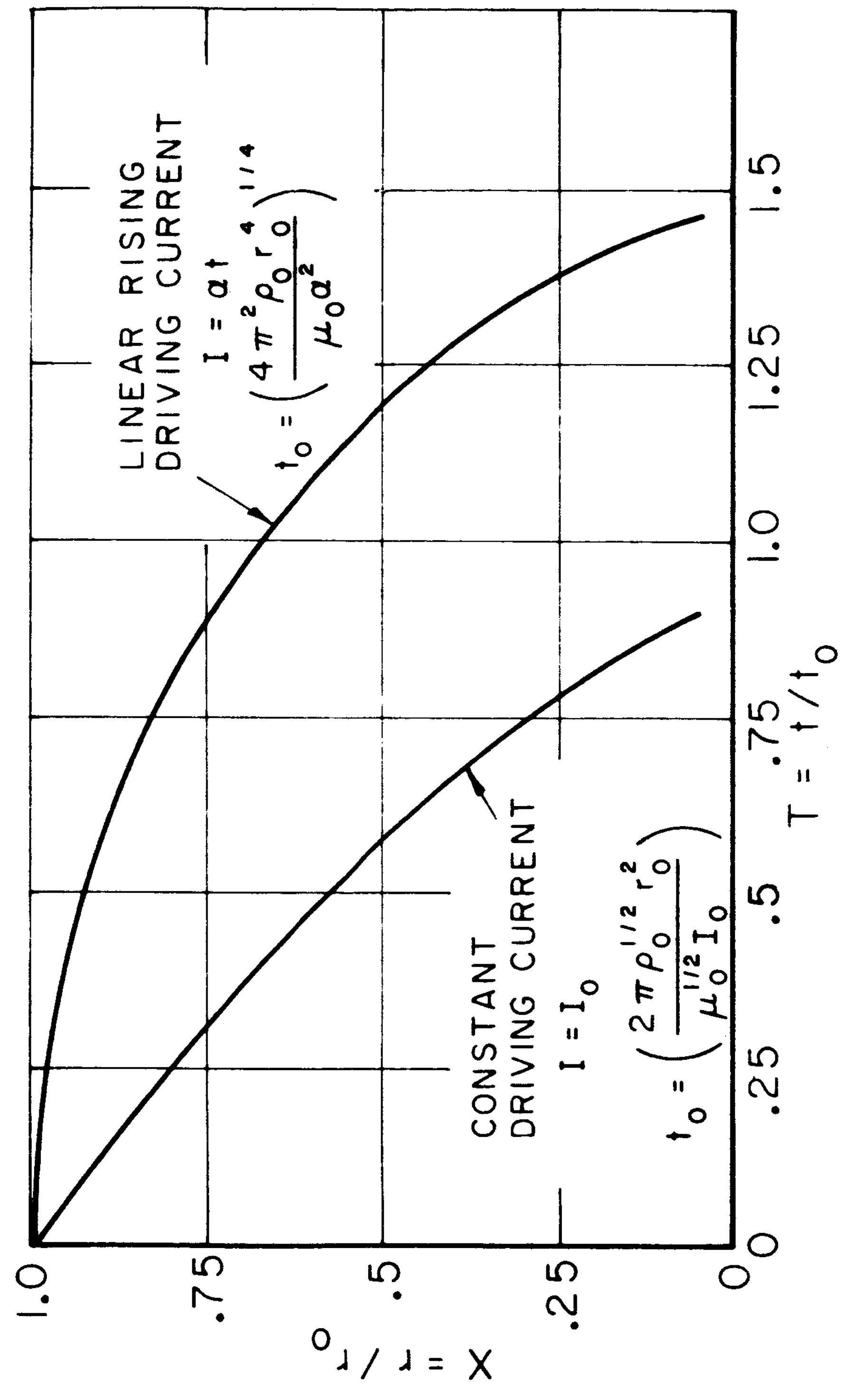

NON-DIMENSIONAL SNOWPLOW TRAJECTORIES

FIGURE B-1

leading to

$$X\frac{d}{dT}\left[(1-X^2)\frac{dX}{dT}\right] = -T^2 \tag{B-9}$$

With initial conditions $X(0)=1,\ dX/dT|_0=0$, the universal solution, $X(T)$, is also shown in Fig. B-1.

Case III: Sinusoidal current $I=I_o\sin\omega t$.

Here two parameters, I_0 and ω, are required to specify the driving current, and this less-restrictive physical situation leads to a less powerful similarity. If we set $t_0=1/\omega$, then Eq. (B-5) becomes

$$X\frac{d}{dT}\left[(1-X^2)\frac{dX}{dT}\right] = -K\sin^2 T \tag{B-10}$$

and hence all solutions in terms of the physical variables ρ_0, r_0, I_0, ω for initial conditions $X(0)=1,\ dX/dT|_0=0$ are encompassed by varying the single similarity parameter $K=(\mu_0 I_0^2/4\pi^2\rho_0 r_0^4\omega^2)$.

Case IV: Arbitrary current $I=I_0G(T)$.

We can choose t_0 in Eq. (B-5) to make the coefficient of G unity:

$$t_0=(2\pi\rho_0^{1/2}r_0^2/\mu_0^{1/2}I_0) \tag{B-11}$$

so that the snowplow equation becomes

$$X\frac{d}{dT}\left[(1-X^2)\frac{dX}{dT}\right] = -G^2(T) \tag{B-12}$$

yielding a quite restrictive similarity relationship between physical situations having driving currents of the same functional form whose time scales must vary according to Eq. (B-11).

B.3 ANALYTIC SOLUTIONS OF THE SNOWPLOW EQUATION

Certain analytic results follow from a direct attack on the equation, for special driving currents.

B.3.1 Sinusoidal Current

Curzon and Howard(49) showed the existence of a simple analytic solution to the snowplow equation for a sinusoidal driving current of a certain special frequency. Expressing this result in our formulation, we find that $X = \cos(\tau/2)$ satisfies Eq. (B-10), for $K = 3/16$. In physical variables:

$\frac{r}{r_0} = \cos\frac{\omega t}{2}$ satisfies the linear pinch snowplow equation, B-3, for the sinusoidal driving current $I = I_0 \sin \omega t$, if:

$$\omega = (4\mu_0 I_0^2/3\pi^2\rho_0 r_0^4)^{1/2} \qquad \text{(B-13)}$$

The pinch time is thus given by the condition $\frac{\omega t_p}{2} = \pi/2$, yielding

$$t_p = (3\pi^4\rho_0 r_0^4/4\mu_0 I_0^2)^{1/2} \qquad \text{(B-14)}$$

B.3.2 Constant Current

By interchanging dependent and independent variables, the constant-current Eq. (B-7) becomes:

$$X(1-X^2)\frac{d^2T}{dX^2}+2X^2\frac{dT}{dX}=\left(\frac{dT}{dX}\right)^3 \tag{B-15}$$

Equation (B-15) is first order in dT/dX. Explicitly, setting $\rho=dT/dX$ we have:

$$X(1-X^2)\frac{d\rho}{dX}+2X^2\rho=\rho^3 \tag{B-16}$$

This is Bernoulli's equation, so let $z=\rho^{-2}$:

$$\frac{dz}{dX}-\frac{4Xz}{(1-X^2)}=\frac{-2}{X(1-X^2)} \tag{B-17}$$

Thus the original second order non-linear Eq. (B-7) has been reduced to the above first order linear equation. Solving Eq. (B-17) by variation of parameters we find

$$z=(1-X^2)^{-2}\left\{-2\int_1^X\frac{1-X^2}{X}dX\quad+k\right\} \tag{B-18}$$

Recalling that $z=\rho^{-2}=\left(\frac{dT}{dX}\right)^{-2}=V^2$, one obtains

$$V^2=(1-X^2)^{-2}[X^2-1-2\ln X+k] \tag{B-19}$$

We must set $k=0$ for V to be finite at $X=1$, then $V^2(T=0)$ is given by

$$\lim_{X\to 1}V^2=1/2 \tag{B-20}$$

So the desired solution $X(T)$ for the case of constant driving current is contained implicitly in the quadrature

$$T(X) = \int_X^1 \frac{(1-s^2)\,ds}{(s^2-1-2\ln s)^{1/2}} \tag{B-21}$$

B.3.3 Zero Driving Current

For zero driving current the non-dimensionalized snowplow equation reduces to

$$\frac{d}{dT}\left[(1-X^2)\frac{dX}{dT}\right] = 0 \tag{B-22}$$

and one readily obtains the implicit solution

$$X - \frac{X^3}{3} = c_1 T + c_2 \tag{B-23}$$

The connection with physical reality is a bit tenous here, since the snowplow magnetic piston concept predicates a driving current, but we can imagine that the sheet is launched and then some time before pinch the driving current stops, while we still suppose that the swept-up mass continues as a narrow piston-like structure, giving up its momentum as it picks up additional mass; then Eq. (B-23) defines the trajectory. The constants of integration, C_1 and C_2 , are most reasonably determined by specifying end conditions in the form

$$X(T_f) = 0$$

$$\left.\frac{dX}{dT}\right|_{T_f} = -V_f \tag{B-24}$$

where the minus sign makes V_f positive for an inward-moving sheet.

With the above end-conditions, Eq. (B-23) becomes

$$X - \frac{X^3}{3} = V_f(T_f - T) \qquad \text{(B-25)}$$

so that there is a single solution-curve for X , if $[V_f(T_f-T)]$ is regarded as the independent variable.

B.3.4 Constant Velocity Solution

One can, of course, synthesize an arbitrary number of closed-form solutions by assuming a functional form for $X(T)$ and thus determining the corresponding driving current from $G(T)$ through Eqs. (B-11) and (B-12). The constant velocity solution has some special interest, since it corresponds to a dynamic efficiency of 50 percent as we showed in Chapter VI. If we set

$$\frac{dX}{dT} = -V^* \qquad \text{(B-26)}$$

then we find from Eq. (B-12) that

$$G(T) = V^*(1 - V^* T)$$

so a constant velocity is produced by a linearly falling driving current.

APPENDIX C

ELECTRODYNAMICS OF PULSED DISCHARGES

C.1 ELECTRIC FIELDS AND TERMINAL VOLTAGE

The electric field between two parallel plates (neglecting fringing) in the simple electrostatic case is given by the applied voltage divided by the plate separation. The situation inside the discharge chamber is considerably more complex, however, and the electric field may depend on the radial position. It is instructive to examine several idealized situations.

We consider the cylindrically symmetric geometry shown in Fig. C-1. A current I enters the lower electrode, flows through a thin cylindrical shell, termed the current sheet for brevity, at radius r_1, and returns to the current source via the upper electrode and the return conductor. The electrodes and the return conductors are regarded as perfect conductors. Our results will follow from the integral form of Faraday's Law of Induction:

$$\oint \bar{E}\cdot d\bar{l} = -\frac{d\phi}{dt} \qquad \text{(C-1)}$$

where the line integral of the electric field is taken around a complete closed contour, and ϕ is the total magnetic flux enclosed by this contour.

It follows immediately that if the current sheet is

AP25-RA122-66

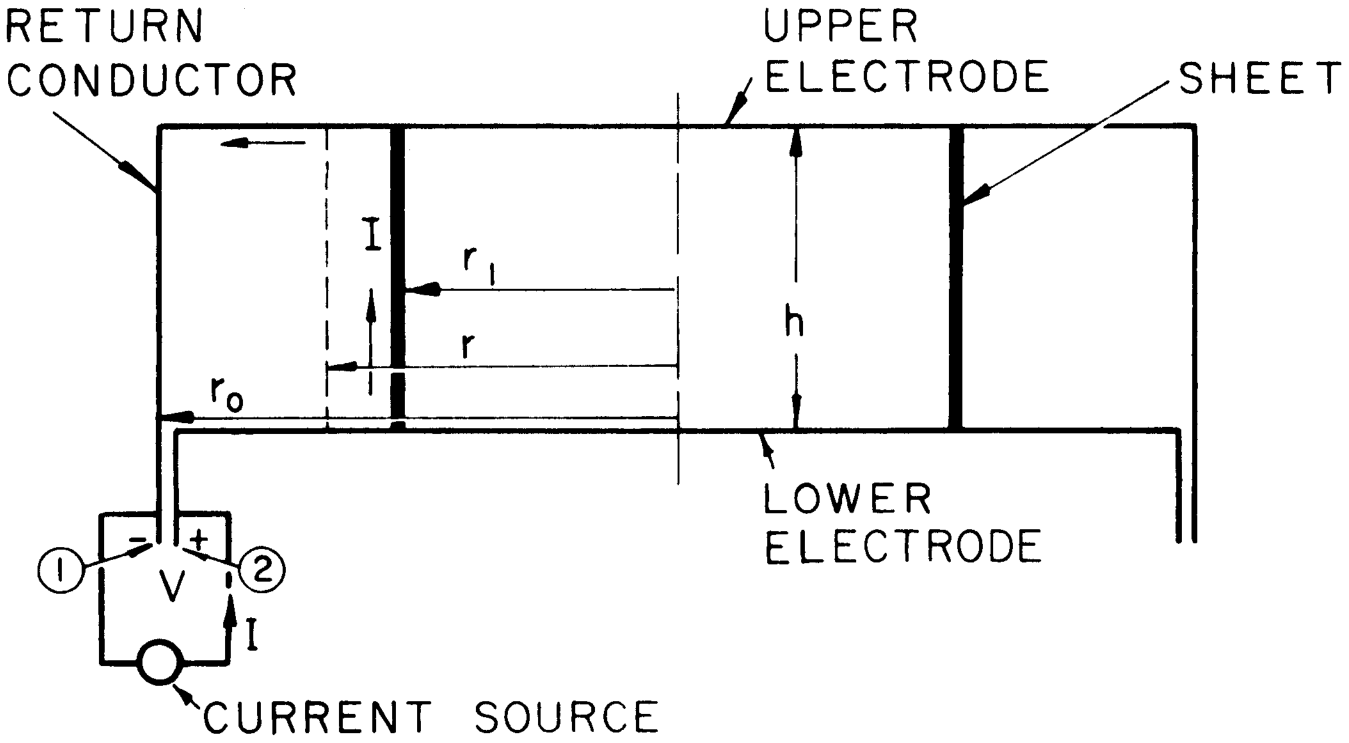

CONFIGURATION FOR DISCUSSION OF ELECTRIC FIELDS

FIGURE C-1

perfectly conducting, there is no electric field inside the sheet position: consider a contour that starts at some radius $r < r_1$ on the lower electrode, runs parallel to the axis between the two electrodes, traverses the upper electrode to the sheet, runs down the sheet, and returns to the starting point along the lower electrode. The R.H.S. of Eq. (C-1) is zero, since there is no magnetic field inside the current sheet radius, so the line integral must be zero. But the contributions along the conducting surfaces are zero as a consequence of the perfectly conducting assumption, therefore the electric field between the plates is zero; note that this result is independent of the driving current or current sheet motion.

Let us now consider the contour which goes from point ② to point ① in Fig. C-1, along the lower electrode, traverses the gap at some radius $r \geq r_1$, and returns via the upper electrode and the return conductor. The contribution to the integral across the current source terminals is just (-V), and across the inter-electrode spacing is $E(r)h$, while the rest of the contour traverses perfect conductors and hence contributes nothing to the integral. Equation (C-1) becomes

$$-V + E(r)h = \frac{-d\phi(r)}{dt} \qquad \text{(C-2)}$$

or

$$E(r) = \frac{1}{h}\left(V - \frac{d\phi(r)}{dt}\right) \qquad \text{(C-3)}$$

where $\phi(r)$ is the flux enclosed by the contour described and is given by

$$\phi(r) = \int_{r}^{r_0} \frac{\mu_0 I h}{2\pi r} dr = \frac{\mu_0 h I}{2\pi} \ln\left(r_0/r\right) \tag{C-4}$$

so

$$E(r) = V/h - \frac{\mu_0}{2\pi} \ln\left(r_0/r\right) \frac{dI}{dt} \tag{C-5}$$

Take $r = r_1$, and assume the sheet to be perfectly conducting so $E(r_1) = 0$, then

$$V = \frac{\mu_0 h}{2\pi} \ln\left(r_0/r_1\right) \frac{dI}{dt} \tag{C-6}$$

Substituting Eq. (C-6) into (C-5), we find

$$E(r) = \frac{\mu_0}{2\pi} \ln\left(r/r_1\right) \frac{dI}{dt} \tag{C-7}$$

Thus the magnitude of the electric field induced by changing current is greatest at the outside wall, which is consistent with the observation that secondary breakdown, which occurs with an oscillatory driving current, begins at the chamber wall.

In writing Eq. (C-6) we implicitly assumed that the conducting sheet was stationary; motion of the sheet introduces a new term into $d\phi/dt$ when the contour lies in the sheet, since the area of the surface bounded by the contour is changing with time, and the electric field is given by:

$$E(r) = \frac{\mu_0}{2\pi} \ln(r/r_1) \frac{dI}{dt} - \frac{\mu_0 I}{2\pi r_1} \frac{dr_1}{dt} \tag{C-8}$$

So that there is a contribution to the field, proportional to the current and the sheet velocity, and uniform in the region between the sheet and return conductor.

We now note that the inductance of the configuration is given by

$$L = \frac{\mu_0 h}{2\pi} \ln(r_0/r_1) \tag{C-9}$$

and the terminal voltage expression becomes

$$V = L\frac{dI}{dt} + I\frac{dL}{dt} = \frac{d}{dt}(LI) \tag{C-10}$$

One can readily show that if the sheet has total resistance R , there is a contribution to the electric field, $E_R = IR/h$, which is uniform throughout, both inside and outside the sheet radius. In this case we have the complete terminal voltage equation:

$$V = L\frac{dI}{dt} + \left(R + \frac{dL}{dt}\right)I \tag{C-11}$$

C.2 DAMPING BY TIME-VARYING INDUCTANCE

Consider the RLC series circuit:

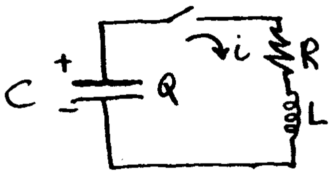

We know that if $R=0$, the current is sinusoidal, for small R the current is a damped sinusoid, but for $R^2>4L/C$, the current does not oscillate and the circuit is said to be overdamped. It is evident from Eq. (C-11) that if the inductance is time-varying, its time-derivative, $\dot{L}$, appears as a resistance. It has been suggested that current reversal in a (usually underdamped) capacitor-bank driven discharge could be avoided if $\dot{L}$ were sufficiently large. In this section we develop a <u>necessary</u> criterion for circuit damping, without a complete knowledge of L as a function of time.

With a time-varying inductance, the current equation for the series RLC circuit becomes

$$\frac{d^2 i}{dt^2}+\left(\frac{R}{L}+\frac{2}{L}\frac{dL}{dt}\right)\frac{di}{dt}+\left(\frac{1}{LC}+\frac{1}{L}\frac{d^2L}{dt^2}\right)i = 0 \qquad \text{(C-12)}$$

We can eliminate the first derivative term in Eq. (C-12) by setting $i=pv$, (50) where

$$p = \mathrm{EXP}\left[-1/2\int f(t)\,dt\right] \qquad \text{(C-13)}$$

$$f = \left(\frac{R+2\dot{L}}{L}\right)$$

so that Eq. (C-12) is transformed to

$$v'' = \left(\frac{R^2+2R\dot{L}}{4L^2} - \frac{1}{LC}\right) v \qquad \text{(C-14)}$$

Now Υ is a positive quantity so that the sign of $\dot{L}$ is the same as v. A <u>necessary</u>, but not sufficient, condition that the current be non-oscillatory is that the right hand side coefficient in Eq. (C-14) be positive, i.e. our criterion is:

$$R(R+2\dot{L}) > 4L/C \qquad \text{(C-15)}$$

Note that this reduces to the usual damping criterion for constant inductance.

The above criterion was applicable to the current equation, we can also write the circuit equation in terms of the charge on the capacitor Q:

$$\frac{d^2Q}{dt^2} + \left(\frac{R+\dot{L}}{L}\right)\frac{dQ}{dt} + \frac{Q}{LC} = 0 \qquad \text{(C-16)}$$

A parallel analysis then yields a <u>necessary</u> criterion that the capacitor charge, and hence the voltage, be non-oscillatory:

$$\frac{1}{4}\left(\frac{R+\dot{L}}{L}\right)^2 + \frac{1}{2}\left(\frac{L\ddot{L}-(R+\dot{L})\dot{L}}{L^2}\right) > 1/LC \qquad \text{(C-17)}$$

Again, we recover the usual damping criterion if L is constant; but in this case we can also set $R=0$ and obtain

$$(2L\ddot{L} - L^2) > 4L/C \qquad \text{(C-18)}$$

So we see a non-oscillatory voltage can be occasioned, in the absence of resistance, by a sufficiently large value of d^2L/dt^2 .

C.3 VALIDITY OF THE INDUCTANCE CONCEPT

While we have made free use of the concept of inductance in the above two sections, it should not be blindly applied to the general time and space varying distributed current density that may occur in a discharge. In particular, a consistent definition must relate circuit current I , magnetic field energy W_M , and inductance L through the relations

$$W_M = \int \frac{B^2}{2\mu_0}\,dV = \tfrac{1}{2} L I^2$$

where the volume integral is to be taken over all space. But we have seen in Section (5-2), for an oscillating driving current, that when the circuit current I is zero, inside the pinch chamber, there may well be a circulating current, and hence magnetic field and non-zero magnetic field energy.

ACKNOWLEDGEMENTS

To Professor Robert G. Jahn, for his guidance, insight, and sustaining interest, I am deeply indebted.

Mr. J. D. Tregurtha assisted greatly, both in the assembly of the apparatus and the conduct of the experiments.

Valuable help was provided by the staff of the Guggenheim Laboratories for the Aerospace Propulsion Sciences, particularly by Mr. Tony Poli and Mrs. Kathryn Walter of the Design Group, and Mr. Lanny Hoffman of the Computing Group.

Financial support for portions of the work was provided by the Ford Foundation, the National Science Foundation, and the National Aeronautics and Space Administration under grant NsG-306-63. Use was made of computer facilities supported in part by National Science Foundation Grant NSF-GP579.

This work is dedicated to my parents, in small token for their constant support and many sacrifices.

REFERENCES

1. W. R. Corliss, "Propulsion Systems for Space Flight," McGraw-Hill, New York, 1960.

2. R. W. Spence and Franklin P. Durham, "The Los Alamos Nuclear-Rocket Program," Astronautics and Aeronautics, 3-6, 42 (June 1965).

3. R. G. Jahn, "The Physics of Electric Propulsion," (to be published) McGraw-Hill, New York, 1966.

4. B. Pinkel, W. H. Krase, A. Leonard, D. L. Trapp, Z. A. Typaldos and R. B. Wilson, "Electrical Propulsion in Space: Mission Comparisons, Development Cost, Reliability, and Their Implications for Planning," Rand Corporation Memorandum RM-4056-NASA, (1964).

5. E. Stuhlinger, "Ion Propulsion for Space Flight," Chapter 5, McGraw-Hill, New York, 1964.

6. D. B. Miller, "Acceleration of Plasmas by Inductively Generated Electromagnetic Fields," Univ. of Michigan, Dept. of Electrical Engineering, Plasma Engineering Laboratory, Report No. 02836-10-F, (1961).

7. R. H. Lovberg, "Nonsteady M.H.D. Accelerators," in Plasma Technology: Aerospace Applications, J. Grey, ed., Prentice Hall, to be published.

8. A. C. Ducati, G. M. Giannini, E. Muehlberger, AIAA Journal, 2-8, (Aug. 1964), p. 1452.

9. D. E. T. F. Ashby, T. J. Gooding, A. V. Larson, "Quasi-Steady-State Pulsed Plasma Thrustors," AIAA Paper No. 65-338, (July 1965).

10. G. W. Sutton and A. Sherman, "Engineering Magnetohydrodynamics," McGraw-Hill, New York, 1965.

11. A. S. Bishop, "Project Sherwood - The U.S. Program in Controlled Fusion," Anchor Books, Garden City, 1960.

12. S. Glasstone and R. H. Lovberg, "Controlled Thermonuclear Reactions," D. Van Nostrand Co., Princeton, 1960.

13. D. J. Rose and M. Clark, Jr., "Plasmas and Controlled Fusion," M.I.T. Press, John Wiley and Sons, 1961.

14. L. Spitzer, Jr., "Physics of Fully Ionized Gases," Interscience, New York, 1956.

15. Rosenbluth, M., "Infinite Conductivity Theory of the Pinch," Los Alamos Scientific Laboratory Report LA-1850, 1954.

16. L. A. Artsimovitch, "Controlled Thermonuclear Reactions," p. 127, Gordon and Breach, New York, 1964.

17. J. Marshall, "Performance of Hydromagnetic Plasma Gun," Phys. Fluids 3-1, p. 134 (Jan. 1960).

18. A. E. Kunen and W. McIlroy, "The Electromagnetic Pinch Effect for Space Propulsion," in Dynamics of Conducting Gases, A. B. Cambel and J. B. Fenn, eds., Northwestern University Press, Evanston, 1960.

19. L. Aronowitz and P. Mostov, "A DC Glow Model of the Formation of the Magnetic Piston," Republic Aviation Corp. Plasma Propulsion Laboratory Report PPL-TR-60-21(241), Dec. 1960.

20. R. G. Jahn, W. von Jaskowsky, and R. L. Burton, "Ejection of a Pinched Plasma from an Axial Orifice," AIAA J. 3-10, (Oct. 1965).

21. R. G. Jahn and W. von Jaskowsky, "Structure of a Large-Radius Pinch Discharge," AIAA J. 1-8, p. 1809-1814 (Aug. 1963).

22. R. G. Jahn and W. von Jaskowsky, "The Plasma Pinch as a Gas Accelerator," AIAA Paper No. 63-013, March 1963.

23. R. G. Jahn and W. von Jaskowsky, "Current Distributions in Large-Radius Pinch Discharges," AIAA J. 2-10, p. 1749-1753, (Oct. 1964).

24. I. A. D. Lewis and F. H. Wells, "Millimicrosecond Pulse Techniques," Pergamon Press, 2nd ed. 1959.

25. K. A. Saunders and R. L. Sewell, "Command Resonance Charging System for the Astron Accelerator," University of California Lawrence Radiation Laboratory Report UCRL-7363, May 1963.

26. H. J. White, P. R. Gillette and J. V. Lebacqz, "The Pulse-Forming Network," Chapter 6 of "Pulse Generators," G. N. Glasoe and J. V. Lebacqz, eds., M.I.T. Radiation Laboratory Series Vol. 5, McGraw-Hill, New York, 1948.

27. D. Rigney, L. Kraus, and H. Malamud, "Synthesis of Current Waveforms by Type C Networks," Republic Aviation Corp. Plasma Propulsion Laboratory Report PPL-TR-61-4(258), Jan. 1961.

REFERENCES-contd.

28. M. H. Dazey, V. Josephson, and R. F. Wuerker, "The Use of Low-Impedance Transmission Lines in Plasma Heating and Confinement Studies," Space Technology Laboratories Physical Research Laboratory Report STL/TR-60-0000-09255, Aug. 1960.

29. B. R. Hayworth, "Energy Storage Capacitors: An Experimental and Theoretical Investigation of their Properties," San Diego State College M.S. Thesis, June 1964.

30. R. G. Jahn, W. von Jaskowsky, and A. L. Casini, "Gas-Triggered Pinch Discharge Switch," Rev. Sci. Instr. 36-1, 101-102, Jan. 1965.

31. R. G. Jahn, W. von Jaskowsky, and A. L. Casini, "Gas-Triggered Inverse Pinch Switch," Rev. Sci. Instr. 34-12, 1439-1440, Dec. 1963.

32. E. P. Butt and A. B. Gillespie, "The Measurement of Voltage, Current and Magnetic Field in Pulsed Toroidal Gas Discharge Apparatus at Harwell," in "Instruments and Measurements," H. V. Koch and G. Ljungberg, eds., Vol. 2, 938-973, Academic Press, New York, 1961.

33. R. H. Lovberg, "The Use of Magnetic Probes in Plasma Diagnostics," Annals of Physics 8, 311-324 (1959).

34. G. A. Rowell, "Cylindrical Shock Model of the Plasma Pinch," Princeton University M.S. Thesis, 1966.

35. A. Cole and O. Laporte, "A Study of Cylindrical Shock Waves in a Sector Shock Tube," Univ. of Michigan Dept. of Physics Report 02539-26-T, July 1961.

36. B. T. Chu, "An Analytical Approach to the Problem of Pinch Dynamics," Republic Aviation Corp. Plasma Propulsion Laboratory Report PPL-TR-60-9(185).

37. J. D. Jackson, "Classical Electrodynamics," Wiley, New York, 1962, p. 325.

38. G. H. A. Cole, "The Pinch Effect," Science Progress (London) 47-187, 437-458, July 1959.

39. T. Goto, M. Sato, and T. V. Chida, "On the Mechanism of the Pinch Effect," Il Nuovo Cimento, 14-5, 1065-1075, Dec. 1959.

REFERENCES-contd.

40. R. G. Jahn and W. von Jaskowsky, "Exhaust of a Pulsed Plasma from an Axial Orifice," AIAA Paper No. 65-92, 1965.

41. W. J. Guman, "Partition of Energy in a Pulsed Plasma Accelerator," *Phys. Fluids 3*, p. 483, 1960.

42. A. H. Shapiro, "The Dynamics and Thermodynamics of Compressible Fluid Flow," Vol. 1, Ronald Press, New York, 1953, p. 118.

43. J. A. Stratton, "Electromagnetic Theory," McGraw-Hill Book Co., New York, 1941, p. 550.

44. M. Abromovitz and I. A. Stegun (eds.), "Handbook of Mathematical Functions," National Bureau of Standards, Washington, D. C., 1964, p. 1024.

45. P. W. Schmidt, "Tables of $\int_0^x J_0(t)\,dt$ for Large x ," *J. Math. and Phys. 34*, 169-172, (1955).

46. P. W. Bridgman, "Dimensional Analysis," Yale University Press, New Haven, 1963.

47. H. L. Langhaar, "Dimensional Analysis and Theory of Models," Wiley, New York, 1951.

48. S. Pai, "Magnetogasdynamics and Plasma Dynamics," Springer-Verlag, Vienna, 1962, p. 42-44.

49. F. L. Curzon and R. Howard, "Z-Pinch Dynamics for Sinusoidally Time-Dependent Discharge Currents," *Nuc. Fusion 3*, 293, 1963.

50. J. Mathews and R. L. Walker, "Mathematical Methods of Physics," W. A. Benjamin, New York, 1964, p. 12.